The Design, Implementation and Performance of the PHENIX Time-of-Flight West Detector

by

Brian Love

Thesis

Submitted to the Faculty of the

Graduate School of Vanderbilt University

in partial fulfillment of the requirements

for the degree of

MASTER OF SCIENCE

in

Physics

May, 2009

Nashville, Tennessee

APPROVED

Julia Velkovska (thesis adviser)

Charles Maguire

TABLE OF CONTENTS

LIST OF TABLES

LIST OF FIGURES

CHAPTER 1

Introduction

The PHENIX experiment, in order to probe nuclear matter under the extreme conditions of high temperature and high energy density, has been designed to observe, measure, and reconstruct relativistic heavy-ion collisions. PHENIX operates at the Relativistic Heavy Ion-Collider (RHIC), at Brookhaven National Lab. Additional experiments at RHIC are STAR, PHOBOS and BRAHMS, see Fig. 1. The RHIC collider-accelerator facility consists of two independent storage rings that collide both like and unlike particle species, providing the opportunity to study both symmetric and asymmetric systems, such as in Gold-Gold (Au-Au) and Deuteron-Gold (d-Au) collisions, respectively. The beams in the RHIC storage rings can be tuned in energy, and experimental evidence from both medium and high energy collisions has been collected. See Table (1.1) for information detailing the particle species, energy levels, and data-set size of experimental evidence collected at RHIC, years 2000-2008. Baseline measurements for the study of densely packed high-temperature partonic (or nuclear) matter are obtained from Proton-Proton (p-p) collisions. The heaviest nuclear species that the RHIC beams collide is gold (Au). Additionally, the RHIC facility collides polarized protons in order to study experimentally the spin-structure of the nucleon.

The RHIC facility became operational in the year 2000, and since that time, the RHIC experiments have experimentally verified the existence of the theoretically predicted Quark Gluon Plasma (QGP). The QGP is an extreme state of matter where the constituent particles of protons and neutrons–quarks and gluons–move in a state deconfined from the strong nuclear force. Experimental evidence from RHIC (years 2000 to 2005), which established the existence and verified the thermal properties of the QGP, is presented in a series of seminal white papers published by each of the four RHIC experiments [**1, 2, 3, 4**].

The topic of this thesis is the design, implementation and performance of the PHENIX Time-of-Flight West detector subsystem (TOFW). After a two year design and construction phase (year 2004 to 2006), and as part of a collaborative high transverse momentum (p_t) upgrade initiative for PHENIX that included the design and implementation of an Aerogel Cherenkov detector (ACC), as

well in cooperation with a similarly motivated upgrade project for STAR [**5**], the PHENIX TOFW detector was installed in June of 2006. By the time-of-flight method alone, the TOFW performs pion-kaon separation up to 3 GeV/c and proton identification up to 5 GeV/c. For increased high-p_t functionality, momentum and mass dependent signals originating from induced Cherenkov radiation in the ACC and Ring Imaging Cherenkov detector (RICH) are used. Pion signals can be extracted from the ACC between 1 GeV/c and 4 GeV/c, and in the RICH from 4 GeV/c to at least 10 GeV/c, or beyond, where identification is limited by low statistics. Proton identification can be extracted from ACC signals between 6 GeV/c and 9 GeV/c. The RICH has been operational in PHENIX since its beginning in year 2000. The ACC was installed in the summer of 2004. Together, the TOFW, ACC, and RICH provide pion, kaon and proton particle identification (PID) functionality for PHENIX up to 9 GeV/c. The PHENIX TOFW detector utilizes Multi-Gap Resistive Plate technology (MRPC). The STAR TOF upgrade uses similar MRPC detectors (with no Aerogel) [**6, 7, 8, 9**]. The ALICE experiment at the LHC uses a MRPC based TOF detector system in conjunction with a Cherenkov radiation detector [**10**].

Using the PHENIX TOF-West detector for intermediate and high-P_t PID, one's understanding of heavy-ion collision is deepened providing further insight into the varying and underlying particle production mechanisms, such as in the soft physics of the QGP medium and the hard-scattering physics of jet production.

(A) Aeriel View of Brookhaven National Lab

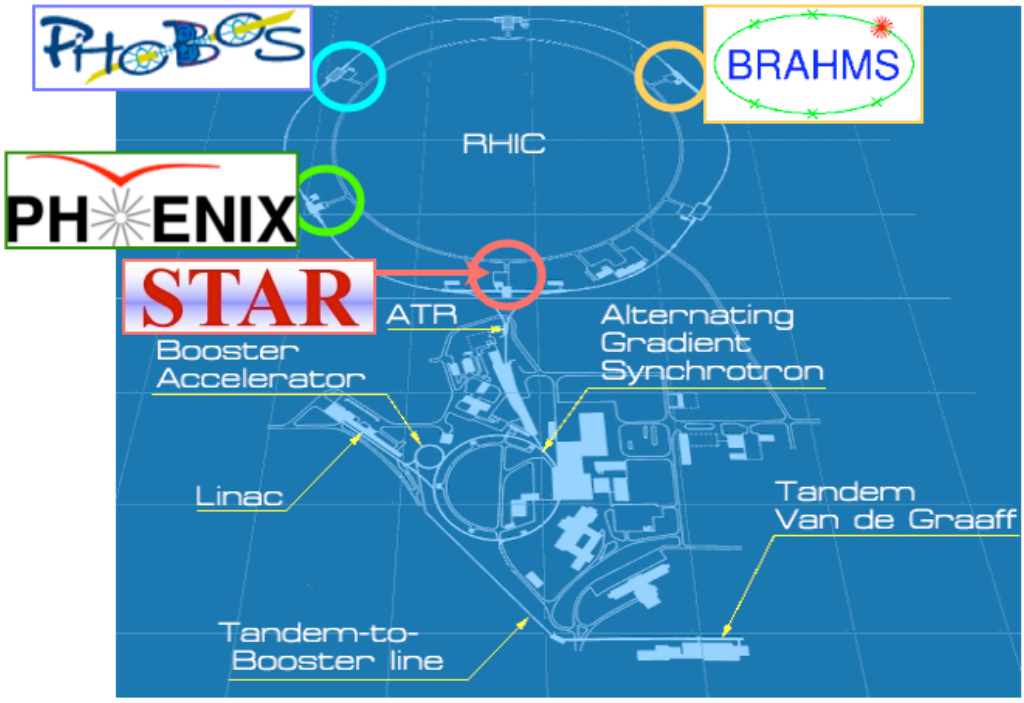

(B) The RHIC Collider-Accelerator Complex

FIGURE 1.1. Experimental Relativistic Heavy-Ion Physics at Brookhaven National Lab (Long Island, NY, USA)

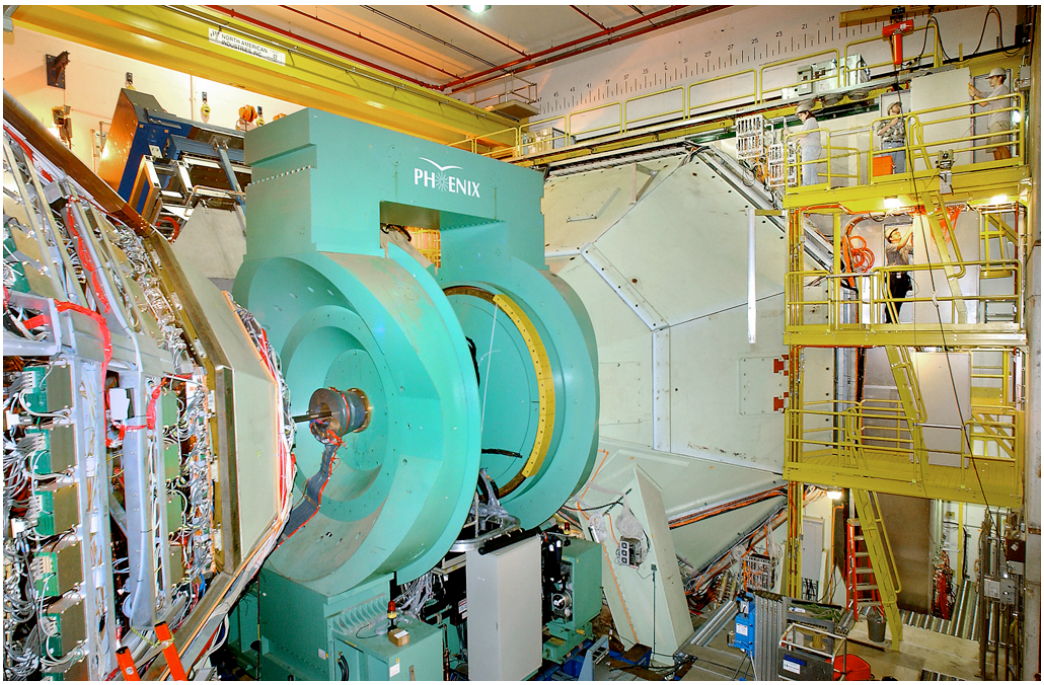

(A)

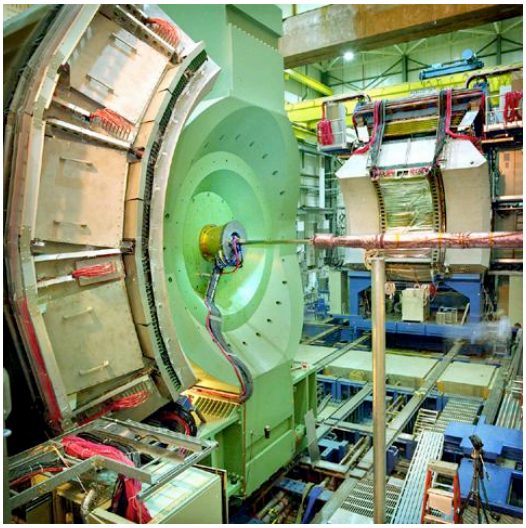

(B)

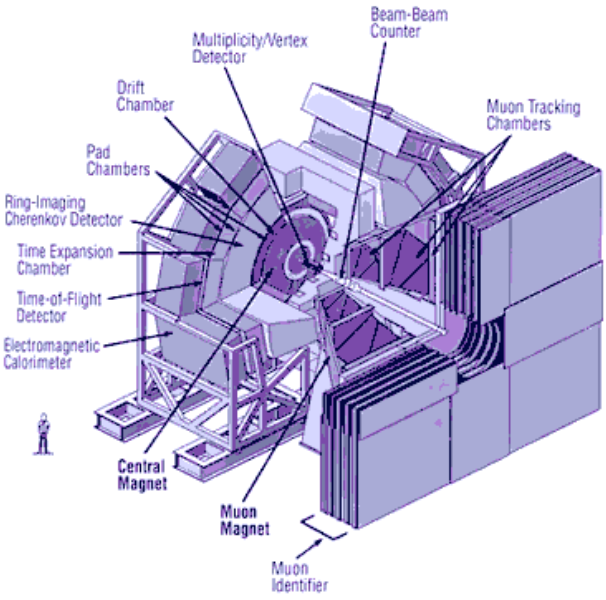

(C)

FIGURE 1.2. The PHENIX Detector

TABLE 1.1. Summary of RHIC Luminosity 2001-2008

Run	Year	Species	$\sqrt{s_{NN}}$ (GeV)	Integrated Luminosity	N_{events}	Size *of* Data Set
01	2000	Au-Au	130	$1b^{-1}$	10M	3TB
02	2001/02	Au-Au	200	$24b^{-1}$	10M	10 TB
		Au-Au	19		<M	
		p-p	200	$0.15pb^{-1}$	3.7B	20TB
03	2002/03	d-Au	200	$2.74nb^{-1}$	5.5B	46 TB
		p-p	200	$0.35pb^{-1}$	6.6B	35 TB
04	2003/04	Au-Au	200	$241\mu b^{-1}$	1.5B	270 TB
		Au-Au	62.4	$9\mu b^{-1}$	58M	10 TB
05	2005	Cu-Cu	200	$3nb^{-1}$	8.6 B	173 TB
		Cu-Cu	62.4	$0.19nb^{-1}$	0.5 B	48 TB
		Cu-Cu	22.4	$2.7\mu b^{-1}$	3.7B	20TB
		p-p	200	$3.8pb^{-1}$	85 B	262TB
06	2006	p-p	200	$10.7pb^{-1}$	233B	310 TB
		p-p	62.4	$0.1pb^{-1}$	28B	25 TB
07	2007	Au-Au	200	$813\mu b^{-1}$	5.1B	650 TB
08	2007/08	d-Au	200	$80nb^{-1}$	160 B	437 TB
		p-p	200	$5.2pb^{-1}$	115 B	118 TB
		Au-Au	9.2		< 5k	

CHAPTER 2

The PHENIX Experiment

When two heavy-ions collide at relativistic energies, numerous particles are produced in the aftermath, and the PHENIX experiment is comprised of numerous detector subsystems that measure the trajectory and energy of these particles. Additional detector subsystems near the vertex provide global event characterization. The PHENIX spectrometer (the collective operation of all detector subsystems) is supported by an extensive online computing infrastructure, that includes a high-throughput and high-speed data acquisition system (DAQ), real-time monitoring of detector performance, and near-real time limited analysis of raw data. Outside of the online operational environment, full production of raw data and subsequent physics analysis is supported by a comprehensive offline computing system. The offline computing environment includes complete implementation of individual detector response software, the framework for event by event reconstruction, and the implementation of static and dynamic calibration parameters.

The PHENIX detector subsystems can be classified by their location with respect to the vertex (the point of collision). See Fig. 1.2c and Fig. 2.1 for the configuration of detector subsystems. The PHENIX spectrometer includes two central arms positioned at mid-rapidity ($| \eta | < 0.35$, $\eta-$pseudorapidity), two muon arms positioned at forward rapidities ($1.2 < | \eta | < 2.4$), and a collection of inner detectors positioned along the beam line. The beam line in PHENIX runs north-south. The four large spectrometer arms are often referred to by their cardinal directions: central arm west, central arm east, muon arm north, and muon arm south.

The inner detectors of PHENIX provide global event classification, such as vertexing, centrality, and reaction plane measurements. The Beam-Beam Counters (BBC), positioned along the beam line and near the center of the detector, measure the ionizing radiation from incident charged particles at far-forward rapidities. Further down stream of the vertex, the zero degree calorimeters (ZDC) measure the incidence of spectator neutrons from a collision event. Because the central detectors provide event classification, they play an integral part of the PHENIX online trigger system **[11]**.

When a particle traverses the fiducial volume of the PHENIX detector, the numerous detector

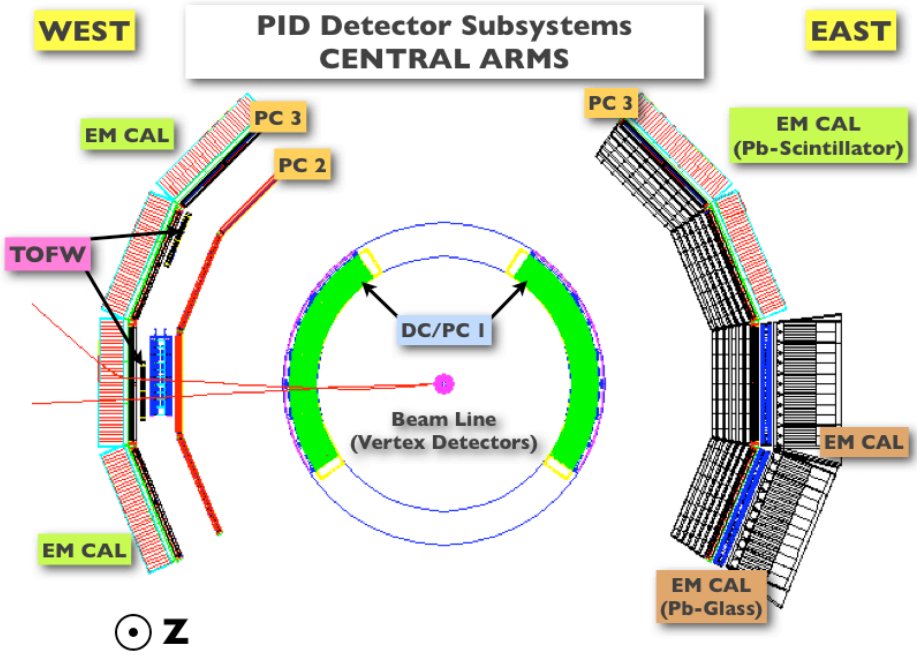

FIGURE 2.1. PID Detector Subsystems
Single-particle simulation of a 4 GeV/c Lambda decaying into a proton and pion ($\Lambda(1115) \rightarrow p + \pi^-$).

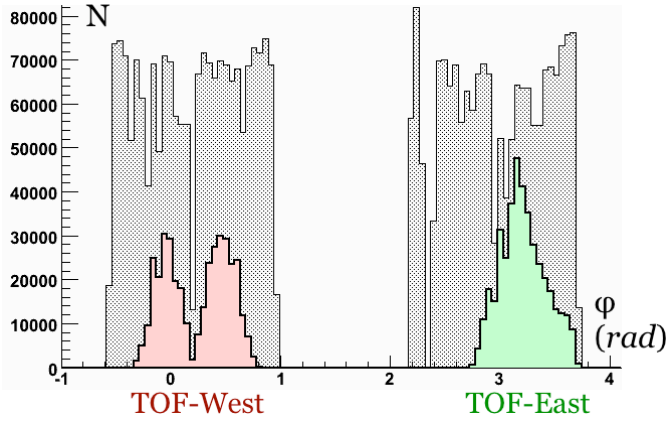

FIGURE 2.2. Azimuthal TOF Acceptance of the PHENIX Central Arms
Track selection includes drift chamber quality, PC3 track matching, and vertex positioning of $\pm 30cm$.

subsystems provide the ability to simultaneously measure several different physical observables of a particle. A particle with a clean trajectory through the central arm spectrometer (east or west) will be tracked by the pad chamber detectors; its momentum will be measured by the bend angle of the particle's path through the drift chamber; the velocity and time-of-flight will be measured by a time-of-flight detector; and, a mass and energy dependent signal will be measured in the electromagnetic calorimeter.

The central arm detectors used for PID are detailed in Fig. 2.1. Here a single particle simulation of a 4 GeV/c Λ particle is shown. The Lambda decays into a proton and negative pion. Fig. 5.1 (in Chapter 5) provides a close up schematic of the combined Aerogel (ACC) and TOFW PID system. The concomitant measurement of the time-of-flight and momentum of a particle provides the ability to experimentally derive a particle's mass, which uniquely identifies a particle (the time-of-flight PID procedure is described in Chapter 3, and the experimental results are shown in Chapter 4 of this thesis).

The EMCAL measures the energy of electrons and photons, as well as partial hadronic showers from charged hadrons [**12**]. For hadrons the EMCAL is not deep enough to contain the full hadronic showers and extract a complete hadron energy-loss signal. The RICH is not drawn in Fig. 2.1, but is located between the DC and PC2. The RICH can be used to tag pions above 4 GeV/c, in addition to identifying electrons [**13**]. The EMCAL for energy measurement and the RICH for electron-ID provides effective electron-photon (γ) differentiation, the ability to measure the electron and photon spectrum, and the ability to reconstructed through their di-photon decay products $\pi^0(135) \rightarrow \gamma\gamma$ and $\eta^0(549) \rightarrow \gamma\gamma$. Additionally, with the ability to identify and eliminate photon background contamination from π^0 and η^0 production, PHENIX is well positioned to study direct photons originating from the QGP medium, which provide a probe of the gluon density [**14**][**15**].

The functionality for measuring an incident particle's time of flight has been incorporated into the central arm spectrometers, where hadron identification is most valuable. Since its inception, PHENIX has operated a plastic scintillator based TOF detector in the east arm (sectors 0 and 1), with timing resolution $\sigma = 96\,ps$ [**16**]. The new MRPC based TOF (the topic of this thesis) was installed in the west arm (sectors 1 and 2) and operates with timing resolution $\sigma = 70ps$. With the installation of the new TOFW, the overall area of acceptance for TOF measurements has increased and the timing resolution capability improved. The azimuthal acceptance of both TOFE and TOFW is shown in Fig. 2.2. The azimuthal distribution of track-trajectories is shown. The

ϕ angle is determined at the exit point of the particle's track from the DC. Those tracks passing through each central arm, which are defined as high-quality DC tracks and with a track origin matching the collision vertex, are shaded in grey. The subset of those tracks also incident on either TOF detector are colored as indicated.

The position of the TOFW detector was chosen to optimize track by track analysis with the ACC and TOFE detectors. The TOFW detector was constructed in two large subsections. One subsection was installed in line behind the Aerogel detector, in the west arm sector 1, for the purpose of coordinated PID functionality, where tracks will pass through both detectors. A second subsection of the TOFW was installed in the west arm sector 2, and will be used to improve upon jet correlation studies.

Jet correlation studies involve the simultaneous measurement of particle distributions at varying azimuthal angles with respect to the jet axis. Fig. 2.3 shows a characteristic azimuthal distribution of particles produced from high-energy jet fragmentation. Jets are produced at 180° angles. Furthermore, when produced in a heavy-ion collision, sometimes the partonic scattering will occur on the edge of the medium, such that one side of the jet propagates through the dense medium (the QGP), resulting in medium induced deformation of particle distributions. Sometimes referred to as away-side jets, these can be considered high-energy probes of the primordial QGP medium.

Jet production is ideally studied using a pair of co-linear high-resolution TOF detectors (such as the TOFW and TOFE) for the identification of high-p_t trigger particles, demarcating the jet axis. The relative configuration of TOFW detectors is shown schematically in Fig. 2.1, as well as in the central arm azimuthal acceptance shown in Fig. 2.2. Particle production falling outside the high-p_t acceptance (the grey region of Fig. 2.2) can be studied collectively, as unidentified charged hadrons. In jet studies a normalization of the particle distribution orthogonal to the jet axis is needed. Because of the limited geometrical acceptance of the PHENIX central arms in azimuth, the west arm of sector 2 is the only position for the TOFW detector that provides the opportunity to measure both the back to back high-p_t jet trigger particles and the 90°-normalization levels. For the TOFW detector in west sector 1, jet axis normalization measurements fall outside the azimuthal acceptance of the PHENIX central arms.

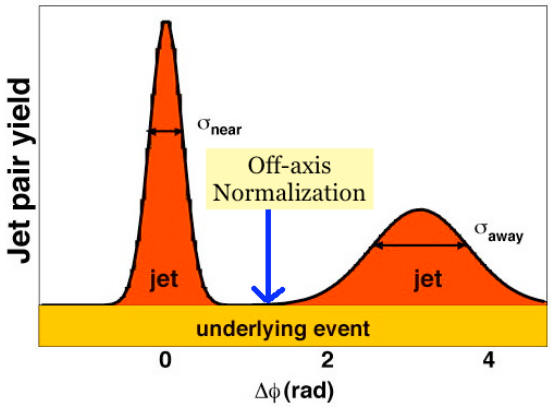

FIGURE 2.3. Azimuthal Distribution of Jet Production

CHAPTER 3

Particle Identification by Time of Flight

3.1. Particle Production

In a heavy ion collision at RHIC, particles are produced at relativistic energies, with momentum energies at a level of significant proportion to the particle's mass, or greater. Most particles are produced in the low momentum region ($P_t < 1$ GeV$/c$). To note, full efficiency of the PHENIX central arms begins at $P_t = 200$ MeV$/c$. Pions $(\pi, 140)$ are the most abundant, being produced "copiously." In practice, when observing unidentified particles at low momentum, one often assumes the particle is a pion. Additionally, in decreasing order of yield, Kaons $(K, 493)$, Protons $(p, 938)$, and Deuterons $(d, 1875)$ are produced. See Table 4.1 for exact PDG values. These fundamental hadrons are stable enough to be detected successfully. Other hadrons, such as the Lambda (Λ), Phi (ϕ), and J/Psi (J/ψ) are produced, but are detected indirectly through their decay remnants, such as $\phi(1019) \rightarrow K^+K^-$, $\Lambda(1115) \rightarrow P\pi^-$, and $K^0_S(498) \rightarrow \pi^+\pi^-$. Leptons, the electron (e) and muon (μ), are produced and are detected as well. Electrons are identified by the RICH. Muons are identified by the muon arms, positioned behind the steel of the central magnets and at far-forward rapidities. Some leptons originate directly from the primordial Quark Gluon Plasma (so called, direct, prompt, or "thermalized" leptons) and others from the leptonic decay of heavy hadrons, such as $J/\psi(3097) \rightarrow e^+e^-$ and $J/\psi(3097) \rightarrow \mu^+\mu^-$. The production and energy of photons (γ) can be measured, using the Electromagnetic Calorimeter (EM Cal) to measure energy and the RICH to tag and exclude electrons from the photon signal. Both "thermalized" photons, originating from the QGP, and those from hadronic decays, such as $\pi_0(135) \rightarrow \gamma\gamma$, are studied.

Particle production can be broken into three distinct momentum (P_t) ranges that generally correspond to different production mechanisms, see Table 3.1 and Table 3.3. Low-P_t particles originate from "soft" processes. High-P_t particles are produced through "hard" scattering processes, which contribute, for example, to jet production. With respect to momentum, at RHIC energy levels, particle production is low-momentum dominated. In the low-P_t domain PID can be preformed by the Electromagnetic Calorimeter (EMCAL) or the (scintillator based) TOF-East detector. For

TABLE 3.1. Customary Momentum Range *for* Particle Production

Low	$P_t < 1$ GeV/c
Intermediate	1 GeV/c $< P_t <$ 5 GeV/c
High	$P_t > 5$ GeV/c

TABLE 3.2. PID-Fiducial Volume By Detector

Detector	Technology	
	P_t Range	
	$Pion - Kaon$	$Kaon - Proton$
TOF West $\sigma = 79$ *ps* (*w/ Aerogel* and Ring Imaging Cherenkov detectors)	Multi-Gap Resistive Plate Chamber (MRPC)	
	< 9 GeV/c	< 9 GeV/c
TOF East $\sigma = 96$ *ps*	Plastic Scintillator	
	< 2 GeV/c	<4 GeV/c
EM Cal $\sigma = 450$ *ns*	Lead Scintillator	
	< 1 GeV/c	< 2 GeV/c

TABLE 3.3. Particle Production Mechanisms

Hard Processes	Parton-Parton scattering resulting in Jet Production. High-p_t hadrons.
Soft Processes	QGP Medium Effects–the time-evolution of a thermalized medium, including pressure gradients resulting from system size anisotropy and the cooling of energy-dense partonic matter. Low and Intermediate-p_t *Pions, Kaons, Protons.*
	Coalescence–the association of two neighboring hadrons into a bound state. Occurs post hadronization and prior to kinetic freeze out. *Deuterons*
	Decay Remnants–from strong and weak decaying hadrons
Other	Background–from incident particles interacting with detector materials. *Electron, Positron contamination*

intermediate and high-P_t PID a high resolution timing detector, such as the MRPC based TOFW, is used. For the PID operational range of different detector technologies, see Table 3.2.

When experimentally measuring both momentum and time-of-flight, the resolution width increases with momentum, and subsequently limits one's ability to precisely reconstruct a particle's mass, as can be seen by the parametrization of the mass-squared bands in Fig. 3.2. Particle differentiation becomes indeterminate when the mass-squared bands merge. Improved timing resolution can compensate for worsening momentum resolution. Ultimately, however, PID by time-of-flight is timing resolution dependent. Hadrons whose species is indeterminate are referred to as unidentified hadrons, or unidentified particles.

3.2. Particle Identification By Time-of-Flight

Charged particle identification (PID) in PHENIX is achieved using the time-of-flight method. In this method, from each particle's track-trajectory the time-of-flight, T_{tof}, path length, L, and momentum, P, are measured. From these three measured quantities, one derives an experimental measurement of the particle's rest mass. Listed here are some useful quantities:

TABLE 3.4. Unit Conventions

Quantity		Units	Experimental Observable
Time of Flight	T_{tof}	ns	measured
Path Length	L	cm	measured
Momentum	P	GeV/c	measured
Mass	m	GeV/c^2	derived
Energy	E	GeV	derived
Velocity	β	$1/c$	derived

As formalized in special relativity, the energy-momentum state of particles in the relativistic regime is described by the energy-mass equation [1][**17**]:

$$E^2 - (pc)^2 = (mc^2)^2 = mass \tag{3.1}$$

Eq. (3.1) can be expressed in the functional form, $m(E,p) = constant$.

In a more rigorous derivation from first principles of the energy-mass relation, one can consider a four-dimensional phase space comprised of time, and the three vector quantities, x, y, and z. We consider $\vec{p} = f(E(t), x, y, z)$. The energy-mass (Eq. 3.1) is obtained from a dot product of the 4-momentum vector.

$$m^2 = p_\mu p^\mu \tag{3.2}$$

[1]As first postulated by Albert Einstein, presented in the 3rd *Annus Mirabilis* paper, "On the Electrodynamics of Moving Bodies" or "Zur Elektrodynamik bewegter Körper", Annalen der Physik. 17:891-921. (June 30, 1905)

Rising from the formalism of special relativity, γ and β are the relativistic (velocity dependent) quantities that relate the rest frame of a particle in motion with the laboratory frame [2].

$$\gamma = \frac{1}{\sqrt{1-\beta^2}} \, and \;\; \beta = \frac{v}{c} \tag{3.3}$$

For a given mass of particle, β andγ are functions of the total energy.

$$\beta(E) = \sqrt{1 - \frac{mc^2}{E}} \tag{3.4}$$

$$\gamma(E) = \frac{E}{mc^2} \tag{3.5}$$

Energy can be defined as a function of a particle's momentum,

$$E = \frac{pc}{\beta} \tag{3.6}$$

With (3.6), Eq. (3.1) can be transformed into,

$$(mc^2)^2 = (\frac{pc}{\beta})^2 - (pc)^2 \tag{3.7}$$

$$(mc^2)^2 = (\frac{1}{\beta^2} - 1)(pc)^2 \tag{3.8}$$

When using the unit conventions outlined in table 3.4, eq (3.8) becomes,

[2]To briefly review, the relativistic equations reduce to the classical regime for $v << c$, where $\beta \approx 0$ and $\gamma \approx 1$. γ is often referred to as the Lorentz Factor (for historical reasons). γ derives purely from geometric considerations of four-dimensional vector fields. The theory of special relativity postulates that all observers (in an inertial frame of reference) will measure identically the speed of light (in a vacuum) regardless of their relative motions. The invariance of the speed of light is formalized in the construction of the four-vector space known as space-time, or Minkowski space, which is comprised of the three vector-degrees of freedom (x,y,z) and time (t). In the simple application of measure theory to this four-dimensional vector field, γ obtains as the measure that relates time to space. $\frac{1}{\gamma} = d\tau/dt$, where τ can be conceived of as the "proper" time, or more applicably, $d\tau/dt = \tau_A - \tau_B$, where τ_A and τ_B are the time states of the two reference frames.

$$m^2 = (\frac{1}{\beta^2} - 1)p^2 \tag{3.9}$$

and in final form, when considering $\beta = \frac{v}{c}$ and $v = L/T_{tof}$,

$$m^2 = ((\frac{cT_{tof}}{L})^2 - 1)p^2 \tag{3.10}$$

Eq. 3.10 is the most useful functional form, clearly relating the three measured quantities (T_{tof},L, and p) with the derived quantity m. This equation was derived in consideration of the constant relation between the quantities of energy and momentum, as expressed in relativistic form in Eq. 3.1.

3.3. Timing Resolution

The mass-squared observable (Eq. 3.10) represents a derived quantity by which particle identification (PID) is obtained. What follows is a brief discussion of the experimental methods by which the three input parameters T_{tof}, L, and P, are obtained in PHENIX, as well the resolution (or statistical variation) associated with each of these measurements. The momentum dependencies of both the timing and momentum resolution will demonstrate the high-momentum limitation of PID.

3.3.1. Momentum σ_α. In PHENIX, the momentum of a particle is determined by mapping the curvature of its trajectory as it passes through a region of known magnetic field strength (Fig. 3.1). The size of the bend angle, α, and the error in its measurement, σ_α, are momentum dependent. The highest momentum particles pass through the magnetic field with very little modification to their trajectories, almost straight. Lower momentum particles curve substantially.

To note, the particle trajectories of pions with momentum below 100 MeV/c are modified so severely, they curve sharply and may fall outside the geometric acceptance of the PHENIX detector. 100 MeV pions can be tracked, but with limited efficiency. Over 90% efficiency is achieved for pions with $p_t > 200$ MeV/c.

For completeness, the fundamental relation between the strength of the magnetic field, B, and the force imparted to a particle of charge q is presented:

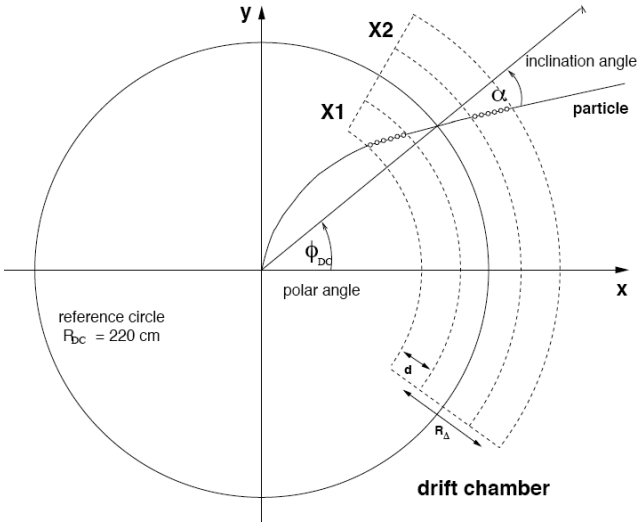

FIGURE 3.1. Drift Chamber

$$\vec{F} = q \mid \vec{v} \times \mathbf{B} \mid \tag{3.11}$$

From Newton's Second Law, the fundamental method for obtaining the momentum of a moving body from the force acted upon it is:

$$F = \frac{d\vec{P}}{dt}$$

$$P = \int F dt$$

The Drift Chamber (DC) is used to determine the bend angle, α, as shown in Fig. 3.1. The Drift Chamber is positioned immediately outside the region of magnetic field, and provides high resolution tracking. To note, tracking of particle trajectories beyond the DC is provided by a three-tiered Pad Chamber system.

The angles measured by the drift chamber are ϕ_{DC} and α. The reference radius, R_{DC}, of the Drift Chamber is 220cm and is recorded in Table 3.6 along with other PHENIX central arm detectors.

To first order, the momentum (in GeV/c) is measured by the angle α according to:

TABLE 3.5. Field Integral K (mRad/GeV)

Run 1	++	84
Run4	++	104
Run7	-+	74

$$P = \frac{K}{\alpha} \tag{3.12}$$

where K is a field integral of the magnetic field strength $K = \int B \cdot dl$. K is a constant, and is determined by the magnetic field orientation. K values for different magnetic field orientations are given in Table 3.5.

From Eq. 3.12, we immediately obtain a relation between the uncertainty σ_p and σ_α:

$$\frac{\sigma_p}{p} = \frac{\sigma_\alpha}{\alpha} = p\frac{\sigma_\alpha}{K}$$

For low-P_t particles, there is a large dynamic range of response. At high-P_t however, changes in transverse momentum will produce very little change in α, where all trajectories are relatively straight ($\alpha \approx 0$). For high-p_t particles, σ_α and the subsequently derived quantity σ_p increase. The drift chamber momentum resolution is finite and high-P_t limited, and contributes to the high-p_t limitations of high-p_t PID.

To note, for systematic studies of the PHENIX acceptance, and thereby the experiment's sensitivity to accurately extract various physics signals from a relativistic heavy-ion collision, the field orientation of the PHENIX central magnets, consisting of a north and south yoke, can be reversed in polarity. Additionally, for extracting certain calibration parameters, such as beam position offsets, the magnet is turned off. The field configurations are often referred to as plus-plus, minus-minus, and zero-field runs. With the introduction of the Hadron Blind Detector (HBD) in 2007, the PHENIX central magnet, in reference to the north and south yoke, operated in plus-minus and minus-plus configurations. The HBD is a near vertex detector, and was installed between the vertex and the DC. These hybrid-polarities optimize HBD performance by providing a near-zero field in the HBD region.

3.3.2. Path Length σ_L. The path length, L, of a particle's trajectory is determined from the track reconstruction. The uncertainty in the path length, σ_L, can be obtained from the uncertainty

TABLE 3.6. PHENIX Detector Subsystems: Distance from the Vertex

PHENIX Detector Subsystems: Distance From the Vertex		
Detector		Distance (cm)
West	East	
Hadron Blind Detector (HBD)		5-66
Drift Chamber		220
Pad Chamber 1		250
Ring Imaging Cherenkov (RHIC)		330
Pad Chamber 2		410
Aerogel		430
Time-of-Flight West		480
Pad Chamber 3		500
	Time-of-Flight East	510
EM Cal (Pb-Scintillator)		610
	EM Cal (Pb-Glass)	630

in the bend angle, σ_α. However, σ_L is only significant for low momentum particles, ($P_t < 200GeV$). For particles detectable within the fiducial volume of PHENIX ($P_t > 200GeV$), contribution from σ_L to the variance of T_{tof} and m^2 can be neglected.

For reference, the distance from the vertex to the Time-of-Flight West (TOFW) is given in Table 3.6. For high momentum particles, with relatively straight trajectories, the distances in Table 3.6 can be considered rough estimates of the path length, L. More precise path length measurements for individual particles are determined at the data production level, during the comprehensive event reconstruction process.

To note, precise path length measurements require precise determination of the vertex position. Through the life of a RHIC beam store, slight drifts in the beam position occur (in the X, Y plane), requiring corrections known as beam position offsets. These corrections are calculated post-production and are implemented at the data-analysis level.

3.3.3. Time of Flight σ_{tof}. The time-of-flight, T_{tof}, is obtained from direct measurement of the start time and stop time. The start time is the collision time of a collision event, which is obtained from the Beam-Beam Counters (BBC). The stop time is obtained by the Time-of-Flight (TOF) detector.

The timing resolution of the time-of-flight (TOF) detector is obtained from the difference of measured and expected time, assuming the mass of a particle to be a pion:

$$\Delta T = T_{tof} - T_{expected,\pi} \tag{3.13}$$

where,

$$\Delta T = T_{tof} - \frac{L}{\beta c} \tag{3.14}$$

The derived quantity, $1/\beta$, can be expressed in terms of the observables, m and p,

$$\frac{1}{\beta} = \sqrt{\frac{m^2}{p^2} + 1} \tag{3.15}$$

Thus,

$$T_{exp} = \frac{L}{c}\sqrt{\frac{m^2}{p^2} + 1} \tag{3.16}$$

And,

$$\Delta T = T_{tof} - \frac{L}{c}\sqrt{\frac{m^2}{p^2} + 1} \tag{3.17}$$

This definition for T_{exp} (Eq. 3.16) is used when experimentally extracting $T_{tof} - T_{exp}$, where p and L are experimentally obtained observables and m (set to the pion mass) is inputted *a priori* for T_{exp}.

The measured distribution of ΔT can be used to extract the experimental timing resolution, σ_{tof}, under the following conditions: $m = m_\pi$ and 1 GeV/c $< p_t <$2 GeV/c. For this momentum range, for the pion, $\frac{m}{p} \ll 1$, and Eq. (3.17) reduces to,

$$\Delta T = T_{tof} - \frac{L}{c} \tag{3.18}$$

Above 2 GeV/c, contamination from kaons begins to broaden the pion mass $T - T_{exp}$ distribution, at which point $\sigma_{\Delta T}$ no longer represents the timing resolution of the detector, see Fig. (4.2) in section

4.1. The error associated with Eq. (3.18) is,

$$\sigma^2_{\Delta T} = \sigma^2_{tof} + \sigma^2_L \tag{3.19}$$

As discussed previously, the uncertainty in the path length, L, is negligible, and Eq. (3.19) reduces to,

$$\sigma_{\Delta T} = \sigma_{tof} \tag{3.20}$$

Within this limited momentum range, and when considering $T_{exp,\pi}$, $\sigma_{\Delta T}$ is a direct measure of the detector's timing resolution, σ_{tof}.

Additionally, for lower momentum particles, the timing resolution can be understood by the relation:

$$\sigma^2_{\Delta T} = \sigma^2_t + (\frac{L^2}{\gamma^2 c})\frac{\sigma^2_p}{p^2} + \frac{1}{\beta c}^2 \sigma^2_L \tag{3.21}$$

In Eq. (3.21), again, the σ_L term can be neglected. The σ_p/p term can be derived from the measured σ_α of the drift chamber (DC) and the appropriate K value of the magnetic field configuration (discussed above). For a given momentum bin width of known PID (i.e. mass), γ can be calculated directly. L is obtained from the known radial position of the TOFW detector, or, more specifically, from a track-by-track projection, obtained at the data production level from the event reconstruction algorithms.

The timing resolution derived here is the measured, or effective, timing resolution of the TOFW detector, which incorporates the start-time resolution of the BBC ($\sigma_{BBC,START} \cong 40\ ps$).

$$\sigma_{TOF,INTRINSIC} = \sqrt{\sigma^2_{TOF,MEASURED} - \sigma^2_{BBC,START}} \tag{3.22}$$

$$\sigma_{TTOF,INTRINSIC} = \sqrt{(0.079)^2 - (0.040)^2} = 0.0693ns \tag{3.23}$$

$\sigma_{tof} = 79\ ps$ is determined from the $T - T_{exp,\pi}$ distribution for 1 GeV/c $< p_t <$1.2 GeV/c

and stripID = 220. The distribution of $T - T_{exp,\pi}$ by momentum bin are shown in Fig. 4.2. As calculated in Eq. (3.23), the intrinsic timing resolution of the TOFW is 69 *ps.* This measurement was extracted using calibrated TOFW data, detailed in section 9.2 when discussing the detector calibrations with respect to time-of-flight timing measurements.

3.4. Particle Identification Bands

The resolution of the derived m^2 distribution from Eq. (3.10) can be parametrized as a function of three experimentally derived constants–σ_α, σ_{ms}, and σ_{ttof}–and the experimentally measured variables, mass, m, and momentum, p:

$$\sigma^2_{m^2} = f(m, p; \sigma_\alpha, \sigma_{ms}, \sigma_t) \tag{3.24}$$

From the appropriate propagation of errors in Eq. (3.10), a parametrization that can be compared to experimental results is:

$$\sigma^2_{m^2} = \frac{\sigma^2_\alpha}{K^2}(4m^4p^2) + \frac{\sigma^2_{ms}}{K^2}(4m^4(1 + \frac{m^2}{p^2})) + \frac{\sigma^2_t c^2}{L^2}(4p^2(m^2 + p^2)) \tag{3.25}$$

This equation, Eq. (3.25), represents a parametrization of the experimentally observed uncertainty in the derived measurement of a particle's mass by the method of time-of-flight. In this model, the three resolution constants (σ_α, σ_{ms}, and σ_{ttof}) are assumed to be constant in momentum and mass. These resolutions arise from the following experimental measurements: First, σ_α corresponds to momentum resolution, where α is the measured angle of inclination of a particle's track as it exits the drift chamber (see Fig. 3.1). Second, σ_{ms} refers to contributions from multiple scattering effects, such as when a particle's track is deflected (and energy lost) as a result of interacting with non-active materials, such as the mylar window of the drift chamber, the electronics boards of PC1, the steel yokes of the central magnets, etc. Considering the location and composition of materials in and around the drift chamber and PC1, estimations place σ_{ms} at 0.6 ± 0.1 (PHENIX Analysis Note 37). Third, and lastly, σ_t (or σ_{ttof}) corresponds to the measured, or effective, resolution the time-of-flight (nominally $\sigma_{tof-west} = 79\,ps$, $\sigma_{tof-east} \cong 96\,ps$, or $\sigma_{emcal} \cong 450\,ns$). Calculated from

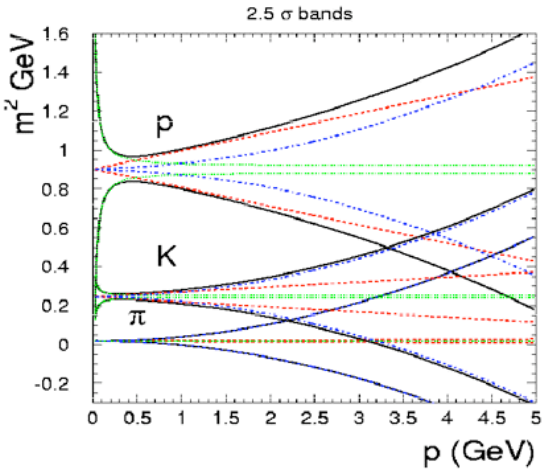

FIGURE 3.2. Parametrization of Particle Identification Bands ($\sigma_{TOF} = 120\ ps$) Bands correspond to 1-σ width of the m^2distribution. Contributions from different components are delineated in color: σ_{ms}(green) multiple scattering contribution, σ_{α}(red) momentum resolution, σ_{ttof}(blue) timing resolution

this parametrization and assuming 120 ps timing resolution, a derivation of the 1-σ mass-squared bands, along with contributions from each component, is shown in Fig. 3.2.

The m^2 bands are defined in terms of the width of each particle's m^2 distribution, derived experimentally and divided by momentum bins. The multiple scattering contribution, σ_{ms}, dominates in the low momentum ($P_t < 0.5\,GeV/c$). The momentum resolution, σ_{α}, is linear with P_t and shows increasing mass dependence. The timing resolution, σ_{ttof}, dominates at high-P_t, where, because of the shorter flight time of higher velocity particles, σ_{ttof}/t becomes significantly large.

CHAPTER 4

In-Situ Detector Performance: Measured and Derived Quantities

The performance plots shown here demonstrate the timing resolution and particle identification capabilities of the PHENIX TOFW detector. Measured results of the detector timing resolution from the method outlined in Section 3.3 are presented (Section 4.1). The measured mass-squared distributions separated by P_t bin (Fig. 4.5) demonstrate the high-p_t limits of TOF-PID functionality (Section 4.2). Performance PID plots are presented (section 4.3). Additional distributions of relevant experimental observables, path length (L) and the drift chamber bend angle (α) are presented (Section 4.4).

These plots were created using data from year 2007, Au-Au at $\sqrt{s_{NN}} = 200$ GeV. 15 million events were analyzed, which represents only a small fraction of the 5.1 billion events collected in year 2007, and 6.6 billion total events with this energy and species since the beginning of RHIC operations. 15 million events provides enough statistics to demonstrate detector performance in the low to intermediate p_t region, as well as the methods and implementation of detector calibrations, as described in Chapter 9 of this thesis. More exact measurements of the mass-squared distribution above 3.5 GeV/c require a high-statistics data analysis.

The data used here is fully calibrated. The analysis shown here was conducted using post-production, or reconstructed data, as well as the PHENIX master recalibrator with full implementation of the TOFW calibration parameters. The complete calibration of the TOFW detector is detailed in this thesis: the integrated implementation of calibration with data production and data analysis is detailed in the schema evolution tables of Chapter 8, and the calibration methods are described in Chapter 9.

4.1. Timing Resolution

The extraction of the TOFW effective timing resolution, as described in section 3.3, is shown in Fig. 4.2, where the distributions of $T - T_{exp,\pi}$ are shown by momentum bin. The equating of

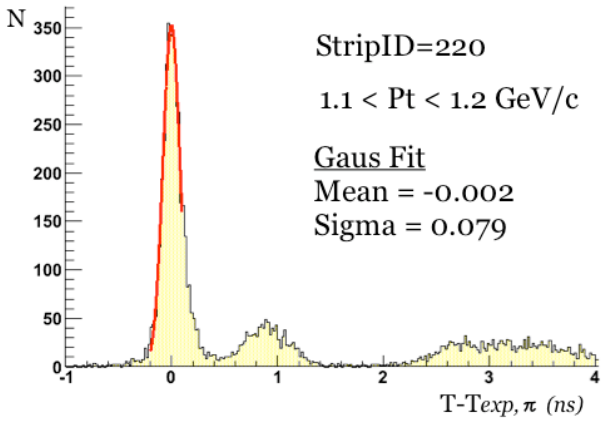

FIGURE 4.1. Timing Resolution

$\sigma_{\Delta T} = \sigma_{TOF}$ is only valid for pions in the momentum range, 1 GeV/c $< p_t <$2 GeV/c. The high momentum limitation of this approximation can be seen as the kaon peak begins to merge with the pion peak around 2.5 GeV/c. The valid momentum range is shown in detail in Fig. 4.1. A gaussian is fit to the pion distribution, where $\sigma_{tof} = 79$ *ps*. This is the measured or effective timing resolution, and does not include subtraction of the BBC start time resolution (see Section 3.3).

The TOFW detector is comprised of 512 strips. The measured timing resolution of each strip is shown in Fig. 4.3. For reference a line is drawn at 70 *ps*. To note, timing calibration parameters are derived strip-by-strip (Chapter 9). The data points at zero correspond to strips that have been removed from operation (see Table 5.2). The data points between 0 and 64 correspond to a dead high-voltage bus. The other strips have been removed from the fiducial volume as result of abnormally low efficiencies.

4.2. Mass Squared

Mass is the defining characteristic of a particle. The mass of different particle species and, for convenience, their mass-squared values are listed in Table 4.1.

The mass squared bands, m^2 *vs* p_t, demonstrate the time-of-flight PID method, and are shown in Fig. 4.4. The mass-squared quantity is derived experimentally from the measured flight time, T_{tof}, path length, L, and momentum, p, and this fundamental relation, $m = f(T_{tof}, L, p)$, is given in Eq. (3.10). When the data is Fig. 4.4 is examined in discrete momentum bins, shown in Fig. 4.5, distinctive particle bands rise above the background continuum. Particles with an experimentally derived mass within a certain width of the known particle mass are considered to be identified as

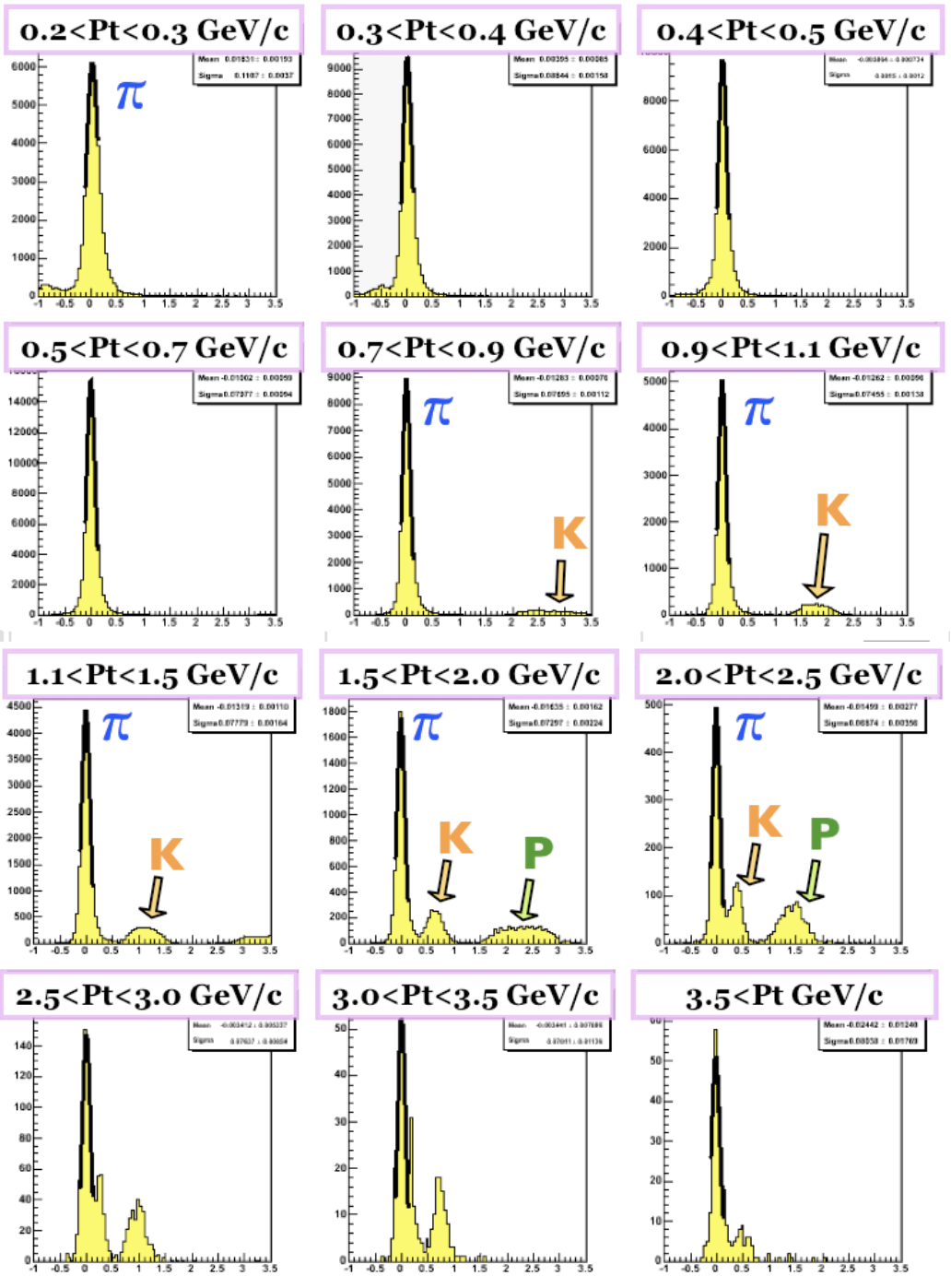

FIGURE 4.2. Timing Resolution ($T - T_{exp}$) by Momentum (x-axis in ns)

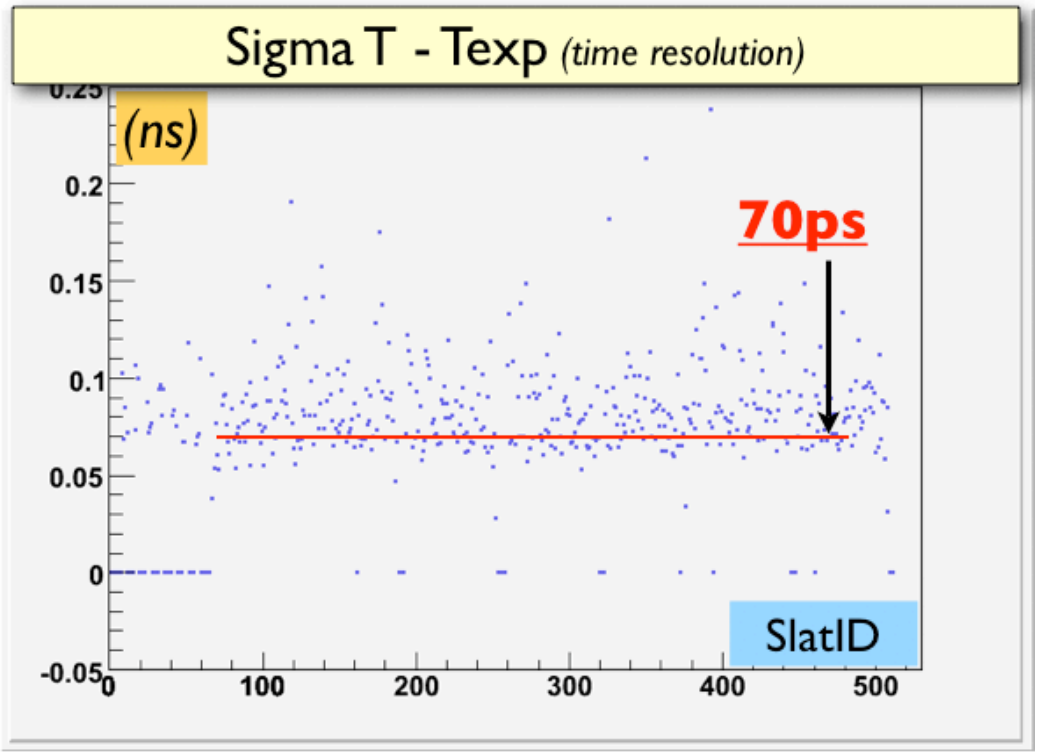

FIGURE 4.3. Strip by Strip Timing Resolution of the TOFW (Sigma of $T - T_{exp}$)

that particle species. Where the mass-squared curves begin to merge, PID becomes indeterminate. Under these circumstances, particles are referred to as unidentified.

Deuteron identification is high-p_t limited. Unlike pions, kaons, and protons, however, the deuteron mass-squared bands are not contaminated from the high-p_t induced diffusion of neighboring particle bands, see Fig 4.6. High-p_t deuteron identification, due to their low yield, is limited by low signal to background.

In the mass-squared distribution, background contribution can be the result of spuriously reconstructed tracks, for example from particles produced as the result of particle interaction with inactive detector material, such as the beam pipe, central magnets and electronics boards. Also, multiple scattering effects can contribute at low-p_t.

The time-of-flight PID bands are derived by fitting to gaussians these mass-squared distributions, Fig. 4.5, and obtaining their momentum-dependent widths. As expected, these widths increase with momentum. This is expressed in the parametrized mass-squared resolution equation, Eq. (3.25). The momentum dependence of the mass-squared widths is shown in Fig 4.7. Both the one-sigma and two-sigma bands are shown for reference.

TABLE 4.1. PDG* Mass Values

Particle Species	$mass\ (GeV/c^2)$	$mass^2\ (GeV^2/c^4)$
Pion (π)	0.13957018	0.0195
Kaon	0.493667±0.000013	0.2437
Proton	0.938272013	0.8804
Deuteron	1.8756	3.5179
Electron	0.000511	$2.6112e^{-7}$
Muon (μ)	0.105658	0.01116

**Particle Data Group*

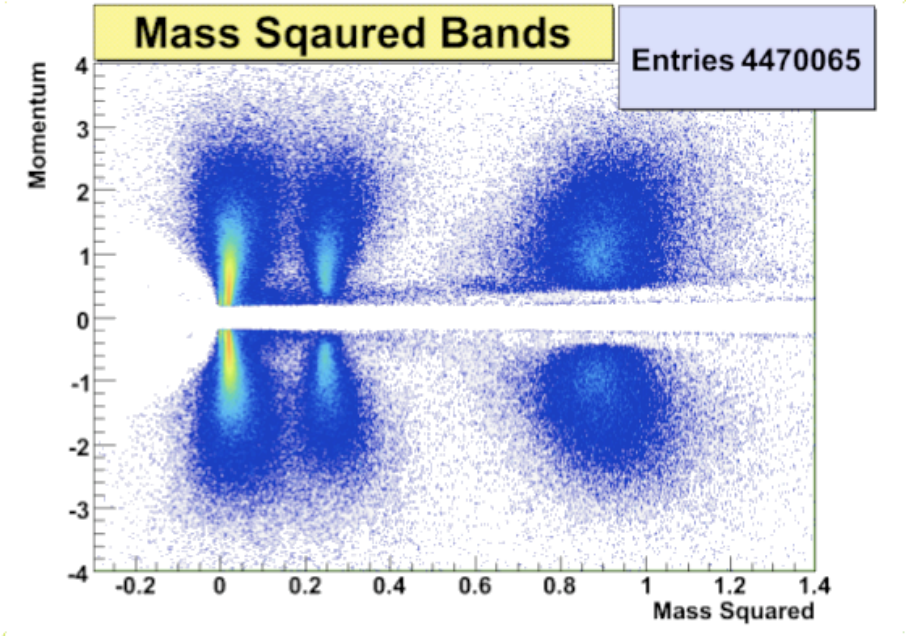

FIGURE 4.4. Mass Squared vs P_t (PID Bands)

The mean of the mass-squared bands, as a function of momentum, as extracted from the gaussian fits, is shown in Fig. 4.8. A reference line is drawn at the reference mass-squared values. As can be seen, there is good agreement with the extracted mean values and the known reference values. Around 3 GeV/c the pion and kaon bands begin to merge, and this effect can be seen in Fig. 4.8 where the mean-mass values begin to fall away from the reference line.

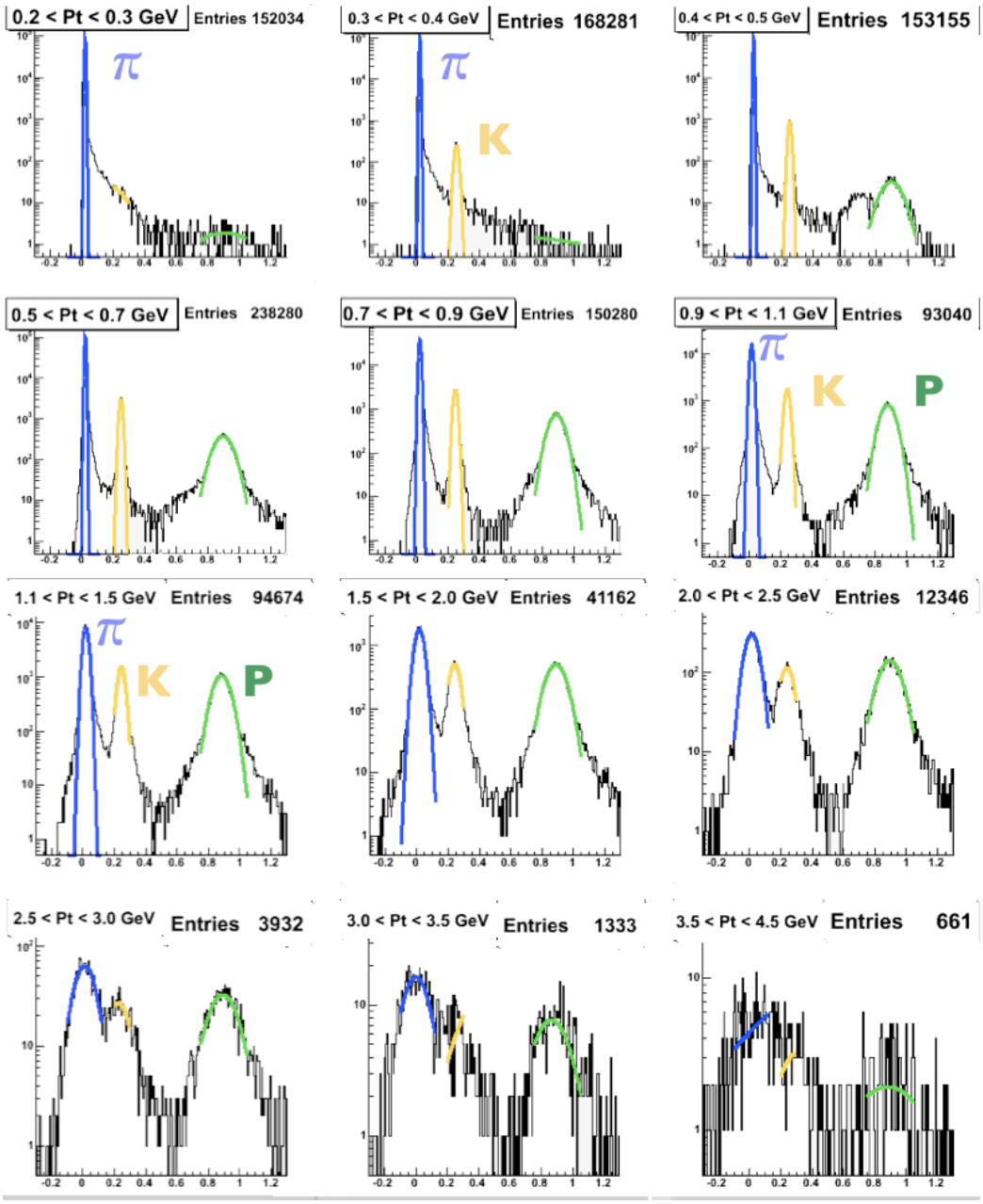

FIGURE 4.5. Mass Squared Distribution By Momentum

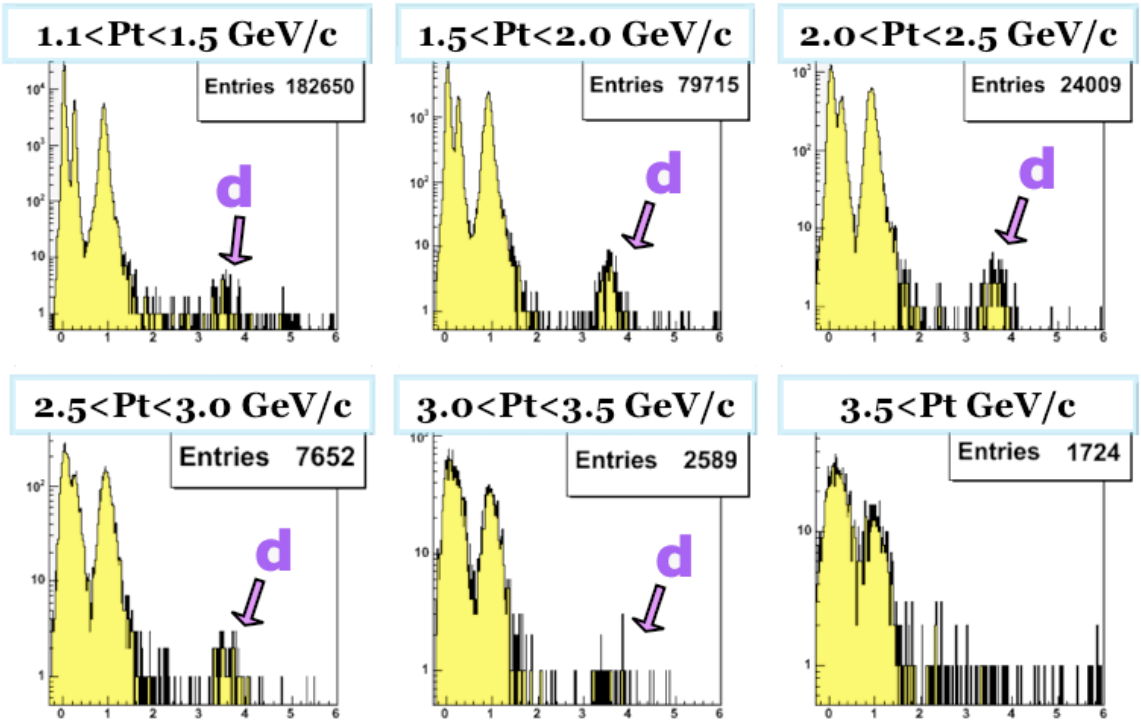

FIGURE 4.6. Deuteron Mass Squared by Momentum

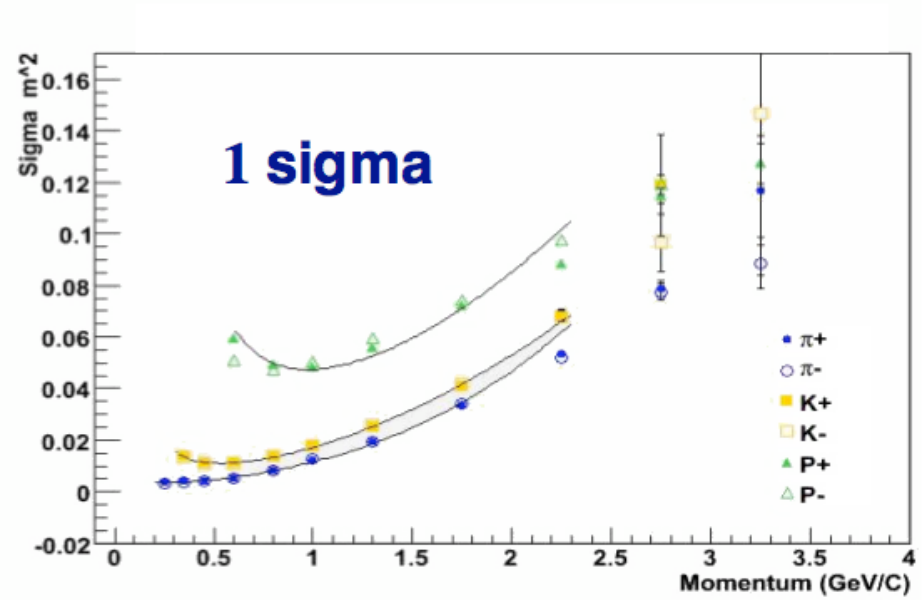

(A) 1 Sigma

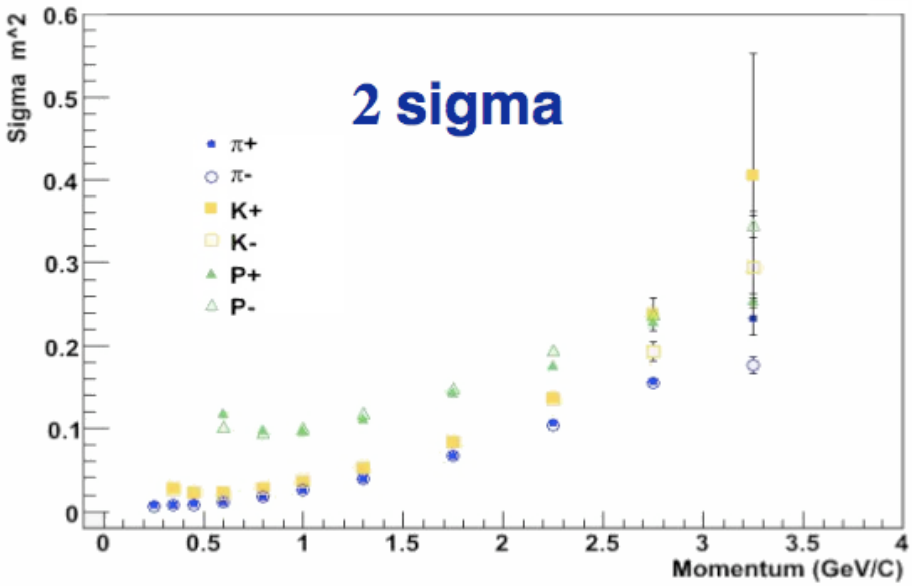

(B) 2 Sigma

FIGURE 4.7. Sigma of Mass Squared

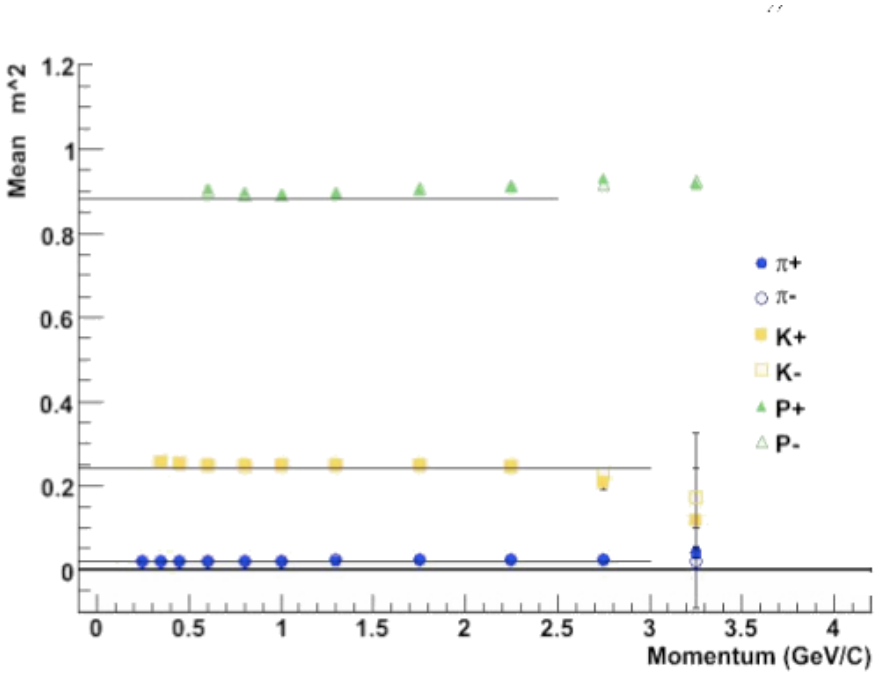

FIGURE 4.8. Mean of Mass Squared

4.3. PID Performance Plots

The experimentally derived time-of-flight PID bands are elegantly expressed in Fig. 4.9 as function of inverse momentum and in Fig. 4.10 and a function of relativistic beta. In addition to pions, kaons, protons and deuterons, the identification of electrons and muons can be seen.

For plotting the TOF PID bands in Fig. 4.9, β is derived from directly measured observables,

$$\beta = \frac{L}{cT_{TOF}} \tag{4.26}$$

In Fig. 4.11, the identification of pions, kaons, and protons from the induced cherenkov radiation in the Aerogel (ACC) detector is shown. The y-axis is the number of cherenkov photons associated with an incident track.

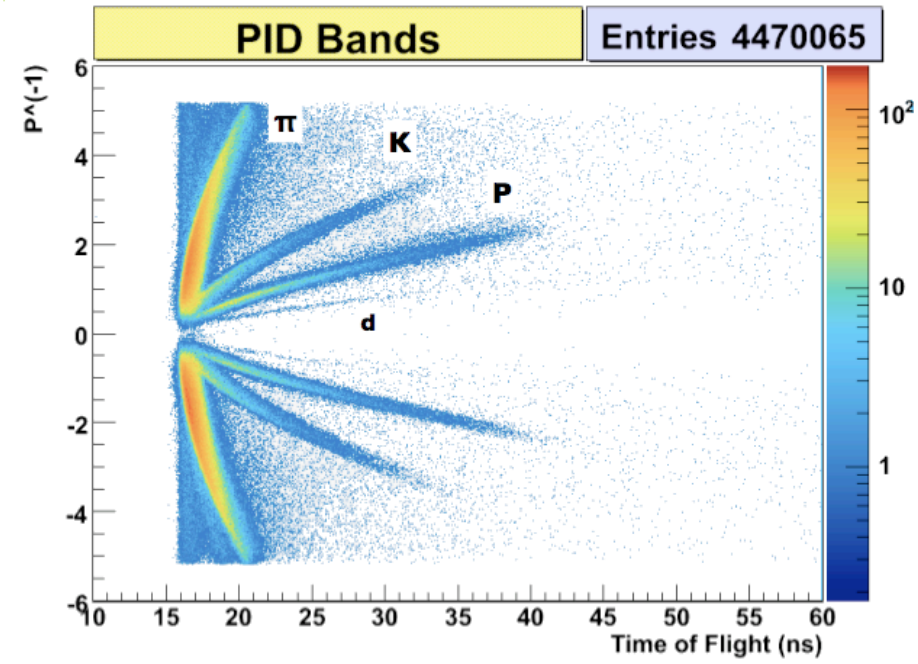

FIGURE 4.9. Inverse $P_t$vs T_{tof} (TOFW)
Positive particles for $\frac{1}{P} > 0$ and negative particles for $\frac{1}{P} < 0$

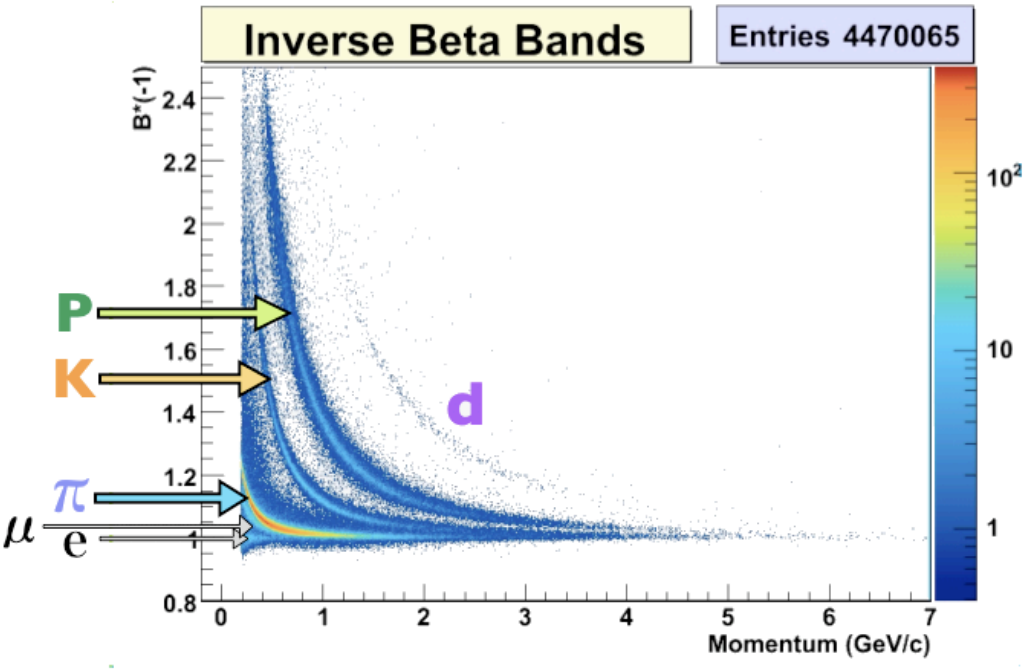

FIGURE 4.10. Inverse β vs P_t

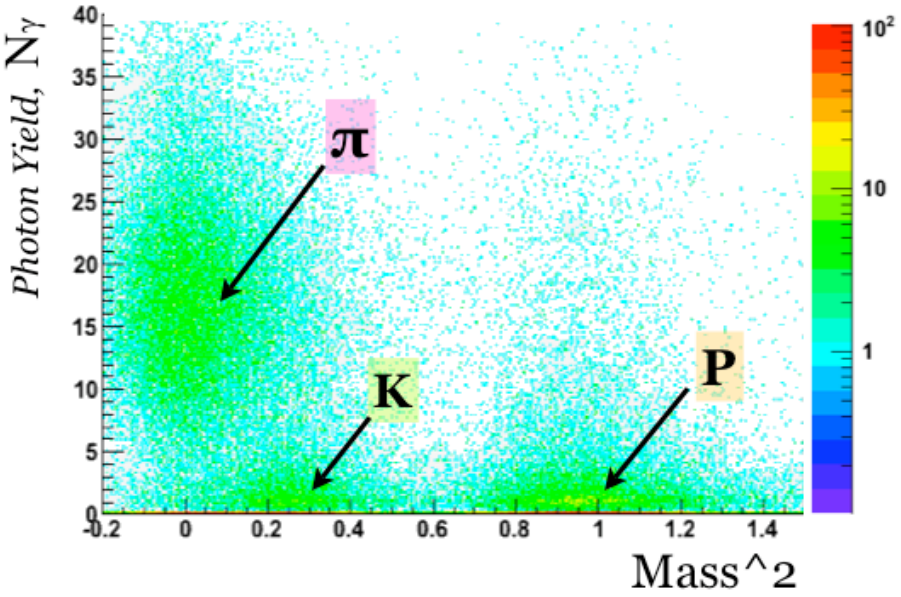

FIGURE 4.11. Aerogel PID $(3 - 3.25\,GeV/c)$

4.4. Other Measurements

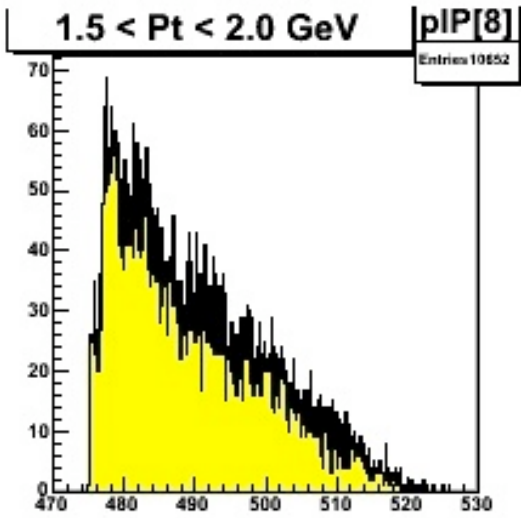

FIGURE 4.12. Reconstructed Path Length from Particle Trajectories Incident on the TOFW

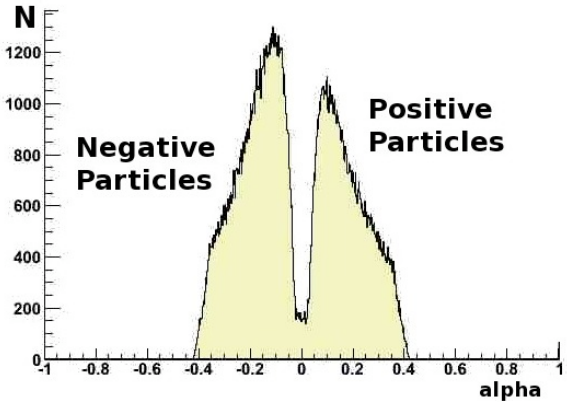

FIGURE 4.13. Alpha Distribution

CHAPTER 5

The Time-of-Flight West Detector Subsystem

The PHENIX collaboration installed in June, 2006 a high-resolution time-of-flight (TOF) detector using Multi-Gap Resistive Plate (MRPC) technology. With a timing resolution performance of $\sigma = 79\,ps$, the use of MRPC detector technology improves upon an existing scintillator based TOF detector ($\sigma_{east} = 96\,ps$) and expands PHENIX PID functionality upto 9 GeV.

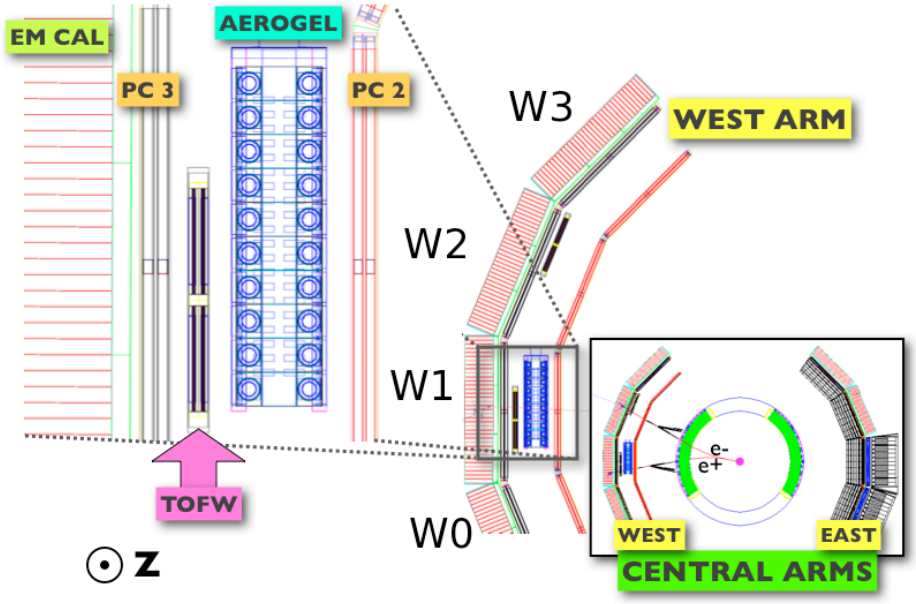

FIGURE 5.1. Cross-Section TOF-West and Aerogel (Sector W1)

5.1. The Multi-Gap Resistive Plate Chamber (MRPC)

The MRPC consists of a gaseous ion chamber subdivided into small independent gas gaps (see Fig. 5.3)[**18, 19, 20**]. The MRPC introduces mechanically several electrically floating (resistive) plates which partition the sensitive gas volume (colored pink, in Fig. 5.3) into small, parallel and uniform gaps. Six of these 230 μm gas-gaps separated by five 550 μm glass plates

constitute the active volume of the detector. When traversing the gas volume, charge separation is induced by minimum ionizing particles, which, when interacting with the gas molecules, generate clusters of electron-ion pairs. For the purpose of signal production, an external high-voltage electric field (14-15 kV) is applied across the active gas volume, with the effect of accelerating these freed electrons (and remaining positive ions) in the direction of the anode (and cathode). The accelerating electrons themselves interact with gas molecules, liberating still more electrons (and positive ions), such that one incident ionizing particle, as a result, induces an avalanche of charge separation. The presence in the avalanche of moving charge generates a signal. Signal extraction is preformed using pairs of copper readout pads, positioned around the gas volume, which, in acting as parallel plate capacitors, are sensitive to the induced current generated by the moving charge in the avalanche. These signals are amplified with on-board electronics. For the detection of incident ionizing radiation, this method of signal production and extraction–by means of induced charge separation and gas-gain–is similar to how other gaseous-ionization detectors operate, such as Geiger counters, proportional tubes, and drift chambers[**21**].

(A) Open MRPC chamber with stack of glass plates separated by fishing line

(B) The Stacking Process

FIGURE 5.2. The MRPC (I)

For reasons that will be discussed, the rise-time of the electron signal in the MRPC is significantly fast, with statistical variations significantly smaller than other implementations of gaseous ionizing detectors, such that, as a result, the MRPC technology provides a high-resolution timing measurement.

In the case of the MRPC, several independent gas volumes are traversed simultaneously, and one incident particle will induce avalanches in each gap (with high probability). The signals from each avalanche are cumulative, and, when read out as collectively, provided a timing measurement

with higher resolution than would otherwise be, without having used the dividing glass plates. The effect of the small gas-gaps is to restrain the size of the induced avalanche of charge, such that the statistical variations that are inherent, which increase with avalanche size, are minimized. Fluctuations in avalanche size (N_e, the number of liberated electrons) increase with d the thickness of the gas gap. They contribute to the statistical variation in rise time of the fast-electron current (the source of the MRPC timing signal). Avalanches grow in space and time, and their size can be modeled as a Poisson process whose variance grows with gap size [see Knoll, [**21**]].

With smaller gas gaps and, thus, smaller avalanches, less current is induced resulting in lower amplitude signals [**22**]. The implementation of a layered multi-gap gas volume, however, compensates for such weak signal limitations. For the MRPC, the extracted signal is the accumulated induced current of all six gas-gaps, whose independence preserves the accuracy of the fast electron signal rise-time. The MRPC combines the high-resolution timing measurement of small gas-gaps but with the signal strength of larger gas-gap RPCs.

To note, for the same statistical reasons governing charge carriers, the signal rise-time of the MRPC-TOF is superior to a scintillator-PMT based time-of-flight detector (such as the TOF-East). Compared to the free electrons in the MRPC gas volume, the mediators of interaction in the scintillator-PMT are the accelerating electrons of the PMT, in which the signal amplification process (or gain) is likewise a stochastic process governed by Poisson statistics.

The MRPC design reduces the intrinsic statistical noise of both single gap RPCs and scintillator based TOF detectors, and delivers a high-resolution timing measurement.

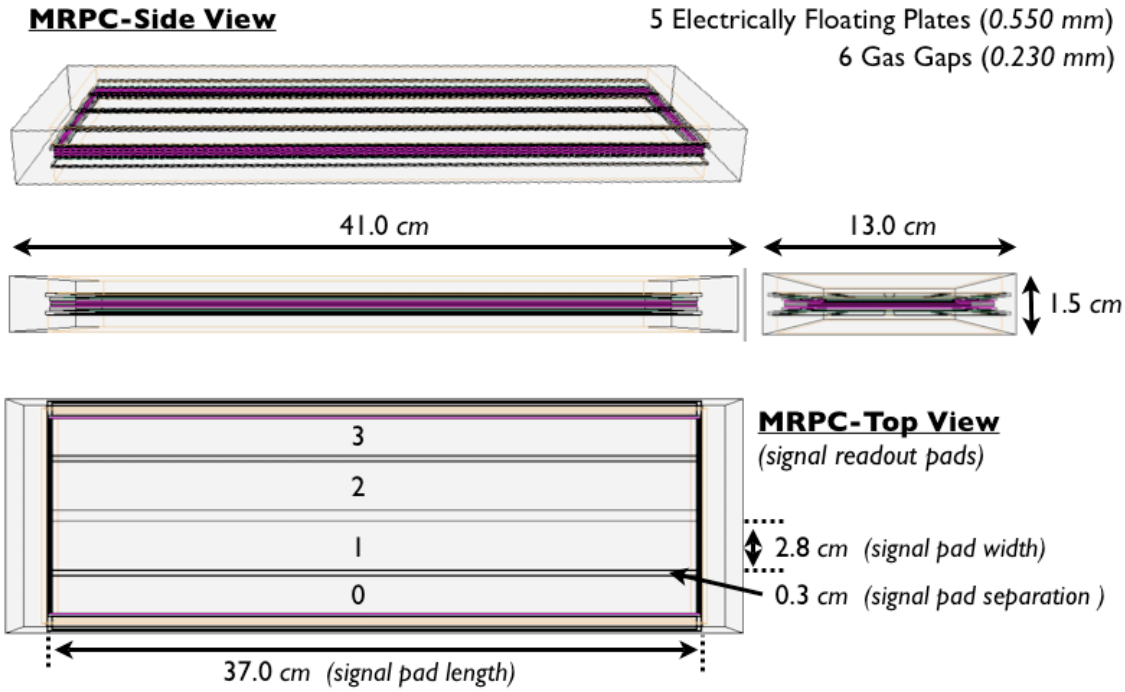

FIGURE 5.3. Schematic Representation of the Multi-Gap Resistive Plate Chamber (PHENIX)

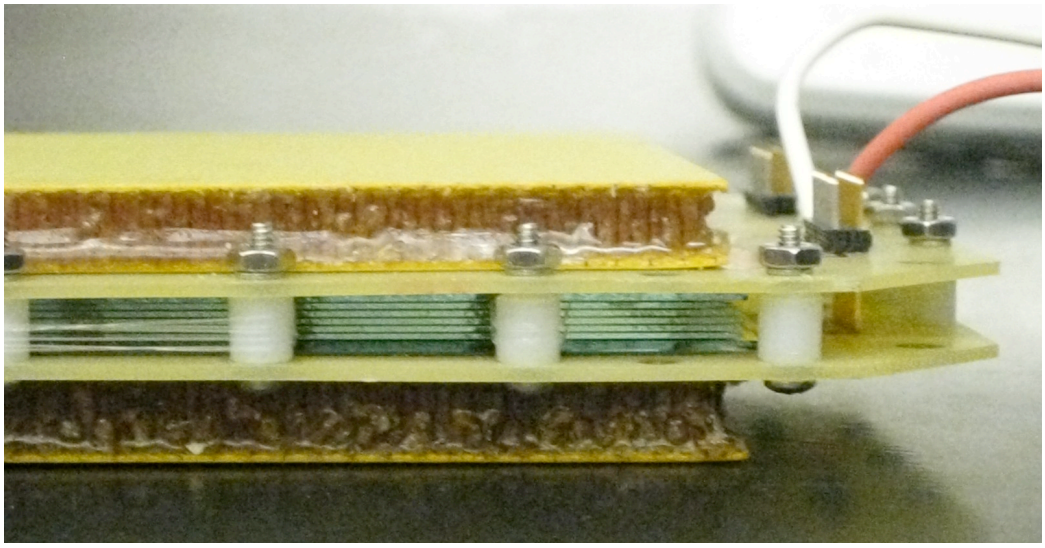

FIGURE 5.4. The MRPC (II)

5.2. The Gas Mixture

As discussed above, the MRPC is a gaseous ionization chamber with parallel plate geometry, where signals arise from the charge separation of ion-induced Townsend avalanches [**23**]. The MRPC operates inside a gas volume[1]. The implementation of the MRPC technology for the PHENIX TOFW subsystem uses a gas mixture of R-134a (1,1,1,2-Tetrafluoroethane or $C_2F_4H_2$, a commonly available generic form of Freon), Isobutane (C_4H_{10} or methylpropane), and Sulfur Hexafloride (SF_6).

Freon is the primary active gas in MRPC and is responsible for the creation of the Townsend avalanche, Fig. 5.5. Freon is a dense gas with a large electron cross section. The density of the gas, because of the small mean free path between molecules, increases the number of electron-molecule interactions (per unit length), as well as improves the probability that the incident ionizing particle will trigger an avalanche when it traverses the gas volume. The large electron cross-section (*i.e.* a high probability of electron-molecule interaction) results in the production of larger avalanches, and thus generating larger signals. Optimal MRPC performance is achieved with 90%-Freon, 5%-Isobutane, and 5%-SF_6[**24, 25**]. However usable MRPC signals can be extracted using Freon alone, which is a helpful procedure to use when testing the MRPC both in the lab and *in-situ*.

Isobutane suppresses the statistical variation in the size of avalanche production, thus improving (by as much as 10 ps) the timing resolution of the detector (see section above, particle identification by time of flight). The Isobutane molecule, $C_2F_4H_2$, has numerous vibrational and rotational degrees of freedom. Isobutane is introduced as a quenching mechanism, whereby lower energy electrons (for example, after scattering off Freon molecules) are absorbed, and their energy expended mechanically (as opposed to ionization). As a result only the fast electrons remain and contribute to the signal. The energy absorption spectrum of Isobutane is limited to lower energy electrons, and has little effect at controlling the large electric discharge in streamer events, for which SF_6 is useful.

While operating the MRPC, charge builds within the detector, and, from time to time, the avalanche triggered by an incident ionizing particle will trigger a massive discharge, sometimes referred to as a spark or streamer, Fig. 5.7. Streamer pulses are characterized both by their large amplitudes (ADC $>$ 600 ch) and by the number of MRPC strips which fire simultaneously. In Fig. 5.7 the decomposition of the ADC spectrum is shown, whereby events are classified according to the number of MRPC strips that fire simultaneously. In each event, only the ADC value from the MRPC

[1]The TOFW gas mixture was 95%-Freon, 5%-Isobutane (for year 2006-08), and 90%-Freon, 4.5%-Isobutane, and 0.5%-SF_6 (for year 2009).

strip with the maximum ADC value is recorded. As can be seen, streamer events are correlated with multiple strip firings.

Sulfur Hexafluroide, or SF_6, is a dense gas with high dielectric properties [**26**]. The small addition of SF_6 to the MRPC gas volume provides increased stability to the ADC spectrum. Fig. 5.7 presents a side-by-side comparison of MRPC ADC spectra with (right) and without (left) SF_6. In the MRPC (at 14kV) the addition of SF_6 clearly suppresses streamer production. The dielectric properties of SF_6 suppress these non-proportional sparks. For example, Tandem Van De Graff accelerators are filled with SF_6 in order to suppress sparks at voltages up to 25 MV. Due to its density–heavier than air–SF_6 is an oxygen deficiency hazard.

In some applications, Resistive Plate Chambers (RPCs) are operated in "streamer" or "spark" mode [**27, 28**], where signal strength and efficiency are high[**21**]. Because streamer events fire multiple MRPC strips simultaneously (Fig. 5.7), however, streamers, or "non-proportional" pulses result in reduced timing resolution. Streamers are violent pulses with large variations in the number of charge carriers and their signal rise time. They can even result in gaseous discharge throughout the entire MRPC chamber, limiting the granulation and tracking matching capability of the detector. Additionally, in streamer mode recovery time is slower, diminishing the detector's rate capabilities [**29**].

The effects of the gas mixture concentrations on the efficiency and streamer production probability are shown in Fig. 5.6. Data was collected using the MRPC in a test bench setup for detecting cosmic rays.

For the purposes of time-of-flight, the MRPC is operated in "proportional" or "avalanche" mode. We require a signal spectrum proportional to energy loss (dE/dx), a detector with good rate capability, as well as a stable signal spectrum and fast signal rise time.

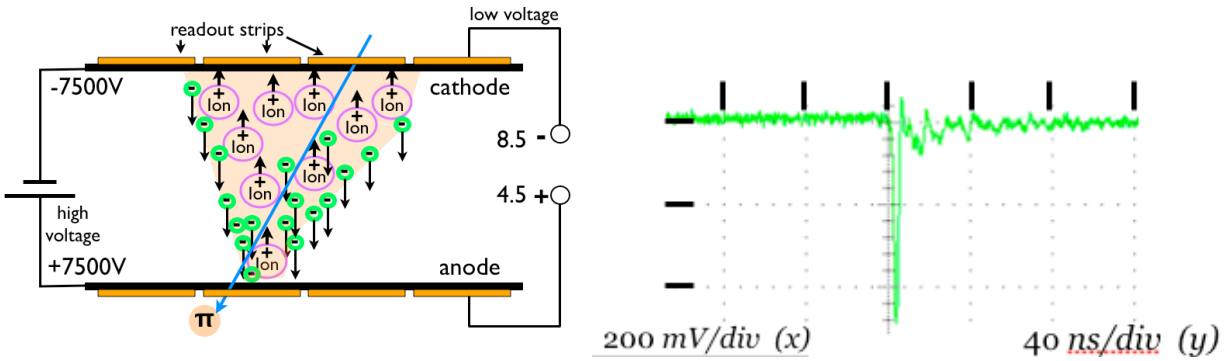

(A) Townsend Avalanche (B) Analog Signal (MRPC FEE Output)

FIGURE 5.5. Charge Separation

Shown here (left) is a schematic representation of charge separation and avalanche induction in a typical gaseous ionization detector with parallel plate geometry. Please note, for illustrative purposes, only one gas gap is shown. In the implementation of the MRPC, six $230\mu m$ are separated by $550\mu m$ glass plates (see Fig. H.1), in which avalanches are produced in each gap. Typical cathode-anode separation is $1-2cm$. Typical gases used are R-134a (a Freon compound, 1,1,1,2-Tetrafluoroethane) for the MRPC and similar Resistive Plate Chambers (RPCs), and Argon/Ethane for wire drift chambers. The high and low voltage settings correspond to the operational values of the TOFW MRPC chamber and FEE boards, respectively.

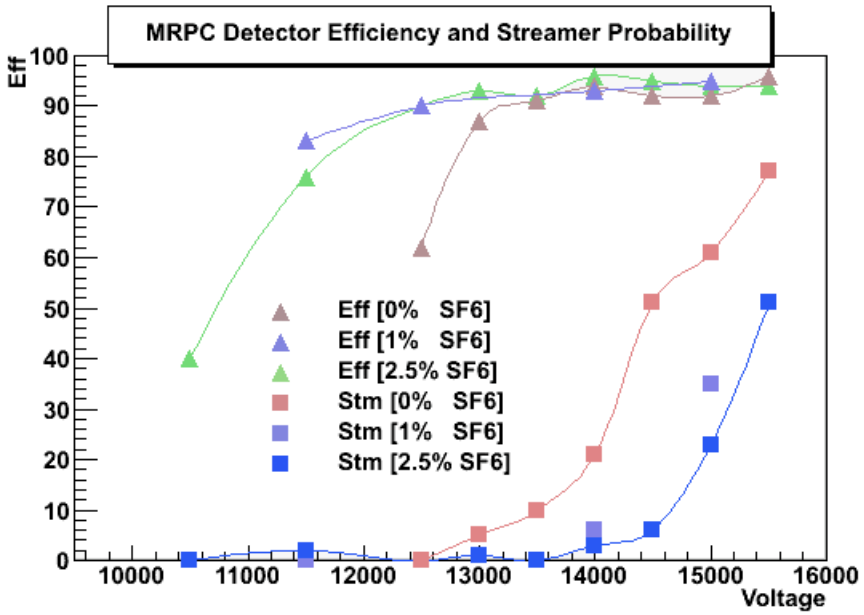

FIGURE 5.6. MRPC Efficiency and Streamer Probability (*Bench Test*)
Data collected from cosmic rays, from a test bench

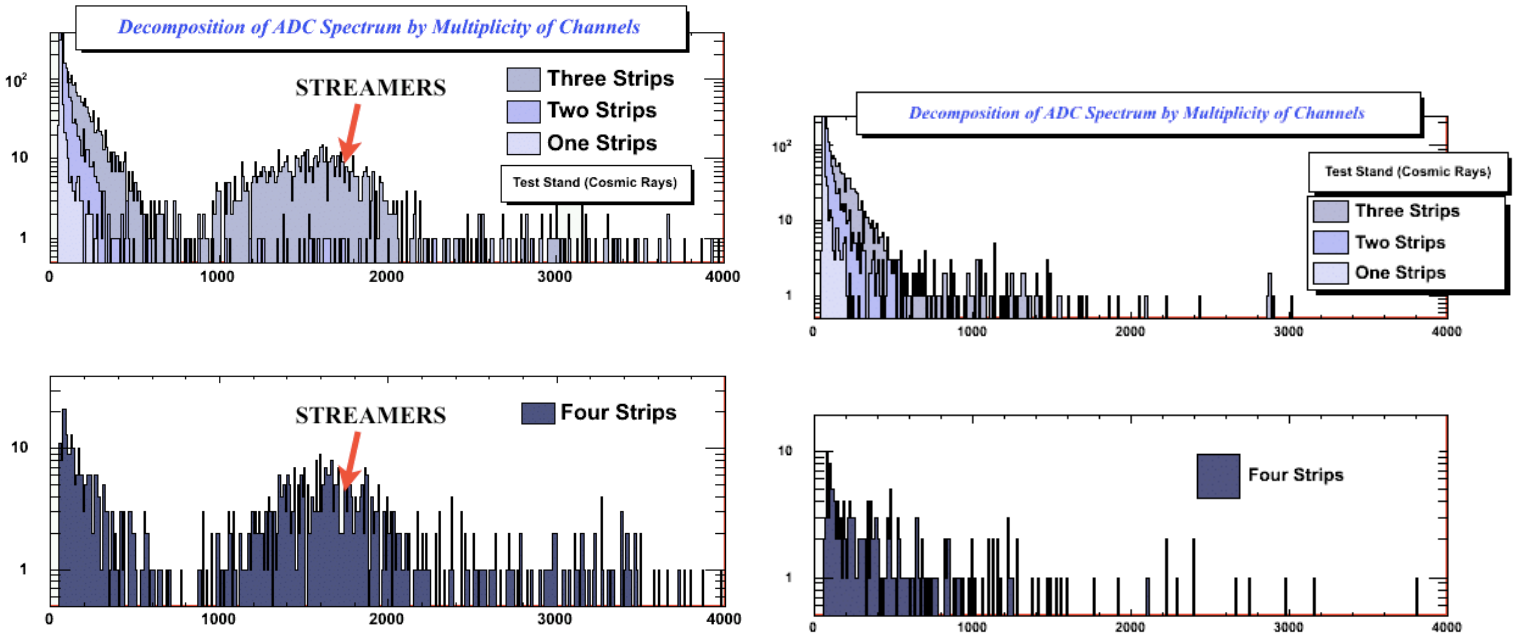

(A) 100%-Freon

(B) 95%-Freon/5%-SF_6

FIGURE 5.7. Stability of the ADC Spectrum
Decomposition of the ADC spectrum by the number of strips firing in each event. Only the ADC value corresponding to the strip with the largest pulse height is recorded in the spectrum. Data collected from cosmic rays, from a test bench. The MRPC was operated with applied voltage of 14kV.

5.3. Assemblage of the Subsystem

The PHENIX Time of Flight West subsystem (TOF-W) is a moderately sized surface area detector. See Table (5.1) for complete TOF-W surface size measurements. The TOFW is approximately 8 m^2 and covers a portion of the PHENIX acceptance comparable to the TOFE (see Fig. 2.2). The fiducial volume of the TOFW covers approximately 20% of the PHENIX west arm. The TOFW spans the rapidity of the PHENIX central arms, $\mid \eta \mid < 0.35$, and is positioned in azimuth $-6.3°(0.110\,rad) < \phi < 3.5°(0.61\,rad)$ and $16.2°(0.283\,rad) < \phi < 26°(0.454\,rad)$. See Appendix B for detailed drawings of the layout of the TOFW detector subsystem.

In total, the TOF-W subsystem is comprised of 128 MRPC chambers, with 4 strips per chambers, where each strip is read out from each end. Of the 128 MRPC units, 32 are installed in each of 4 identical gas boxes. 2 boxes were installed in sector W1, in line with the Aerogel (ACC) detector, and 2 boxes were installed in sector W2, for the purpose of back-to-back jet correlation studies with TOF-E. For the configuration of gas boxes in the west arm see Fig. B.3.

Not all of the TOF-W strips are active. During the commissioning of the TOF-W subsystem, in the summer of 2006, one high voltage bus (in box 0) failed. We believe failure was a result of damage incurred in the installation process of a high-voltage connector mounted on the gas box. So as not to risk compromising the integrity of the air-tight box, no attempt was made to replace the connector *in-situ*. Additionally, in the analysis of *in-situ* performance some channels were found to have reduced efficiency. In some physics analysis it may be desirable to remove these channels from the fiducial volume. The active area surface size of the TOF-W has been computed including and excluding these dead or reduced efficiency strips (see Table 5.1).

The geometric layout of the TOF-W in each sector and in each box (or gas chamber) is identical. Within the gas chamber, with respect to the vertex, the MRPC units are staggered in alternating positions in the radial direction, in order to provide, as near as possible, a seamless fiducial volume (see fig. 5.8). The MRPCs are tightly packed, and the staggering provides sufficient breathability for the gas to flow into and out of the detector units. The gas enters through two long perforated tubes that run the long-axis of the chamber, at the bottom and top. A gas exhausts is located on the exterior side.

TABLE 5.1. Active Area Surface Size

Object (*dimensions in m*)		Formula	$SA_{obj}(m^2)$	$\frac{100*SA_{obj}}{SA_{cylinder}}$	$\frac{100*SA_{obj}}{SA_{west\ arm}}$
Cylinder ($at\ R = 4.77$, $h = 3.85$)		$2\pi Rh$	115.3875	100.00 (%)	~
Sector-Cent. Arm ($at\ R = 4.77$, $l = 1.90$, $w = 3.85$)		lw	7.3150	6.34 (%)	25.00 (%)
West Arm ($at\ R = 4.77$)		$4 * SA_{Sector}$	29.2600	25.36	100.00
Ideal Detector With Full Operability					
TOFW Components	Strip ($l = 0.369$, $w = 0.028$)	lw	0.01033	0.008	0.035
	MRPC (0.37, 0.13)*	lw	0.0481	0.04	0.16
	Box (1.924, 0.926)	$32 * SA_{MRPC}$	1.5392	1.33	5.26
	Sector-TOFW ($2l_{box}$, w_{box})	$2 * SA_{Box}$	3.0784	2.67	10.52
TOF-W (*total*)		$2 * SA_{Sector}$	6.1568	5.34	21.04
Reduced Fiducial Volume From Exclusion of Dead or Inefficient Channels *(see table 5.2)*					
TOFW-Sector 1 (S1)	9 MRPCs + 2 Strips	**	2.56291	2.22	8.76
TOFW-Sector 2 (S2)	3 Strips	**	3.04741	2.64	10.41
TOF-W (*total*)		$SA_{S1} + SA_{S2}$	5.61032	4.86	19.17
	No. of excluded volumes				

**To Note, 4 strips constitute one MRPC. The interval distance between adjacent strips is* $0.3\,cm$.

$^{**}SA = SA_{IdealSector} - N_{ExcludedMRPCs} * SA_{MRPC} - N_{ExcludedStrips} * SA_{Strip}$

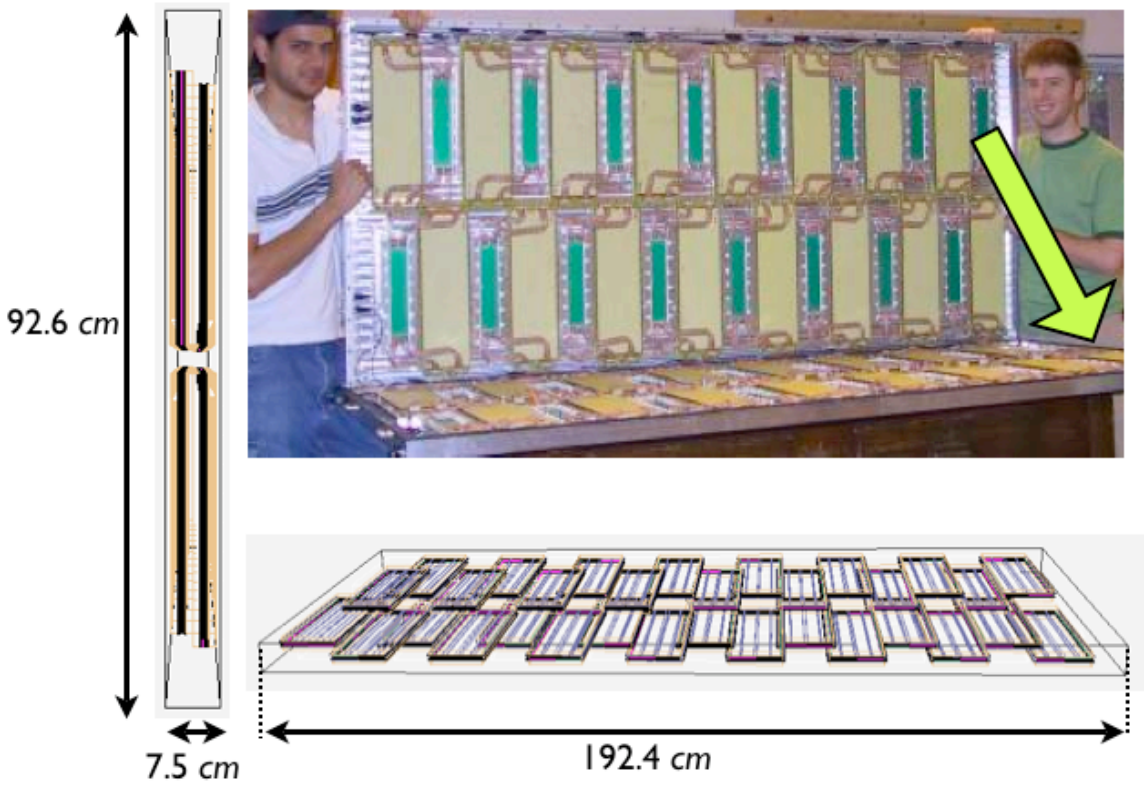

(A) Layout of the MRPCs inside the Gas Box

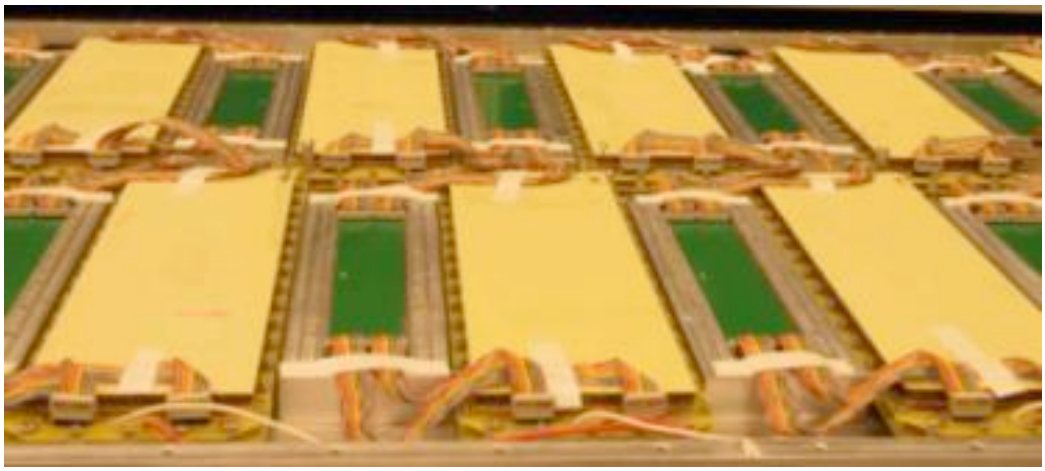

(B) Interior

FIGURE 5.8. The Gas Box
Shown here are 32 MRPCs as positioned in each of 4 gas boxes (each box with identical configuration). 16 MRPCs in the the top half fold down onto 16 MRPCs in the bottom half. The MRPC chambers are staggered in the radial (or, locally, the X) direction in order to obtain a near-seamless fiducial volume in the Z direction. The feed-through boards, on which the pre-amplifying electronics boards are mounted, are in green. 4 ribbon cables on each chamber can be seen. The white daubs are sealant.

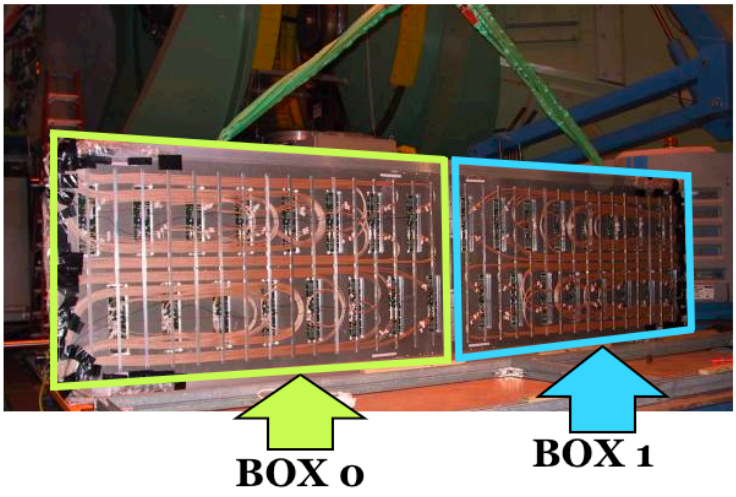

(A) Sector W1 (Photo)

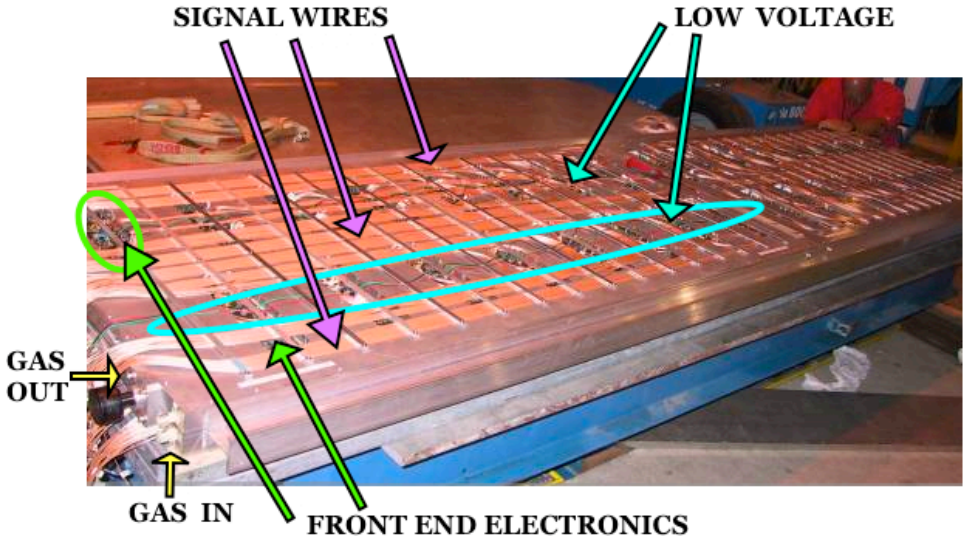

(B)

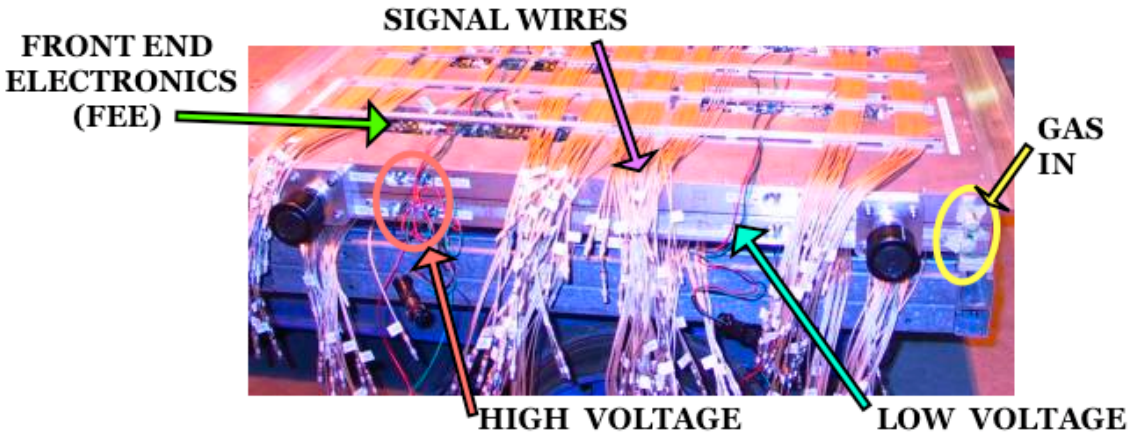

(C)

FIGURE 5.9. Exterior of the Gas Box

TABLE 5.2. Strips Excluded from the Fiducial Volume (valid for year 2007)

Relevant Condition	StripID
High Voltage Bus Failure	4-7, 12-15, 20-23, 28-31, 36-39, 44-47, 52-55, 60-63
Reduced Efficiency	0-3, 19, 161, 372, 394, 460

TABLE 5.3. Configuration: Sector, Box, StripID

Sector	Box*	StripID	Box	StripID
W1	0	0-127	1	128-255
W2	2	256-383	3	384-511

*See Fig. (B.2) for the numbering sequence of boxes within each sector

5.4. Gas System

The total flow rate for the TOFW subsystem (all 4 gas boxes) is 400 *ccm* (cubic-centimeters per minute). At this flow rate, the gas volume refresh rate is 5x per 24 hours. The gas volume of the entire system is 120 liters (or, $1.2e^5$ *ccm*), which corresponds to 30 liters per box. The total input system pressure is 0.4"*w.c.* (inches-water column), which is 1 *mbar* or 0.7 *torr* above standard atm pressure. The gas system has been designed to allow for gas volume recirculation anywhere between 20 to 80%. However, as of year 2009, because of the low flow rate and low relative cost of gas, the gas is not recycled, but vented after output from the detector.

5.5. High Voltage System

The individual MRPC units are powered by 16 high-voltage buses. Each bus powers 8 MRPCs. The high-voltage is applied symmetrically across the detector. The applied electric voltage induces the Townsend avalanche and will affect the gain of the detector. Higher voltages will increase signal amplitude, and thus improve detector efficiency. Gaseous ionization chambers, such as the MRPC, eventually approach a limiting operational range, known as the efficiency plateau, where modulating applied electric field strength has little effect. The plateau is the desired operational range, where temporary fluxes in the electric field, for example from induced charge separation of incident ionizing radiation, will have imperceptible effect on detector performance. The knee of the MRPC efficiency plateau is around 13.5kV, and is dependent on the gas mixture. High concentrations of SF-6 improve efficiency and increase the operational range of the detector. At even higher voltages above the knee of the plateau, increasing applied electric field strength will increase the production probability of low quality non-proportional (or streamer) pulses. The ideal applied voltage, balancing high efficiency

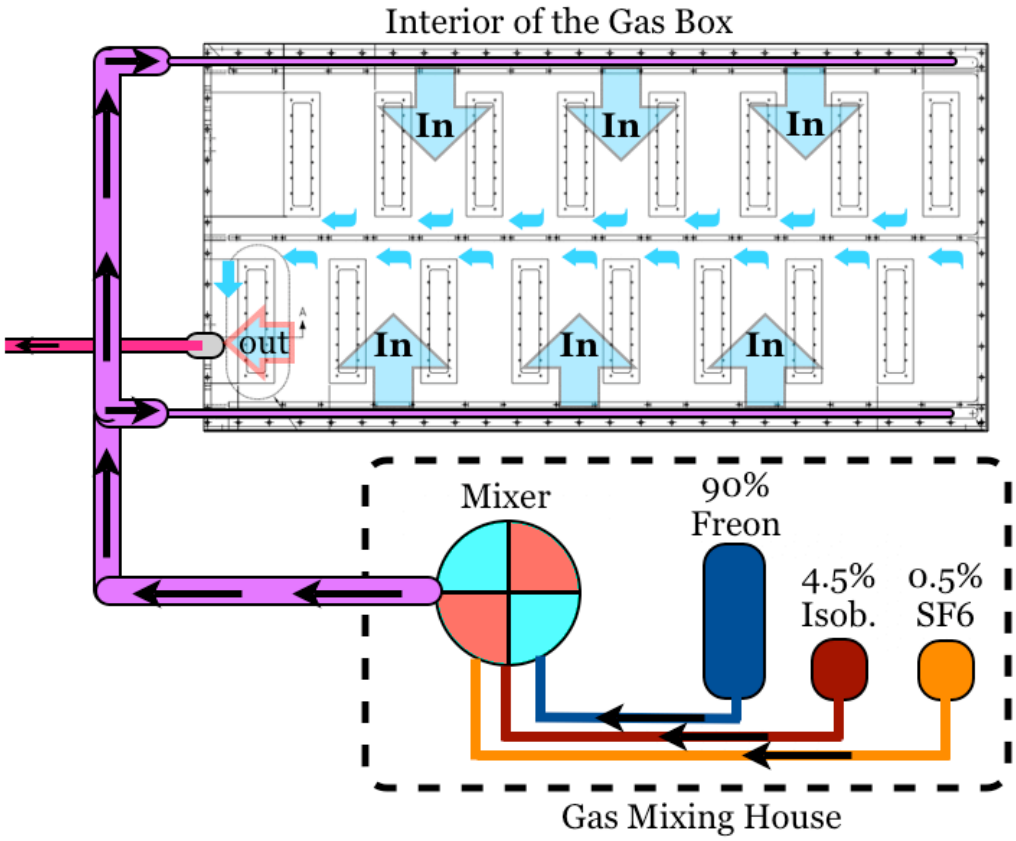

FIGURE 5.10. Gas System
Gas mixture concentrations correspond to year 2009 levels.

and low streamer production, is around 14-15kV, with 90%Freon, 5%Isobutane, and 5%SF6 **[25]**. Year 2006-2009 the TOFW has been operated with a high-voltage of 14kV, applied symmetrically.

5.6. Low Voltage System

Low voltage power supplies are used to power the front electronic boards (FEE). The TOF-West uses 8 low-voltage buses. Each bus powers 16 FEE boards, where each FEE board corresponds to an individual MRPC unit. The FEE low voltage is applied asymmetrically, -8.5V and +4.5V. Typical currents drawn are +4.0A (positive) and 0.8A (negative) *per bus*. This corresponds to 0.25A (positive) and 0.05A (negative) *per FEE board*. The circuity of the FEE is protected from large amplitude input pulses using a Schotky Diode. Nevertheless, it is still recommended that when ramping up or down the MRPC high-voltage, that the FEE boards be powered down such that the risk of spurious large-amplitude signals is minimized.

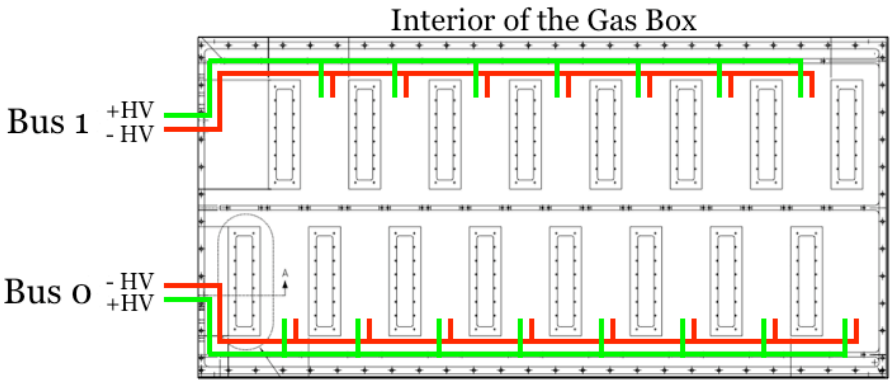

FIGURE 5.11. High Voltage Setup
Year 2006-2009 HV=$\pm 7kV$

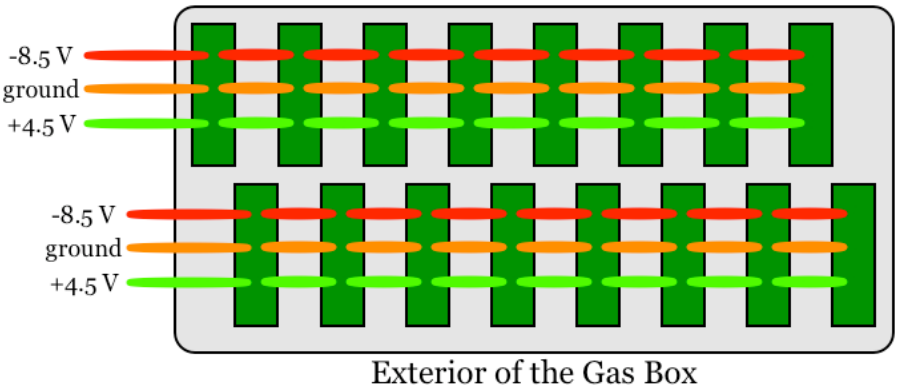

FIGURE 5.12. Low Voltage Setup
The FEE boards are powered in series, with 8 boards to a bus (thus requiring four low-voltage buses per box. The drawing below represents one-half of one gas box. The reverse side is not shown, however the layout is identical. See Appendix for more detailed schematic of the low voltage system.

5.7. Detector Occupancy

The TOFW detector has sufficient segmentation that the probability of multiple tracks incident on the same signal strip is low, shown in Fig. 5.13. The TOFW covers a little less than 8 m^2 in active surface area and is located 477 cm from the beam line. The detector is comprised of 512 strips, each about 0.01 m^2. See Table 5.1 for exact measurements. When the track reconstruction software associates more than one track with a hit in the TOFW, detector efficiency is lost. For events with characteristically higher multiplicity the TOFW has lower reconstruction efficiency. In central collisions more particles are produced than in peripheral collisions. As well, because of the system size of the colliding nuclei, in Au-Au central collisions more particles are produced than in Cu-Cu or d-Au central collisions. Track reconstruction efficiency will be centrality and system size dependent. These effects can be scaled as one effect when considering, N_{part}, the number of participant nucleons between colliding nuclei. The RHIC experiments have found that particle production scales with N_{part} **[3]**. The efficiency of track reconstruction as a function of N_{part} can be studied using embedded simulations, where one simulated track is merged with a real event. From the resulting reconstruction efficiency for the simulated tracks, the centrality and system size dependence of TOFW efficiency can be determined.

The centrality dependence of the TOFW occupancy is shown in Fig. 5.13. Both the number of tracks per event in the west arm only, and the entire central arm (east and west) are shown for comparison. In the most central collisions, corresponding to centrality of 0 to 10%, on the order of 5 to 10 tracks are incident on the TOFW. The multiplicity of tracks incident on the TOFW is one full order of magnitude less than the that of the entire west arm. As well, the track incident track multiplicity of the entire central arm (east and west) is twice that of the west arm, indicating, as expected from the symmetry of the colliding system, that the particle multiplicity is symmetric between the east and west arms. For mid-centrality to peripheral collisions less than one track on average is incident on the TOFW.

Fig. 5.14 shows the fiducial volume of the TOFW in the y and z plane, where y is the local azimuthal direction and z is the beam axis. Tracks are selected from a 2-sigma matching cut on TOFW. The small rectangular patches result from dead areas in the pad chamber tracking system. The alternating white space in the lower left corresponds to the dead high voltage bus (8 MRPC chambers, south box, sector W1). When measuring the TOFW efficiency, for example in order

to obtain correction factors for the absolute normalization of particle spectra, these areas must be excluded from the TOFW fiducial volume. Vertical dark lines represent dead or reduced efficiency areas in the drift chamber.

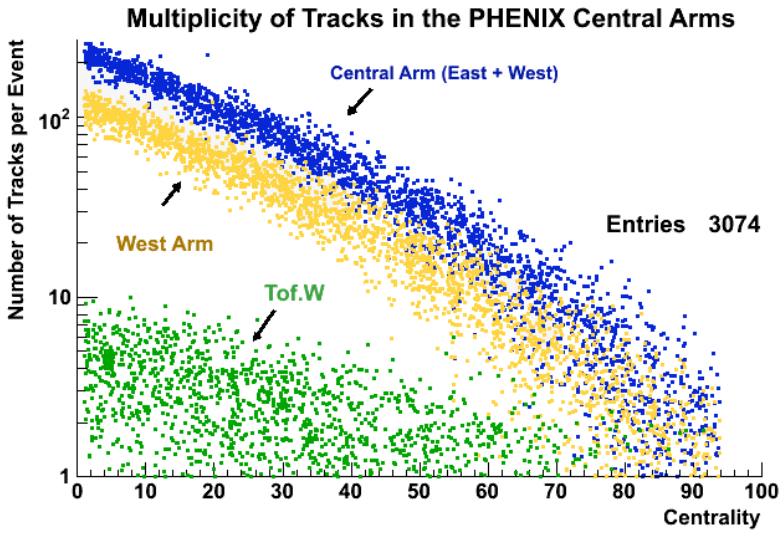

FIGURE 5.13. Multiplicity of Tracks Per Event Au-Au Collisions at $\sqrt{s_{NN}} = 200$ GeV from year 2007 (2-sigma matching cut on TOFW)

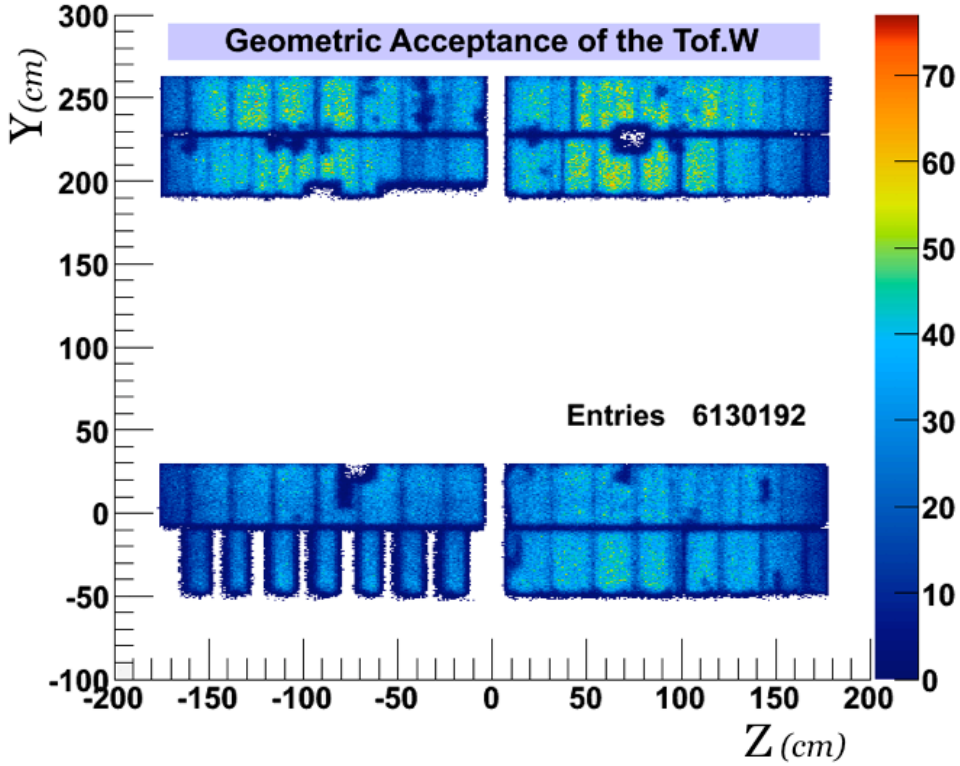

FIGURE 5.14. TOFW Detector Occupancy

CHAPTER 6

Signal Extraction and Processing (DAQ)

Signals from the Multi-Gap Resistive Plate Chamber (MRPC) are measured in time and by pulse height, and the simultaneous extraction of these measurements is described here. The characteristic fast rise time of the MRPC signal provides the desired flight-time measurement through which particle identification is achieved. In addition to the signal timing, the pulse height of MRPC signals provides the ability to compensate for detector behavior, such as the vetoing of low-quality non-proportional (or streamer) pulses and the correction for time-walk resulting from fixed-level discrimination of variable pulse height signals (or slewing effect).

MRPC signal acquisition progresses through a layered-implementation of application specific electronics that integrates low-level signal processing and high-level trigger decision making. Signal processing begins on-board, with the Front End Electronics (FEE) followed by the near-detector Front End Modules (FEM), located in the PHENIX IR and near the central arms, but outside the active volume. Signal processing is completed in the FEMs, where the TOFW data packet is assembled and passed into the PHENIX data acquisition system. Data flows from the FEMs into the PHENIX counting house for final assembly of a complete event (including output from all other subsystems). The TOFW raw data packet is stored in a PHENIX Raw Data File (or PRDF).

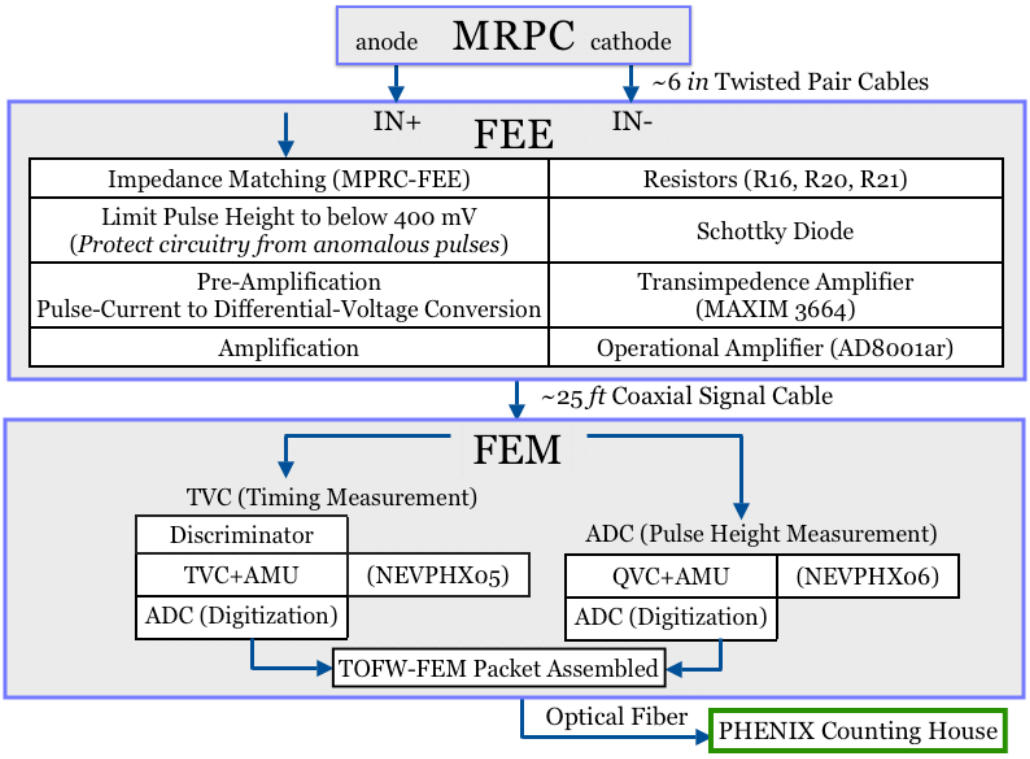

FIGURE 6.1. Signal Processing Components

6.1. Front End Electronics

The PHENIX TOFW Front End Electronics (FEE) boards provide immediate low-level signal processing for the purpose of conveyance of the MRPC raw signal from the detector *in-situ* to the near-detector Front End Modules, which is accomplished through pre-amplification.

In collaboration with the similarly motivated STAR MRPC TOF detector project, we implement an identical FEE electronics circuit [**30**]. The PHENIX MRPC TOF detector subsystem was designed in collaboration with the STAR MRPC TOF detector subsystem, and although differing in their large-area deployment, and with some difference in the exact dimensions of the MRPC chamber itself, the principle design components of the STAR and PHENIX MRPC TOF detectors are identical.

The PHENIX TOFW FEEs are positioned in the active volume of the PHENIX central arms, and, like all non-active materials, contribute to the radiation length of incident tracks and general background contamination. For this reason, as well as constraints from the limited space between the Aerogel and PC3, the FEEs were designed with a low radial profile. The FEEs are mounted

on the exterior of the gas box, in specially designed pockets that complement the staggered layout of the MRPCs inside the gas volume. External mounting allows efficient cooling of the electronics without compromising the integrity of the sensitive gas volume. The FEEs are powered by a low voltage supply.

The FEEs attach to the gas box by means of a feed-through (FT) board. The FT board permanently attaches to the gas box, sealing and ensuring the integrity of the gas volume. By means of the FT board and gas box, the FEEs are grounded. From inside the gas volume, MRPC signals are conveyed to the FT board by means of twisted pair cables ($6in$). One FEE board processes all 8 channels from one MRPC chamber. There are four strips in each chamber, and each end is read out.

The MRPC applied external field, with parallel plate geometry, is operated between $14kV$ to $15kV$ and with an electrode separation distance of $1.5cm$. MRPC signals are read from the signal pad anode, aligned with the applied electric field anode, in order to optimize sensitivity to the fast electron signal, as opposed to the relatively slower positive ion current flux. Input from the signal pad cathode is terminated by a resistor (R16). MRPCs are highly capacitive (10-20pF) **[30]**, and in-series resistors (R20 and R21) provide the needed impedance matching between the MRPC and the FEE circuit. A Schottky Diode provides provides protection from anomalously large-amplitude pulses, cropping pulse-heights above $400mV$, which is about 2x the average MRPC pulse height. The integrated charge of raw MRPC signals is on the order of 50 fC **[30]**. Raw MRPC signals are not large enough to survive the attenuation of the 25 ft of signal cable needed to convey the signals from the detector *in-situ* to the near-detector FEMs. The on-board FEE circuitry provides the needed

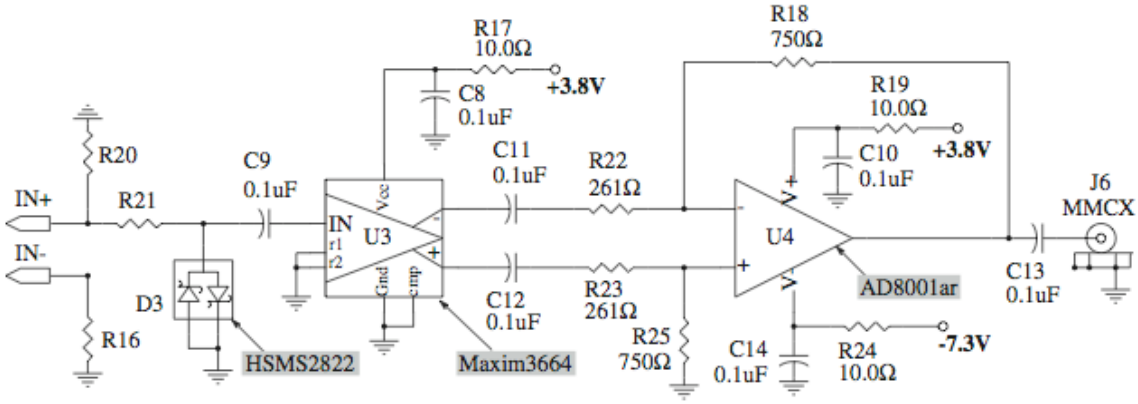

FIGURE 6.2. FEE Circuit Diagram

amplification in a two-stage process.

First, raw signals are passed through a transimpendence amplifier (model Maxim 3664), which transforms the input pulse current into a differential voltage pulse. When an avalanche-induced charge separation occurs in the MRPC, a current flows between the signal pad anode and signal pad cathode. The small-amplitude flux and fast-rise in the current is the origin of the MRPC signal. The transformation from small current flux into an analog voltage pulse constitutes "pre-amplification."

Second, the MRPC pulse is passed through an operational amplifier (model AD8001ar). This amplification provides the needed gain to successfully drive the raw signal to the FEMs. The output gain can been tuned with resistors (R18, R22, R23), and prior to full-installation several levels were tested in order to determine the optimal level. As well, the implementation of the AD8001 circuit includes a resistor modulated feedback network for signal-pulse shaping, such as optimization of fast rise-time and minimization of pulse ringing.

6.2. Front End Module

PHENIX TOFW Front End Modules (FEMs) are application specific electronics modules designed to optimize the high feed-through, low dead time operation of the PHENIX data acquisition system (DAQ). In order to minimize the processing of signals from unneeded events, the FEMs provide integration of low-level signal processing with high-level trigger decision making. This is achieved using low-level multiple event buffering with simultaneous read and write access, as well as logic-driven multi-channel multiplexing.

The PHENIX TOFW FEMs are identical in design to those used for the PHENIX TOF-East subsystem, which subsequently were modeled on the readout architecture of the WA98 experiment's TOF detector. The FEM in general, as well as two ASIC chips (NEVPHX05 and NEVPHX06) were designed at Nevis Laboratories, Columbia University, NY.

Signal processing occurs every clock tick of the RHIC beam. The beam crossing rate is 106 *ns* (9.43 MHz). Each channel of the MRPC-TOF is fed into one FEM channel. There are 16 FEM channels per FEM board. We use 16 FEM boards to process all 1024 MRPC channels, which includes readout and processing of both ends of each of the 512 MRPC strips.

Amplified MRPC signals from the TOFW FEEs are conveyed to the FEMs by *25 ft* of coaxial cable. In the FEM the input signals are immediately split for simultaneous measurement of the signal timing and pulse height. One pulse is passed through a discriminator, with a logic pulse

TABLE 6.1. TOFW Data Packet Members and Derived Quantities

Data Member	Description
Data Packet Members (per channel)	
Q_1	Q_{PRE}
Q_3	Q_{POST}
T_3	T_{MEAS}
Derived Quantities (per channel)	
$Q_3 - Q_1$	Q_{iCH} or "ADC" (chn) Integrated Pulse Height
$T_3 * T_{CONV}$	T_{iCH} or "TDC" (ns)
Derived Quantities (per strip)	
$\sqrt{Q_{UP}Q_{DOWN}}$	Q_{STRIP} Signal Averaging
$(T_{UP} + T_{DOWN})/2$	T_{RAW} Uncalibrated TOF
$(T_{UP} - T_{DOWN})/2$	T_{DIFF} ("Toffset" calibrates mean to 0)
$T_{DIFF} * V_{SIGNAL}$	Y_{POS} Strip Hit Position
Constants	
T_{CONV}	0.028 $ns/channel$ (avg. of strip calibration constants)
V_{SIGNAL}	$0.56C = 16.784$ (cm/ns) Signal propagation speed of the readout pad strips
c	Speed of Light 29.972 (cm/ns)

width duration until the next RHIC clock tick. This uniform-voltage logic pulse is passed to a time-to-voltage (TVC) converter. The TVC voltage is held for one clock tick, followed by a read-out and subsequent reset. The TVC output is stored in one cell of an Analog Memory Unit (AMU). This value is the T_{MEAS} of the signal. The charge, hold, read and reset of the TVC requires three clock ticks.

Concurrent with the timing measurement, the MRPC signal is passed to a charge-to-voltage converter (QVC) for integration of the signal pulse height. Likewise, the QVC output is stored by a dedicated AMU chip. The QVC-AMU chip measures signal pulses on every clock tick.

The integrated switched-capacitor AMU chips have been equipped with multi-event buffering. Each unit holds 4 events, and each event holds 64 cells for signal sampling and holding in memory of up to 64 clock ticks. This buffering is implemented prior to analog signal digitization, which is a relatively time consuming process (800 ns, or 1.25 MHz), and potential data flow bottle neck and source of dead time. The low-level buffering provides operational flexibility for trigger decision making, which can have a high latency relative to the beam clock, such as Lvl-1 trigger-time of 40 clock ticks or 4.25 us. The latency between an event and the trigger decision is managed by the sophisticated buffering and data flow multiplexing of the FEMs.

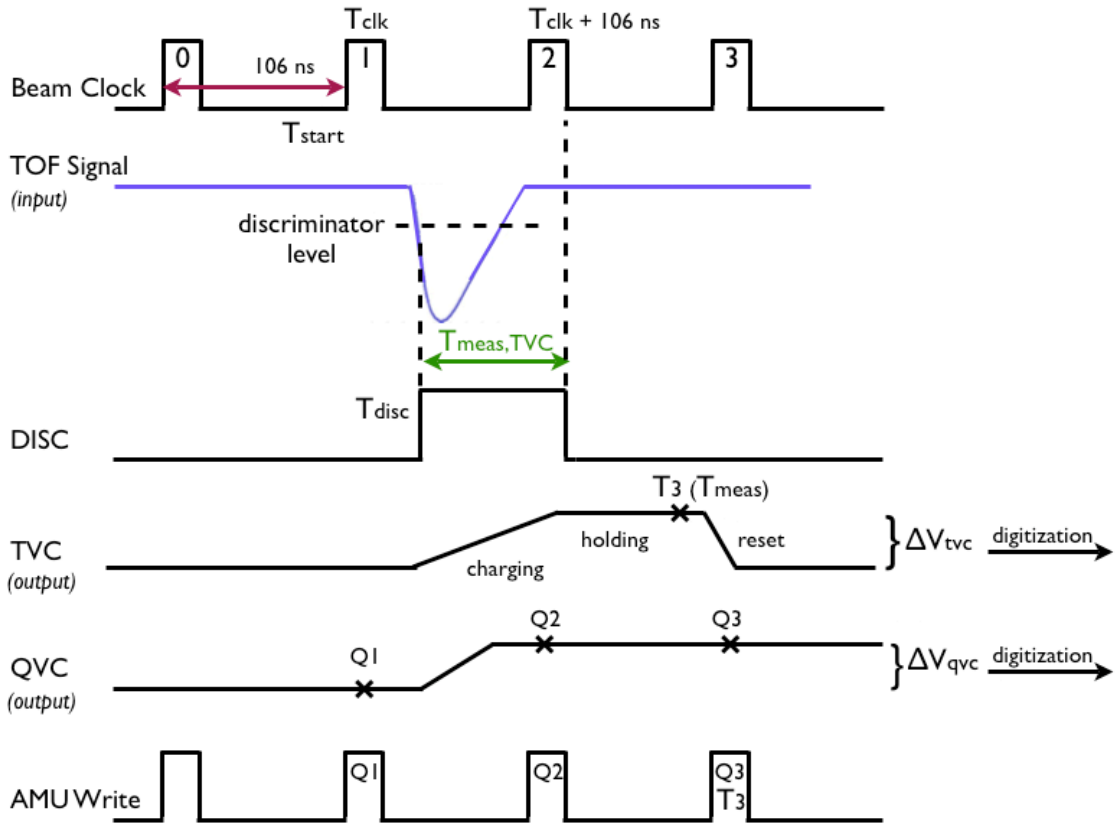

FIGURE 6.3. Signal Processing Sequence for the Front End Module (FEM)

After digitization, the TofW signal values (Q1, Q3, T3) are assembled into a data packet and passed, via optical fiber, to Data Collection Modules (DCMs) located in the PHENIX Counting House. Data packets from all 16 TOFW FEMs are merged and, along with data packets from other subsystems, assembled, event by event, into the PHENIX Raw Data Format (PRDF).

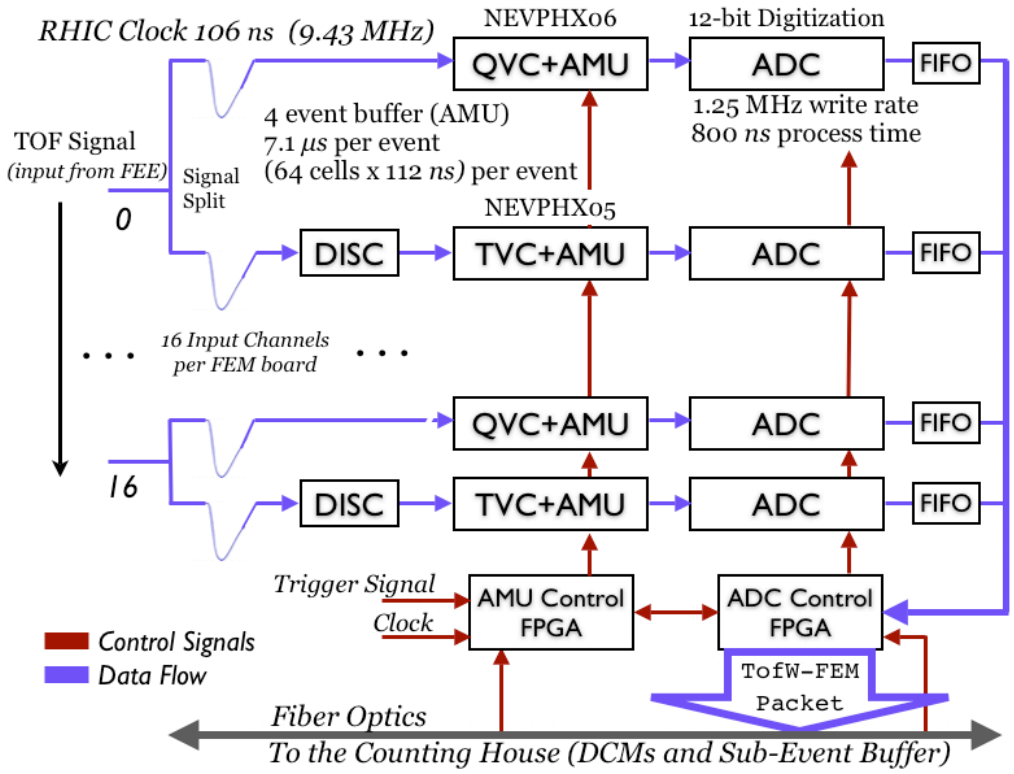

FIGURE 6.4. FEM Data Flow

6.3. DST Data Members

In the production of raw data, PHENIX Raw Data Files (PRDFs), the central arm track reconstruction algorithms associate hits in the TOFW with track projections. For associated hits in the TOFW, the TOFW FEM data is stored in a DST file (data storage file). The DST data members are stored in relation to each event and each track, such that for a given particle track, TOFW information can readily be associated with other detector information, as well as production-level calculations of derived quantities such as momentum and raw track-matching residuals. The TOFW-DST and ACC-DST data members are listed in Table 6.2.

TABLE 6.2. DST Data Members (TOFW and ACC Classes)

Access Method = Class_Name.Data_Member

TofwHits[1]			
rawadc[4][2]	charge[4]	time	nstrip
rawtdc[4][2]	time[4]	boxid	max_strip
xyz[3]	stripid[4]	chamberid	

AccRawHits			
tdc[2]	adc[2]	adc_post[2]	boxid

[1] *ADC and TDC from both ends of all 4 MRPC strips per chamber are recorded for each hit association in the TOFW. The xyz hit position is only stored for the signal strip corresponding to the track association. Charge and time are derived from the ADC and TDC values.*

CHAPTER 7

Schema Evolution of TOFW Class Dependencies (Source Code)

TABLE 7.1. TOFW Calibrations by Method and Implementation Layer

Enumeration			
Type	**Calibration Layer**	**Description**	**Implementation** / **Application**
Channel by Channel			
Timing	Production	Bin size calibration of TVC [FEM]	TofwCalib::getTvcConv()
			TofwEvent::DcmtoRaw()
Run by Run			
Timing	Master Recal	Fine-tuning calibration of the BBC start time, T_0^{OFFSET}	TofwCalib::get_runoffset()
			TofwrecalReco::process_event()
Strip by Strip			
Timing	Production	Set to zero the mean of T_{up}- T_{down} (gross alignment)	TofwCalib::get_toffset()
			TofwEvent::RawtoHit()
Timing	Master Recal	Set to zero the mean of T_{up}- T_{down} (fine tuning)	TofwCalib::get_DeltaT()
			TofwrecalReco::process_event()
Timing	Master Recal	Slewing correction needed to correct small amplitude time-walk that results from leading-edge fixed-level discrimination of variable pulse height spectrum (2-Parameter fit of ADC vs TDC)	TofwCalib::get_Slewing_A() TofwCalib::get_Slewing_B()
			TofwrecalReco::process_event() TofwrecalReco::CalSlewing()
Track Matching*	Master Recal	Set to zero the mean of track matching residuals in ϕ and z	MatchrecalRecoRun7::process_event()
			MatchrecalRecoRun7::process_event()
Track Matching*	Master Recal	Sigma Normalization of Track Matching Residuals in ϕ and z	MatchrecalRecoRun7::CalTofwSigmaPhi() MatchrecalRecoRun7::CalTofwSigmaZ()
			MatchrecalRecoRun7::process_event()

**Momentum dependent (100MeV bins)*

TABLE 7.2. Class Definition and Dependencies in the Schema Evolution of the TOFW Package (Data Production, Calibrations and Simulation)

CLASS NAME	**Description**		
Useful Member Functions	**External Dependencies**		
TOFWPAR.h	Declaration of static global constants pertaining to geometric parameters and enumeration constants.		
TOFWGEOMETRY	Basic Geometry Constructor		
class TofwGeometry	class PHTimeStamp	TofwGeometry.h	PHGeometry.h
TOFWCALIB	Interface to TOFW PHENIX Calibs DB, both production-level and recalibration-level parameters.		
class TofwCalib DB Access (fetch by run, fetch from file) Set/Get Methods DB Update methods	class PHTimeStamp	TofwCalib.h TofwPar.h	RunToTime.hh PdbBankManager.hh PdbApplication.hh PdbCalBank.hh PdbParameter.hh
TOFWEVENT	Data production process whereby PRDF (raw data) are transformed into DST files (processed data). Subsequent high-level implementation of TofwEvent class in true Fun4All framework is performed by TofwReco class. IO stream: input as PRDF, output as DST.root.		
class TofwEvent TofwEvent::DcmToRaw()[1] TofwEvent::RawToHit()[2] TofwEvent::process_event()[3]	class TofwRaw class TofwHit class TofwGeometry class TofwCalib class PHCompositeNode	TofwEvent.h TofwGeometry.h TofwCalib.h TofwRaw.h TofwHit.h	Event.h PHIODataNode.h RunHeader.h

1) Processing of PRDF (raw data), which involves the interpretation of DCM (data collection module) output; the resulting output is a "raw" event
2) Processing of a "raw" hit into a DST (reconstructed) event, includes application of certain production-level calibration parameters
3) Only one implemented Fun4All method (true Fun4All implementation in TofwReco class).

TOFWRECO

High-level implementation of the data production (or reconstruction) process. TofwReco processes the TofwEvent class. TofwReco is an extension-by-method of the TofwEvent class for the purposes of its incorporation within the common PHENIX reconstruction framework.

class TofwReco : public SubsysReco Standard Fun4All Methods	class TofwEvent class TofwGeometry class TofwCalib	TofwReco.h TofwGeometry.h TofwCalib.h TofwEvent.h TofwRawv1.h TofwHitv1.h	SubsysReco.h RunHeader.h recoConsts.h getClass.h PHCompositeNode.h PHIODataNode.h PHNodeIterato.h phool.h

TOFWRAW

Container class for use when manipulating PRDF (raw) data members. Most functions defined *in-line* in versioned header file *TofwRawv1.h.*

class TofwRaw : public PHObject *(virtual base class)*	class TofwSnglRaw *(base)*	TofwRawv1.h *(v1)*	PHObject.h *(b)*
class TofwRawv1 : public TofwRaw *(versioned)*	class TClonesArray *(v1)*	TofwRaw.h *(v1)*	phool.h *(base)*
Set/Get Methods		TofwSnglRawv1.h *(v1)* TofwPar.h *(v1)* TClonesArray.h *(v1)*	

TOFWHIT

Container class for use when manipulating DST data members. Most functions are defined *in-line* in versioned header file *TofHitv1.h.*

class TofwHit : public PHObject *(virtual base class)*	class TofwSnglHit *(base)*	TofwHit.h *(v1)*	PHObject.h *(b)*
class TofwHitv1 : public TofwHit *(versioned)*	class TClonesArray *(v1)*	TofwHitv1.h *(v1)*	phool.h *(base)*
Set/Get Methods		TofwSnglHitv1.h *(v1)* TClonesArray.h *(v1)*	

TOFWSNGLRAW	For consistency with PHENIX schema evolution		
class TofwSnglRaw : public PHObjectclass (*virtual base class)*		TofwSnglRaw.h *(v1)*	
class TofwSnglRawv1 : public TofwSnglRaw *(versioned)*			
Set/Get Methods			

TOFWSNGLHIT	For consistency with PHENIX schema evolution		
class TofwSnglHit : public PHObjectclass (*virtual base class*)		TofwSnglHit.h *(v1)*	
class TofwSnglHitv1 : public TofwSnglHit *(versioned)*			
Set/Get Methods			

TOFWSIMEVENT	Implementation of the sim-production chain for simulated inputs (managed by the Fun4All framework) and simulated outputs. Similar to the TofwEvent class. IO stream: input as PISA hits file (PISAEvent.root), output as simDST.root.		
class TofwSimEvent	class TofwRaw	TofwSimEvent.h	Event.h
TofwSimEvent::PisaToRaw	class TofwHit	TofwRaw.h	getClass.h
TofwSimEvent::RawToHit	class TofwGeometry	TofwHit.h	PHIODataNode.h
Standard Fun4All Methods	class PHCompositeNode	TofwGeometry.h	RunHeader.h
	class TfwPISAHit	TfwPISAHit.h	gsl/gsl_randist.h
		tfwghitWrapper.h	gsl/gsl_rng.h

TFWSIMRECO	Implementation of the TofwReco functionality for simulated events. SimReco processes the SimEvent class as TofwReco processes TofwEvent.		
class TfwSimreco : public SubsysReco	class TofwSimEvent	TfwSimreco.h	PHCompositeNode.h
Standard Fun4All Methods	class TofwGeometry	TofwSimEvent.h	PHIODataNode.h
	class TofwHit	SubsysReco.h	PHNodeIterator.h
	class TofwRaw	tfwghitWrapper.h	recoConsts.h
	class tfwghitWrapper	TfwGetGEA.h	phool.h
	class PHCompositeNode	TofwHitv1.h	
		TofwRawv1.h	
		TofwGeometry.h	

TFWPISAHIT	Container class for TOFW PISA hits, which result from simulated inputs such as Exodus (single particle) or HIJING events.		
class TfwPISAHit : public TObject		TfwPISAHit.h	TObject.h

MATCHRECALRECORUN7 — Track matching recalibration using the Run7 (year 2007) detector configuration for DC/PC1, PC2, TOFW, TOF(East), and EMCAL

class MatchrecalRecoRun7 : public Recalibrator Standard Fun4All Methods MatchrecalRecoRun7::InitPars()**	class PHCompositeNode	MasterrecalRecoRun7.h Recalibrator.h PHCentralTrack.h PHSnglCentralTrack.h	PHGlobal.h PHCompositeNode.h RunHeader.h getClass.h

**Massive *in-line* declaration of calibration parameters (mean and sigma of residuals, for positive and negative charge, for +- and -+ field, in z and phi).

RECALIBRATOR — Implementation interface between individual recalibration modules (e.g. MatchrecalRecoRun7 and TofwRecal) and the MasterRecalibrator class.

class Recalibrator : public SubsysReco	class MasterRecalibrator	Recalibrator.h MasterRecalibrator.h	SubsysReco.h

MASTERRECALIBRATOR — Ordered high-level implementation in the Fun4All framework for all recalibration modules (e.g. matching, momentum, tofw, tof, emcal, etc.)

class MasterRecalibrator : SubsysReco Standard Fun4All Methods

TOFWRECALRECO — Implementation of Tofw recalibration parameters (see Table 7.5).

class TofwrecalReco : public Recalibrator Standard Fun4All Methods DB Access (fetch by run, fetch from file) Set/Get	class TofCalib class PHCompositeNode	TofwrecalReco.h Recalibrator.h TofwPar.h TofwCalib.h PHCompositeNode.h	RunHeader.h PHCentralTrack.h PHSnglCentralTrack.h getClass.h PdbBankManager.hh PdbApplication.hh PdbCalBank.hh PdbParameter.hh RunToTime.hh

TABLE 7.3. Source Code Location in the PHENIX Repository

Location	**Function**	**Source Code**	
offline/packages/tofw	Geometry Enumeration Data Production Calibration Simulation	TofwCalib.C TofwEvent.C TofwGeometry.C TofwHit.C TofwHitv1.C TofwRaw.C TofwRawv1.C	TofwReco.C TofwSnglRaw.C TofwSnglRawv1.C TofwSnglHit.C TofwSnglHitv1.C TofwSimEvent.C TfwSimreco.C
offline/framework/recal	Calibrations	TofwrecalReco.C MatchrecalRecoRun7.C	Recalibrator.C MasterRecalibrator.C
simulation/pisa2000/src/tfw	Simulation	Tfw.f Tfw_digi.f	Tfw_gustep.f
simulation/pisa2000/src/root	Simulation	TfwPISAHit.f	
online/monitoring/Run3/subsystems/tofw	Online Monitoring	TOFWMon.C *macros*	TOFWMonDraw.C
online/calibration/onlcal/subsystems/tofw	Online Calibrations	TofwCal.C TofwCalDefs.h	TofwDraw.C

TABLE 7.4. GEANT Implementation of the Tof-West Detector (PISA)

TFW.F	Construction of all detector volumes, active and inactive components; layout of a hierarchical structure for nested (embedded) volumes; declaration of material types; and, placement of the detector within the PHENIX mother volume.
TFW_DIGI.F	Subroutine: Manages IO for recording hit information.
TFW_GUSTEP.F	Subroutine: Called for each time step of the simulation
TfwPISAHit.f	Container class for PISA (GEANT) hits

TABLE 7.5. Structure of the TOFW Calibrations Database

Calib.Tofw.Stripbystrip

index	0 (Schema)	1 (nEntries)	2-9(data)	10-3594(data)
	1	3592	sigma_dphi[4]* sigma_dz[4]*	deltaT [512] slewing_a [512] slewing_b [512] mean_dz_plus [512]* mean_dz_minus [512]* mean_dphi_plus [512]* mean_dphi_minus [512]*

Calib.Tofw.Toffset

index	0(Schema)	1(nEntries)	2-514(data)
	1	512	toffset [512]

Calib.Tofw.Tdc

index	0(Schema)	1(nEntries)	2-514(data)
	1	512	TvcConv [512]

Calib.Tofw.Runoff

index	0(Schema)	1(nEntries)	2(data)	3(data)
	1	2	runnumber[1]	runoffset[1]

*Although stored in the DB, these calibration parameters are implemented without using a db call, using *in-line* data declarations in MatchrecalRecoRun7 class (year 2007).

CHAPTER 8

Calibration

Full realization of detector performance is achieved with the implementation of *in-situ* calibrations. Calibration of the direct timing measurement from the TOFW corrects for slight variations of physical detector components, such as each channel's signal cable length and time-walk effects of the pulse-height spectrum (slewing effect). Derived measurements also require calibration, such as in calculating the time-of-flight where fine-tuning adjustments to the start time are included. Additionally, residuals from the track reconstruction projections onto the TOFW are normalized, which provides a measure of the quality of the incident track, useful for rejection of background contamination and spuriously reconstructed tracks.

The TOFW calibration schema, consistent with other PHENIX detector subsystems, involves two layers, the storage of the calibration parameters themselves and the implementation of the calibration methods. In PHENIX calibrations are stored in an SQL relational database, for which all database entries are defined corresponding to a valid run number, or range of run numbers. Calibration methods are implemented in the Fun4All framework, where the matching of relevant parameters to matching runs is managed on the back-end. The deployment of both layers of the TOFW calibration schema is described here.

Access to calibration parameters stored in the PHENIX calibrations database (or federation, to be pedantic) are managed by the interface class, TofwCalib. With standard *set*, *get* and *fetch* functions, the TofwCalib class provides a database implementation layer that can be managed independently of other components of the TOFW package. TOFW calibration parameters are grouped into four databases, whose contents and data structure is described in Table 7.5. One exception to using the TofwCalib database access method for retrieval of calibration parameters is in the track-matching residual normalization process, whose parameters are stored in-line in the MasterrecalRecoRun7 class.

Method implementation of the TOFW calibrations proceeds in two levels: the production level where raw data (PRDFs) are processed (including event and track-by-track reconstruction), and

the analysis level where post-production calibration parameters are applied for normalization and fine-tuning of data members. Both calibration levels use the common PHENIX data processing framework, Fun4All, for event by event processing. Production level calibration methods are implemented in the TofwEvent class. High-level calibration methods (analysis-level) are implemented in the TofwrecalReco and MatchingrecalRecoRun7 classes, both of which are components of the PHENIX master recalibrator framework.

8.1. Strip End Timing Offset T_{DIF}^{OFFSET}

The difference in timing measured from opposite ends of a MRPC strip provides positioning in the ϕ (azimuth, or local Y) direction.

$$T_{DIF} = T_{up} - T_{down} \tag{8.27}$$

$$\Delta Y = \frac{T_{DIF}}{2} * V_{SIGNAL} \tag{8.28}$$

where, $\triangle Y$ is the displacement from the strip center and V_{SIGNAL} is the constant signal propagation velocity of the MRPC readout pad, given in Table 6.1. Calibration of T_{DIF} improves the precision of TOFW hit positioning in ϕ, which reduces the distribution width of the track-matching residuals– the difference between the TOFW internal hit-positioning and the externally reconstructed track projection. This is useful because tighter track matching improves background rejection, including the elimination of spuriously reconstructed tracks.

For the ideal detector, T_{DIF} is uniformly distributed with mean centered at zero (the center of the strip) and width (from center) defined by the length of the strip,

$$\mid T_{DIF} \mid = \frac{L_{STRIP}}{V_{SIGNAL}} \tag{8.29}$$

$$T_{DIF}^{TOFW} = \frac{37cm}{16.784cm/ns} = 2.2ns \tag{8.30}$$

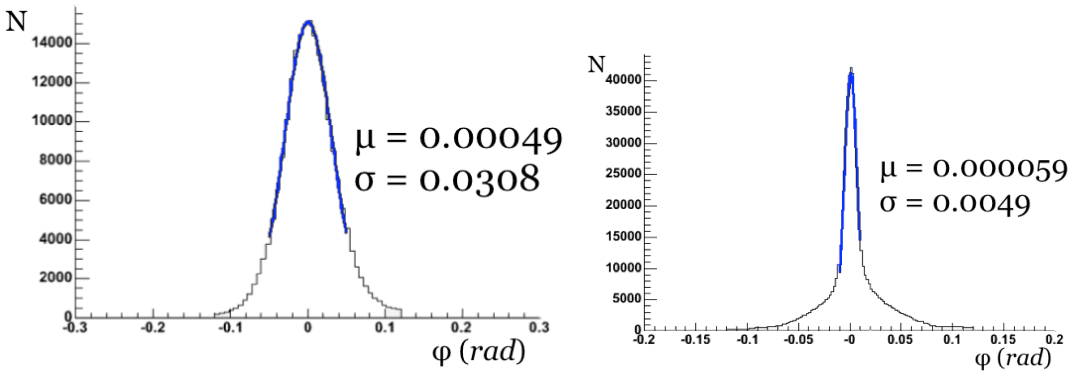

(A) Before $T_{up} - T_{down}$ Calibration (B) After $T_{up} - T_{down}$ Calibration

FIGURE 8.1. Track Matching Residual in ϕ (azimuth)

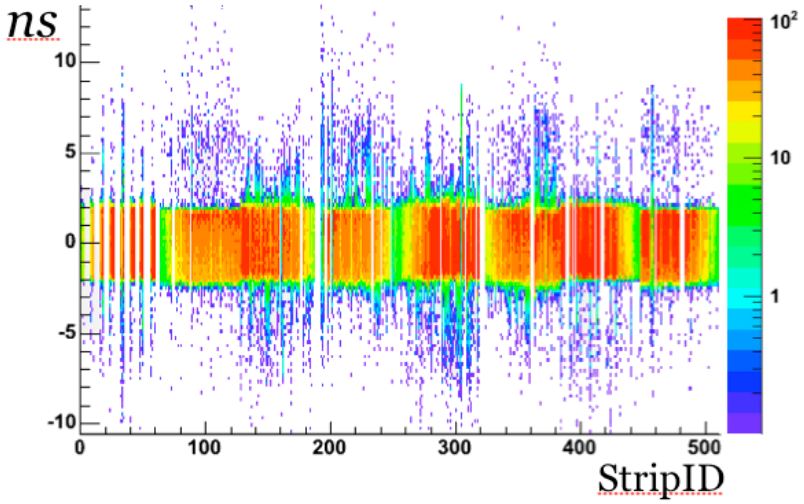

FIGURE 8.2. Calibrated $T_{up} - T_{down}$

The strip end timing offset value, which is the mean of the T_{DIF} distribution, is calculated for each strip. This offset value, T_{DIF}^{OFFSET}, at the analysis-recalibration level is subtracted from the raw time-of-flight measurement, $T_{TOF,MEAS}$. The post-calibration distribution of T_{DIF} by strip number is shown in Fig. 8.2. As expected the width of T_{DIF} is 2.2 *ns*, corresponding to the length of the MRPC signal readout strip. As well, Fig. 8.2 visualizes the full illumination of the TOFW detector in ϕ.

The resulting improvement in the TOFW hit-positioning in ϕ, seen in the narrowing width of the track matching residuals, is shown in Fig. 8.1.

8.2. Fine-Tuning of the BBC Start Time–"Time-Zero Offset" T_0^{OFFSET}

The time-of-flight, $T_{TOF} = T_{START} - T_{STOP}$, is a measure of the flight time of a particle from the vertex of the collision to the time-of-flight detector. T_{START} is measured by the Beam-Beam Counters and T_{STOP} is measured one of three time-of-flight detectors. PHENIX Time of flight measurements can be made with the EMCAL ($\sigma_{TOF,EMCAL} = 450ps$), TOF-East ($\sigma_{TOF,EAST} = 96ps$), and TOF-West ($\sigma_{TOF,WEST} = 79ps$). Event-by-event subtraction of the BBC start time, T_{START}^{BBC}, from $T_{TOF,MEAS}$ is implemented in the Bbcrecal class of the PHENIX master recalibrator (Fun4All framework). Not compensated for in T_{START}^{BBC} are slight drifts in the beam position throughout a store that subsequently induce slight systematic deviations in the measured start-time with respect to the RHIC beam clock. T_0^{OFFSET} is a run dependent fine-tuning correction for these variations. The T_0^{OFFSET} is obtained by fixing to zero the mean of the $T_{TOF,MEAS} - T_{TOF,EXPECTED,\pi}$ for 1.1GeV/c $<$ P $<$ 1.2 GeV/c. These T_0^{OFFSET} corrections are implemented for the TOFW in the TofwrecalReco class of the PHENIX master recalibrator.

8.3. Slewing Correction T_{SLEW}

The TOFW timing measurement is extracted from leading-edge fixed-level discrimination of variable amplitude analog signals. As shown in Fig. 8.3, smaller amplitude pulses, because of their shape, will trigger the discriminator at a later time than larger amplitude pulses when both are coincident in time. This pulse shape distortion on the timing distribution induces a charge-dependent time-walk, or slewing, that predominates at low values of the pulse height spectrum. This slewing effect is an intrinsic bias of the detector. It is corrected for in the form of a charge dependent timing offset (strip-by-strip).

The average integrated charge of one MRPC strip is given by,

$$ADC \text{ or } Q_{STRIP} = \sqrt{Q_{UP}Q_{DOWN}} \tag{8.31}$$

The charge dependent slewing correction, in the form of a timing offset, is given by,

$$T_{SLEWING} = A + (B/Q_{STRIP}^{0.4}) \tag{8.32}$$

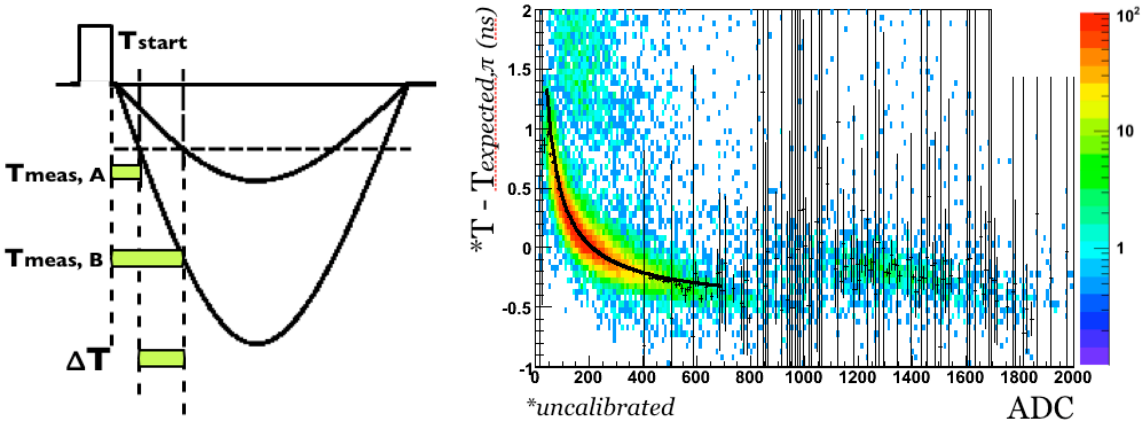

(A) Small Pulse Height Induced Time Walk

(B) ΔT vs. ADC

FIGURE 8.3. Time Walk or Slewing

where A and B are two parameters extracted from a two-parameter fit of TDC vs ADC. The slewing correction procedure for the TOFW fits $T - T_{EXP,\pi}$ vs ADC.

The time-walk calibration improves the timing resolution of the detector, which can be seen in the $T - T_{EXP,\pi}$ distribution for particles with momentum 1.1 GeV/c $<$ P $<$ 1.2 GeV/c, as shown in Fig. 8.4. In this momentum range, the width of $T - T_{EXP,\pi}$ is a valid approximation of the effective timing resolution of the MRPC detector, $\sigma_{TTOF,MEAS}$. After applying the slewing correction, the effective timing resolution of the TOFW is 0.079 ns Fig. 8.4. We can deduce the intrinsic timing resolution of the TOFW detector from $\sigma_{TTOF,EFFECTIVE}$ and σ_{T0} . The measured errors are related in quadrature as follows,

$$\sigma_{TTOF,EFFECTIVE} = \sqrt{\sigma^2_{TTOF,INTRINSIC} + \sigma^2_{T0}} \tag{8.33}$$

T_0 is measured by the Beam-Beam Counters with a resolution of 0.040 ns.

$$\sigma_{TTOF,INTRINSIC} = \sqrt{(0.079)^2 - (0.040)^2} = 0.0693\, ns \tag{8.34}$$

The extracted intrinsic timing resolution of the TOFW is givin in Eq. (8.34).

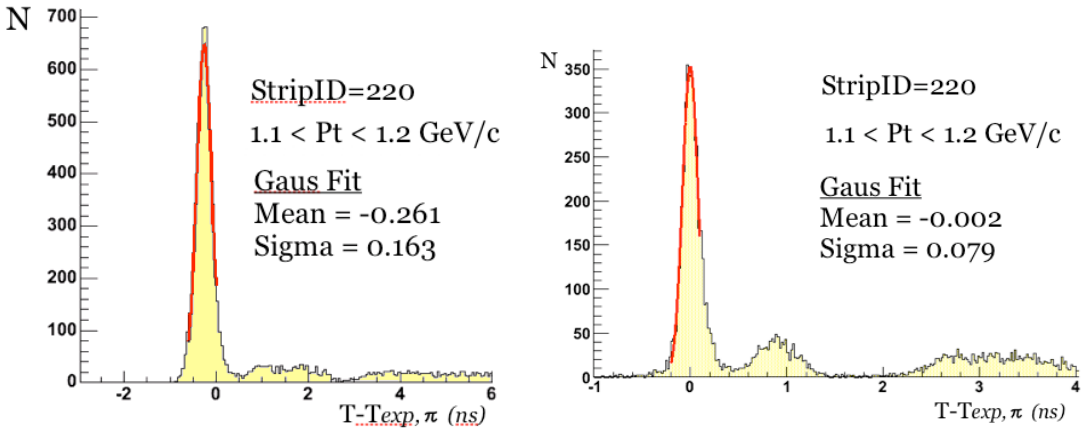

(A) Before (B) After

FIGURE 8.4. Slewing Correction Effect on $T - T_{exp,\pi}$

$$T_{TOF,CALIBRATED} = T_{TOF,MEAS} - (T^{OFFSET}_{DIF(up,down)} + T^{OFFSET}_{0} + T_{SLEWING})$$

8.4. Normalization of Track Matching Residuals (z and ϕ)

Positioning of the "hit" of an incident particle is determined both internally, using the known geometric layout of the detector, and externally, by projection onto the TOFW by the PHENIX track reconstruction algorithms. The difference in these two measurements are referred to as "track matching residuals." The un-normalized TOFW residuals are shown in Fig. 8.5a, for z, and Fig. 8.1 for ϕ. Normalization is preformed by fitting these raw distributions with two gaussians, for background and signal (the native track matching residual), as demonstrated in Fig. 8.5b. The width of σ_{dZ} is shown to be 1.9 *cm*, which is, as expected, from the 2.8 *cm* width of the MRPC signal readout strips, which constrains the positioning resolution of the detector in z. The extracted width of $\sigma_{d\phi}$ is shown to be 4.9 *mrad*, which corresponds to an azimuthal resolution (local Y direction) of 2.*3 cm.*

The normalization procedure is implemented by momentum, charge, and centrality class, for which, as a result, normalized track matching cuts may be used uniformly. For normalization, the residual means are set to zero and normalized to 1-sigma, as extracted from the raw residual distributions (Fig. 8.1 and Fig. 8.5a). At the data analysis level, track matching cuts are useful for background rejection. These matching cuts improve signal to background levels. They are often referred to by the width of their cuts on the normalized residuals, such as "one sigma" or

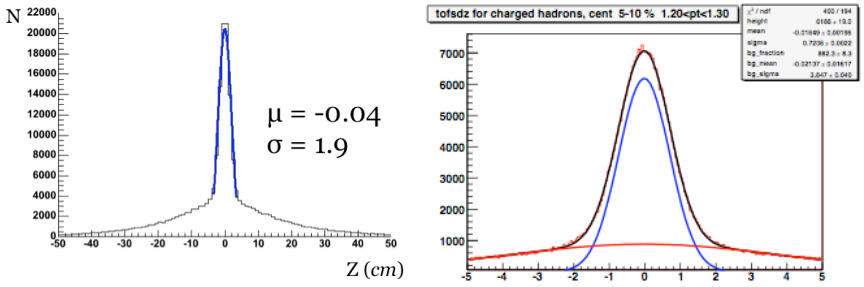

(A) Distribution (B) Normalization

FIGURE 8.5. TOFW Track Matching Residual in Z (beam axis)

"two sigma." Track matching normalization is a high-level calibration and is implemented in the MatchrecalRecoRun7 class of the master recalibrator.

APPENDIX A

Photos from the TOFW Installation

FIGURE A.1. TOFW Sector Installation (PHENIX IR)

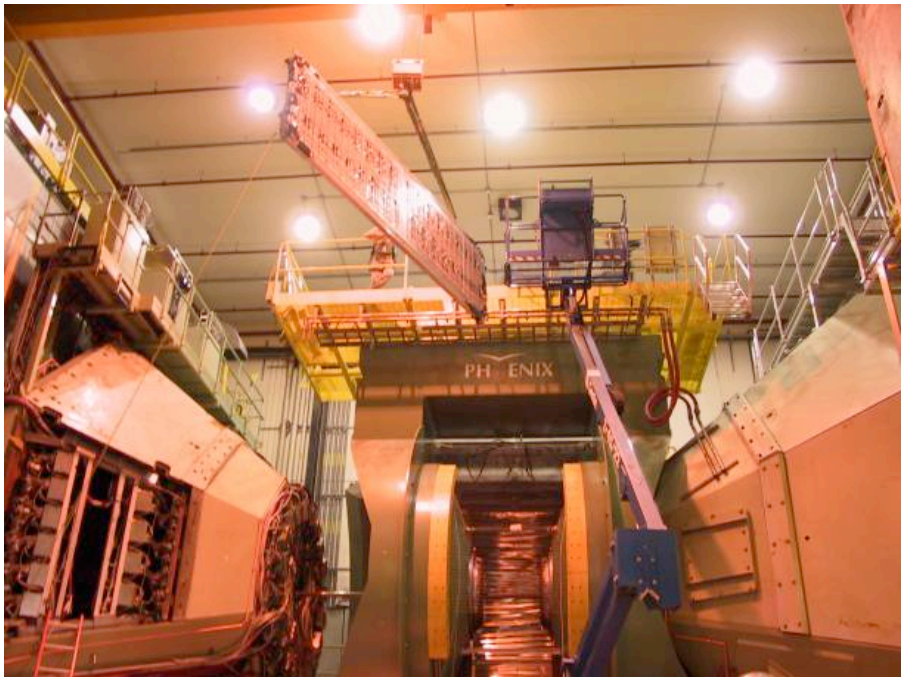

FIGURE A.2. MRPC Production (Clean Room, 9th floor, Stevenson 6000, Vanderbilt University, Nashville, TN, USA)

FIGURE A.3. At BNL, Transportation from the Hi-Bay assembly area (Physics, bldg) to the PHENIX IR

FIGURE A.4. Backside of the Central Arm East (PHENIX IR)

FIGURE A.5. Top of Central Arm West, in the process of installing one TOFW sector

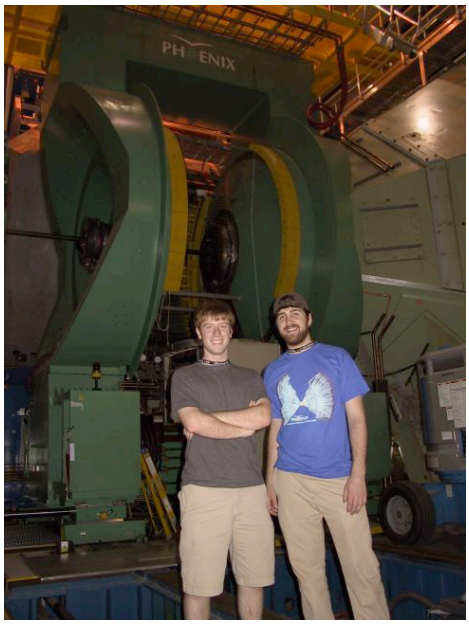

(A) Dillon Roach (Grad Student, VU) Evan Leitner (Senior Undergrad, VU) June 2006

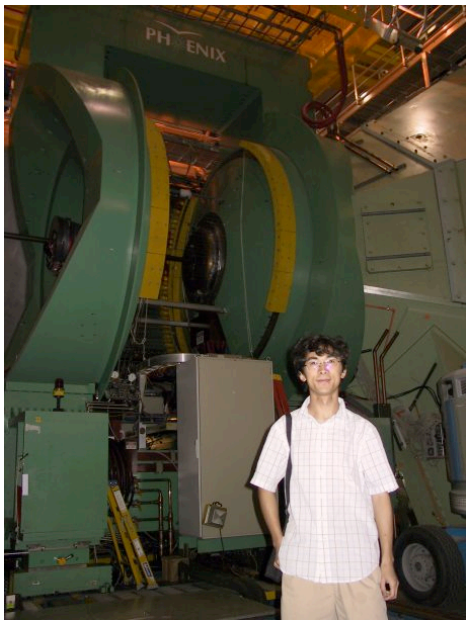

(B) Shengli Huang (Post-Doc, VU) June 2006

(C) Brian Love, PHENIX Counting House, March 2009

FIGURE A.6. PHENIX IR and Counting House

APPENDIX B

Global Geometric Parameters and Layout

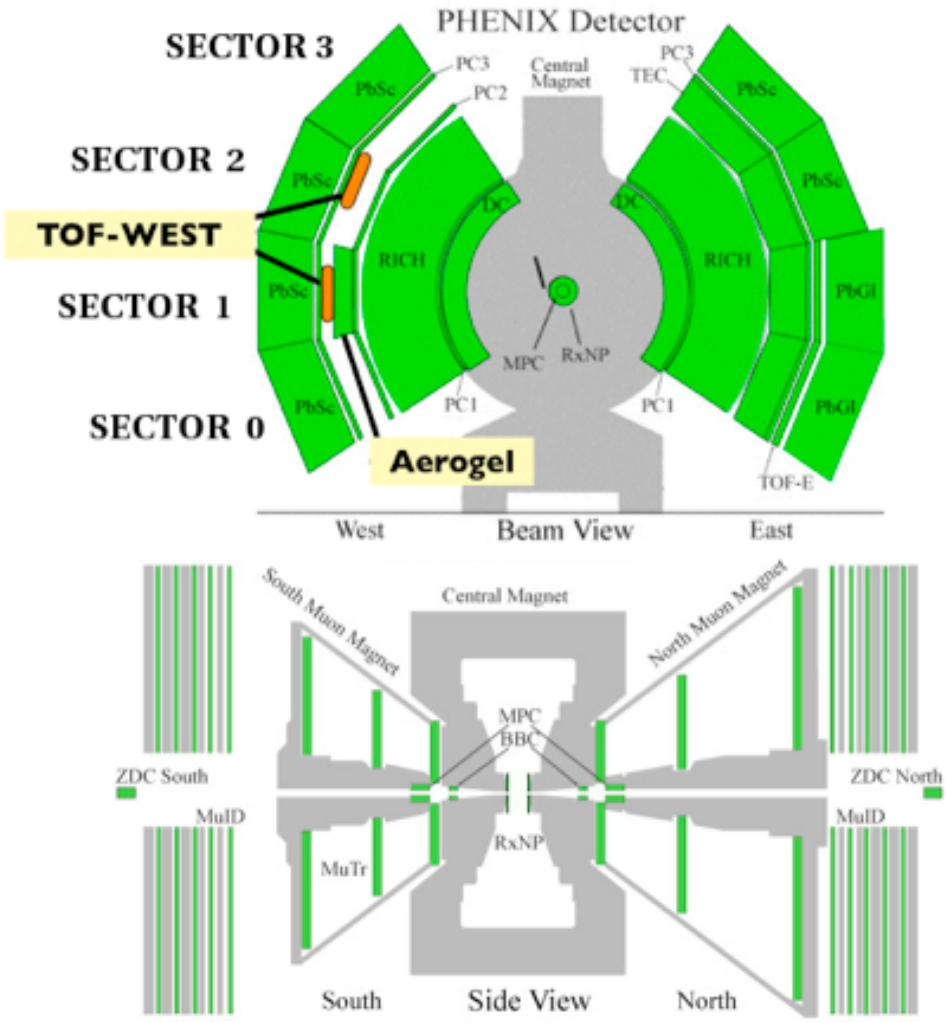

FIGURE B.1. PHENIX Spectrometer

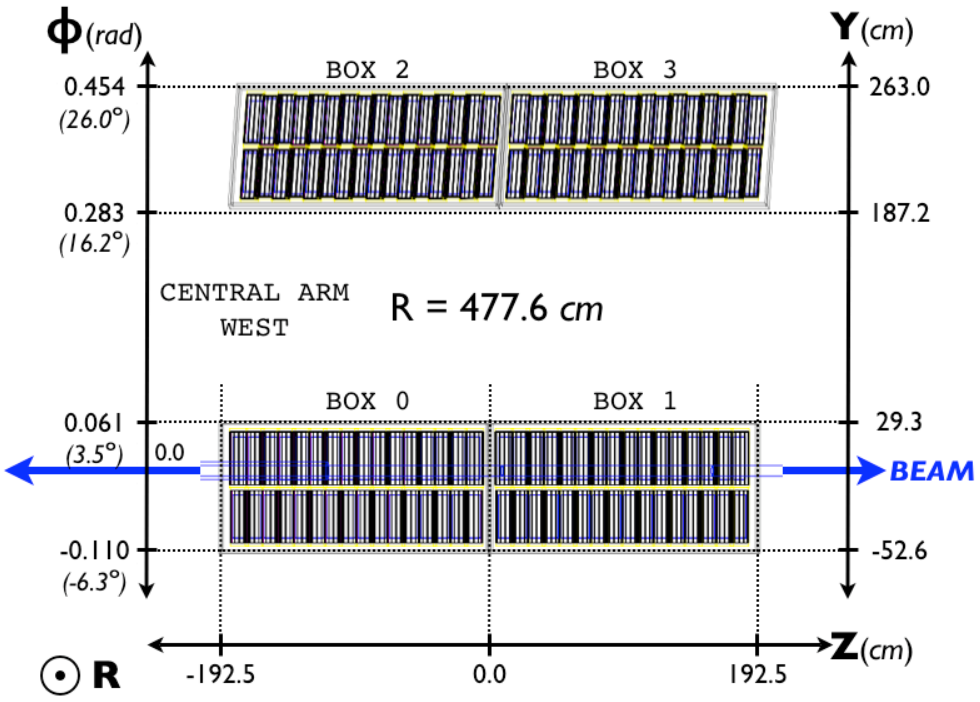

FIGURE B.2. TOFW Geometry (Longitudinal View)

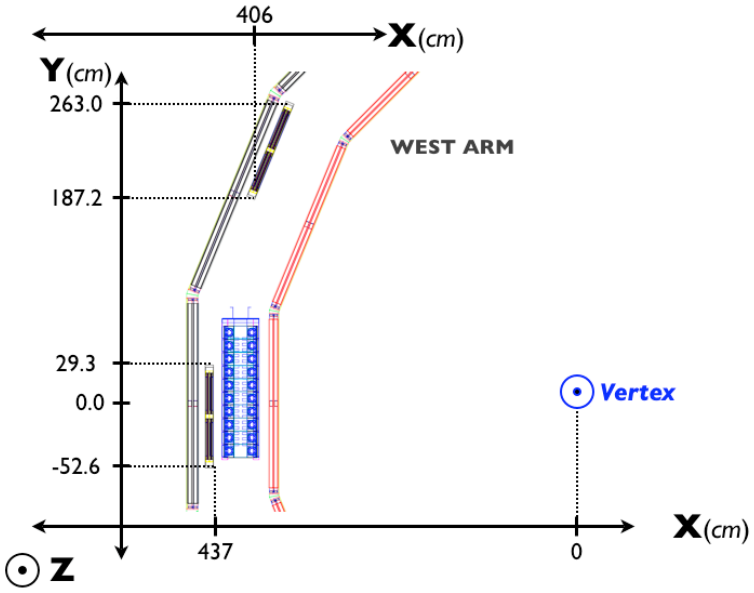

FIGURE B.3. TOFW Geometry (Transverse View)

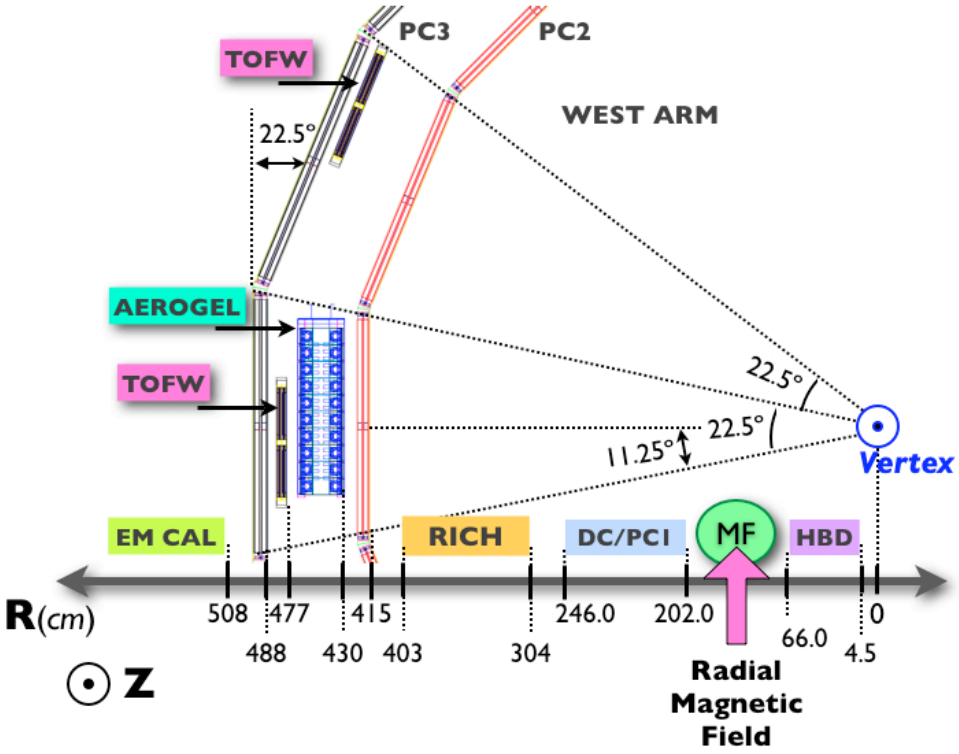

FIGURE B.4. Central Arm West (Cross Section)

APPENDIX C

Detector Response (*from Cosmic Ray Test Bench*)

Detector signals were extracted from one MRPC chamber in a laboratory cosmic ray test bench. Events were triggered using a double co-incidence between two PMT scintillators, above and below the detector. The MRPC signals were preamplified and delayed in order to allow time for event triggering and subsequent signal processing. The same FEEs were used in the lab as are in-situ, which in addition to signal extraction and amplification, induces some signal shaping on the trailing end. The ringing effect, for example, is an artifact of the electronics. TDC signals were generated from leading-edge discrimination of the analog signal, as is done in-situ using the TOFW FEMs. In the lab, we used NIM modules for such signal processing, and the discriminator level was set to the device minimum of 15mV. Lab view was used for data acquisition. These scope picture were acquired from a Tectronic oscilloscope.

The gas mixture used when extracting these signals was 90% Freon, 2.5% Isobutane, and 2.5% SF6. To note, for reference, the sensitivity of our gas flow meter limited our ability to lower the SF6 concentrations below 1%.

All four of the MRPC strips were read out simultaneously. Each "A1" corresponds to the ADC value from one end of the MRPC strip. "T1" and "T2" correspond to TDC values from opposite ends of the MRPC strip. "T1" and "A1" correspond to the same strip end. TDC values of 4095 correspond to an event overflow.

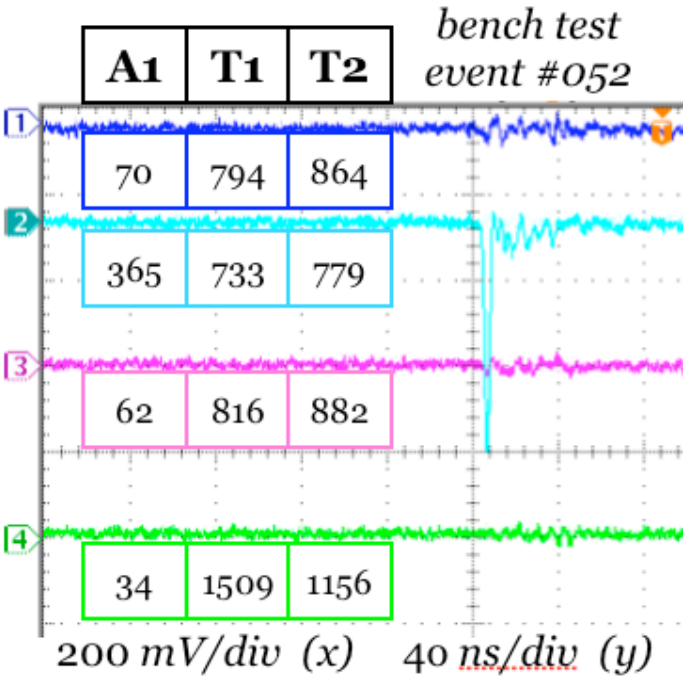

FIGURE C.1. Single Strip Event (typical)

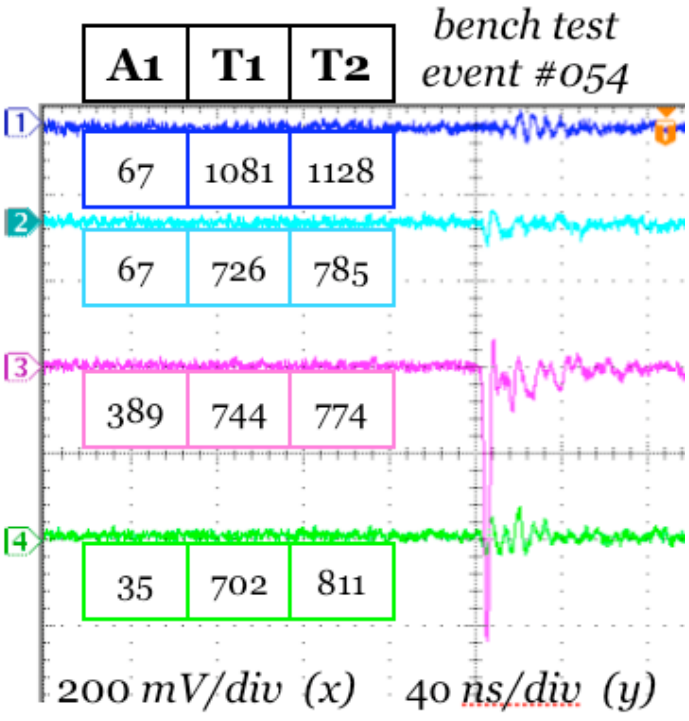

FIGURE C.2. Single Strip Event (typical)

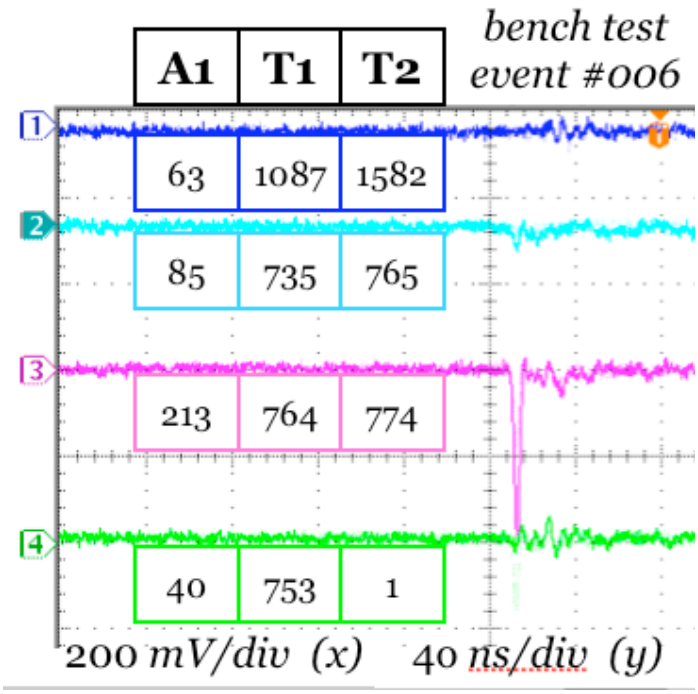

FIGURE C.3. Single Strip Event with Small Secondary in Neighboring Strip

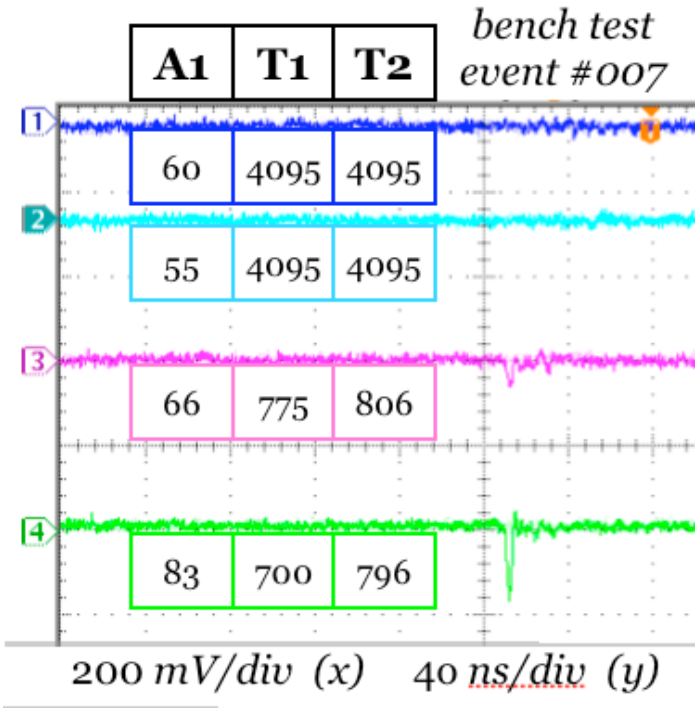

FIGURE C.4. Double Strip Event

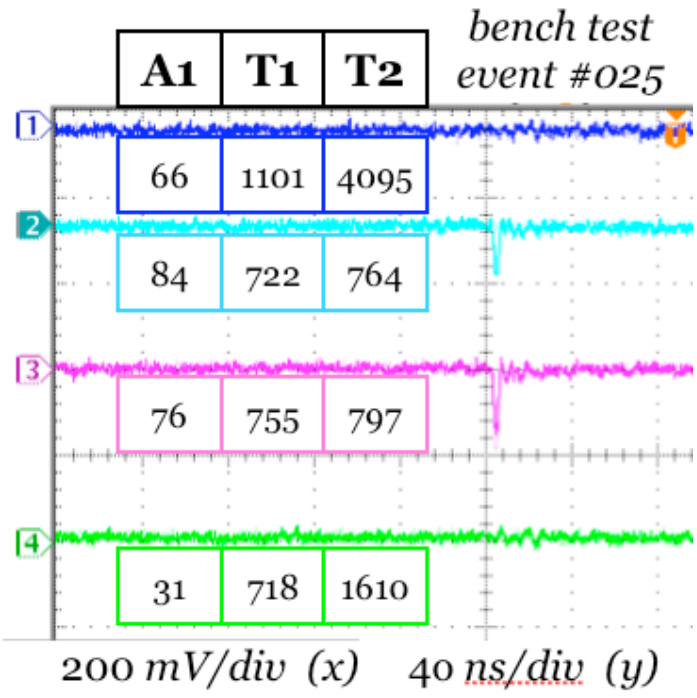

FIGURE C.5. Double Strip Event

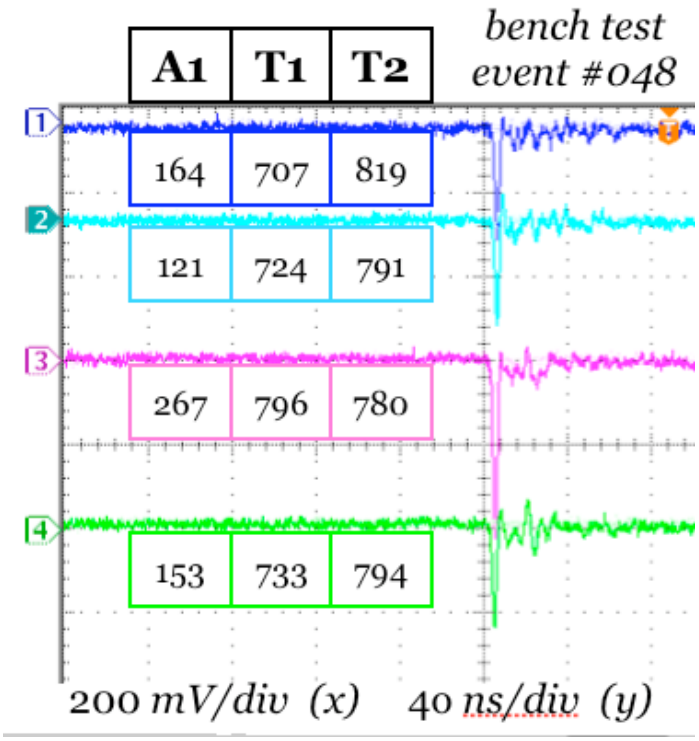

FIGURE C.6. Multiple Strip Event (rare)

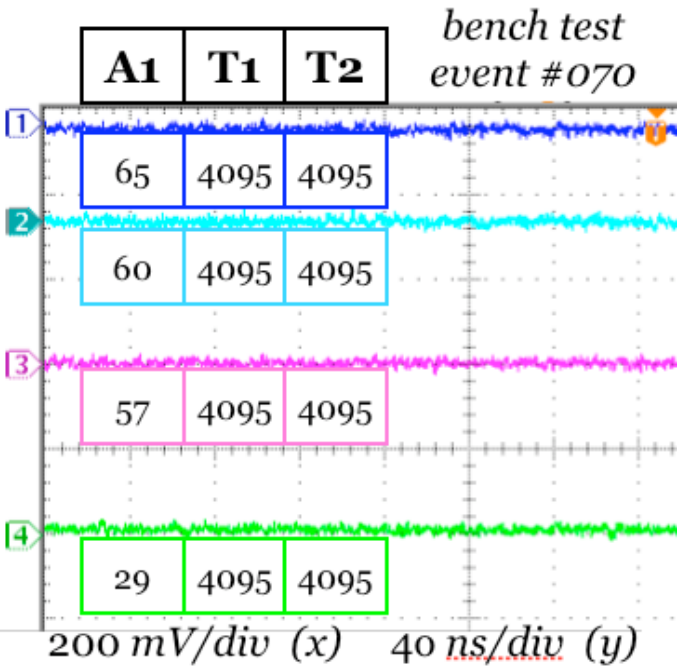

FIGURE C.7. Empty Event (baseline)

APPENDIX D

PHENIX Data Acquisition

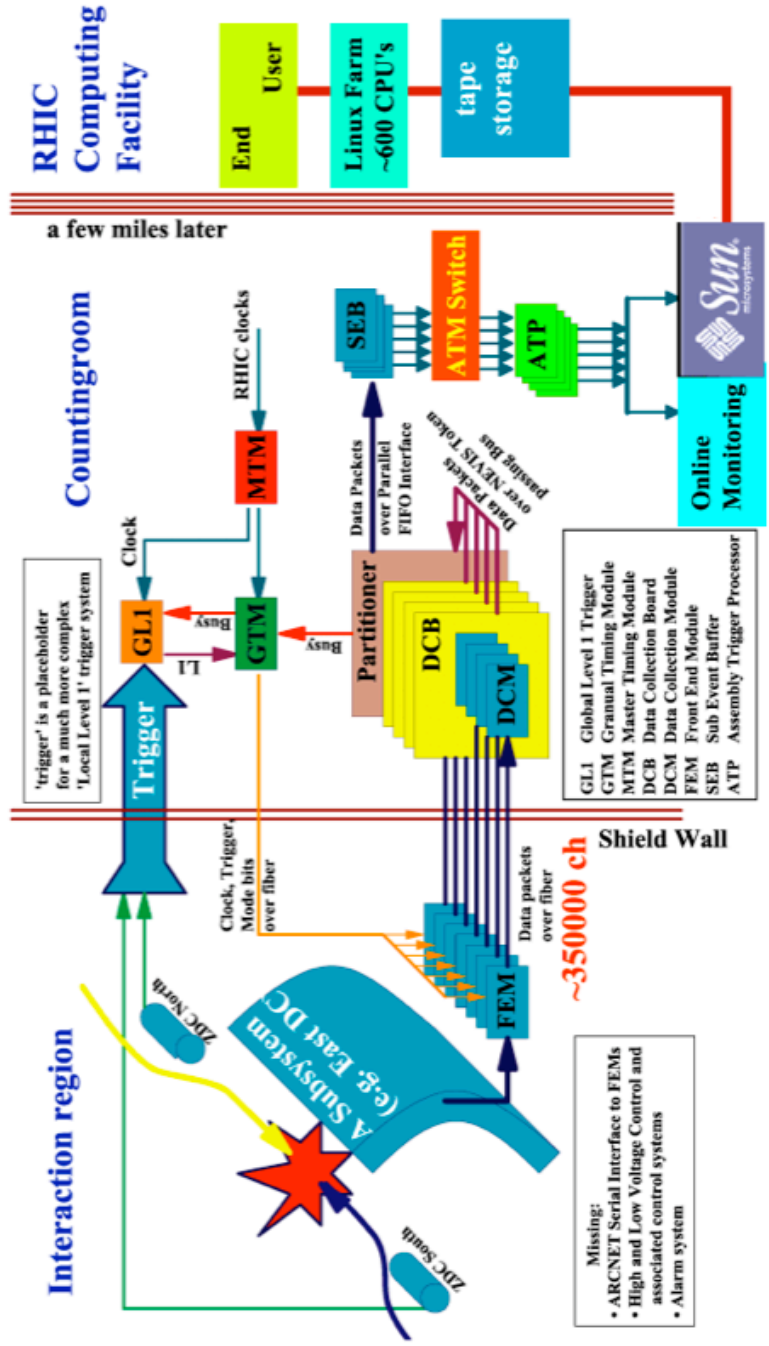

FIGURE D.1. PHENIX DAQ

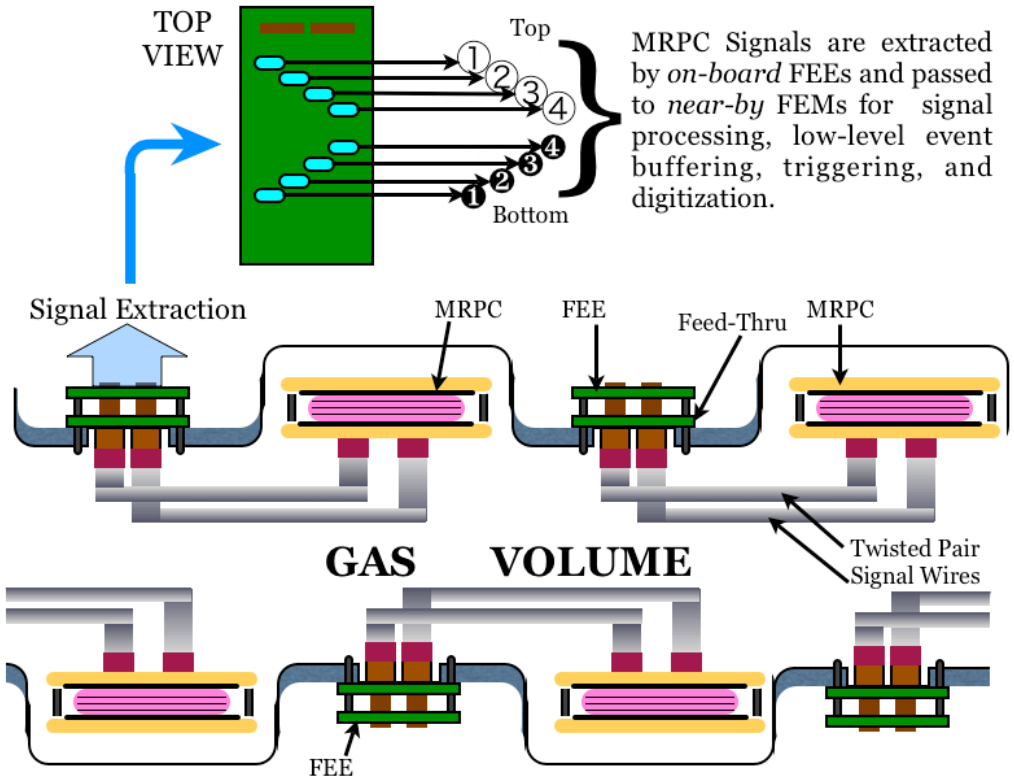

(A) Side View

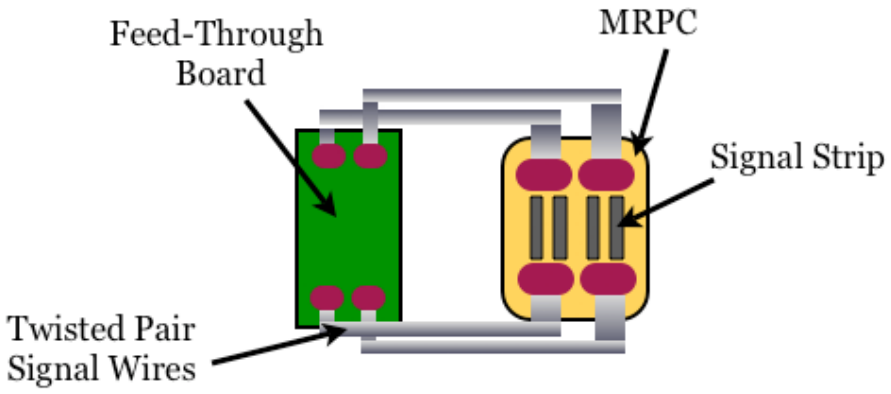

(B) Top View *(from iside the gas chamber)*

FIGURE D.2. FEE Layout (Inside the Gas Box)

APPENDIX E

TOFW Online Monitoring

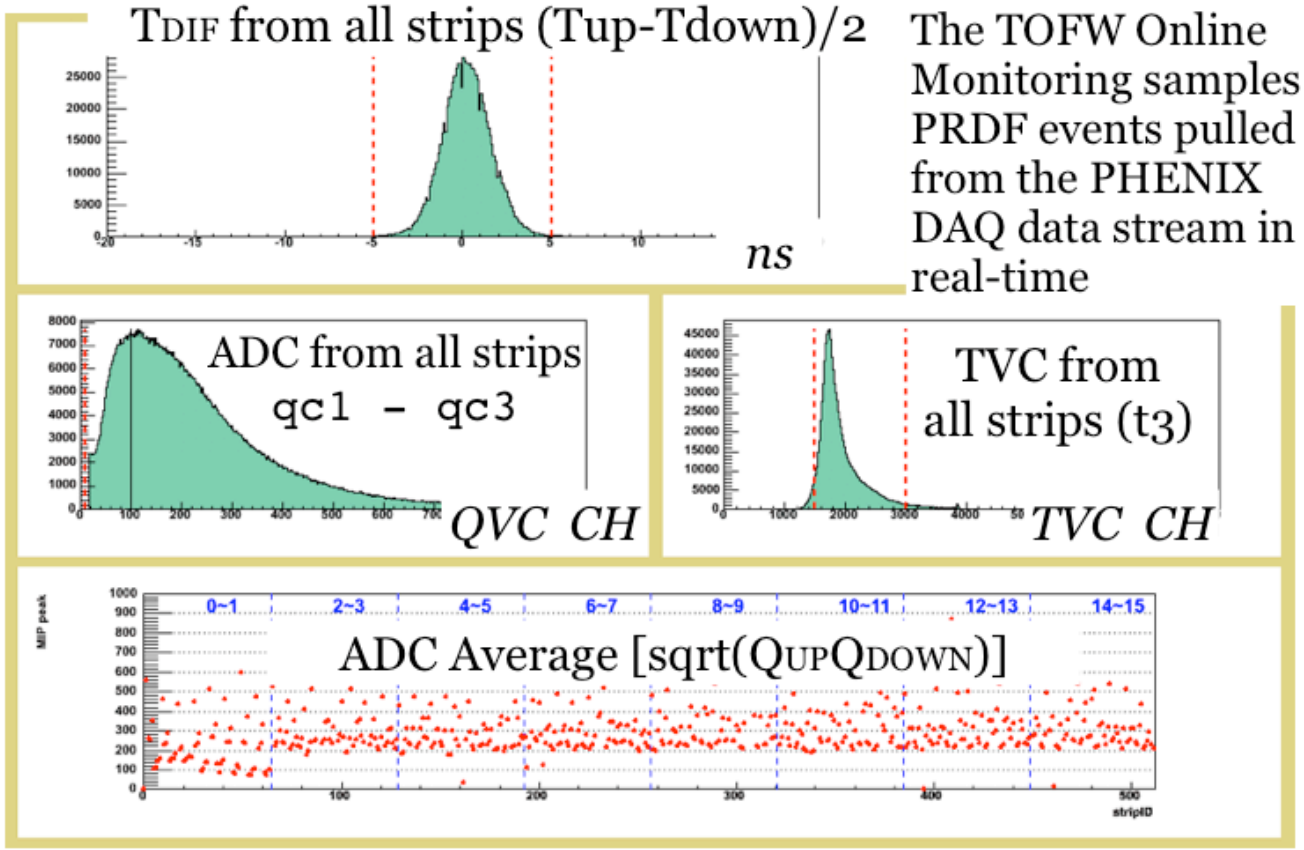

Figure E.1. Online Monitoring Display

APPENDIX F

Geometric Enumeration of ID Numbers

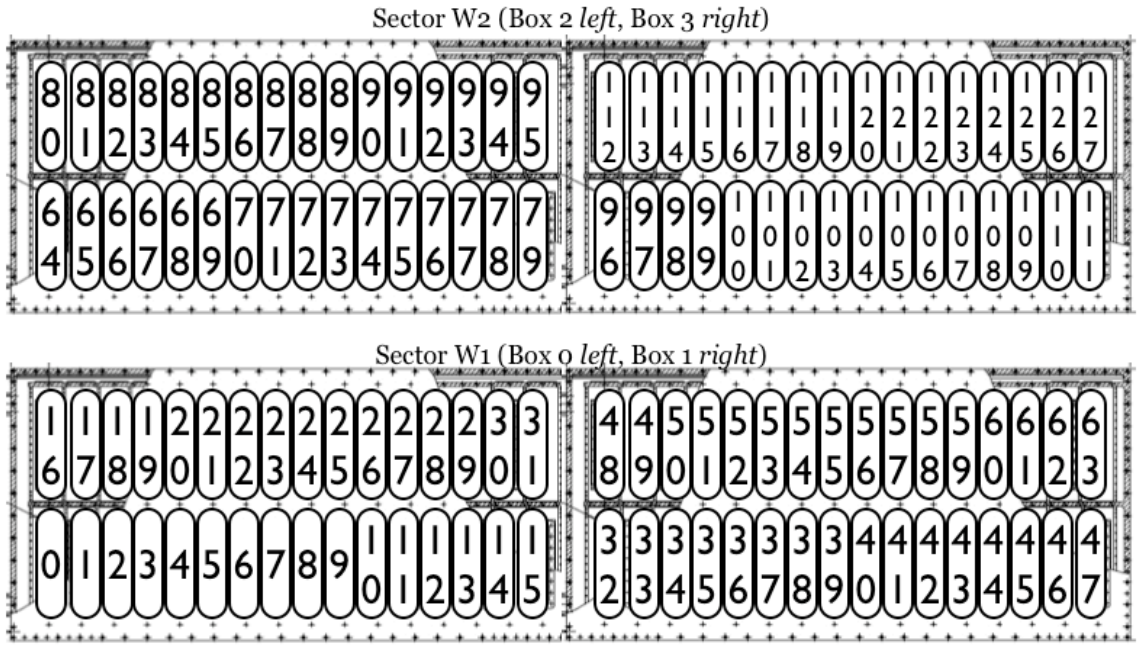

(A) MRPC ID

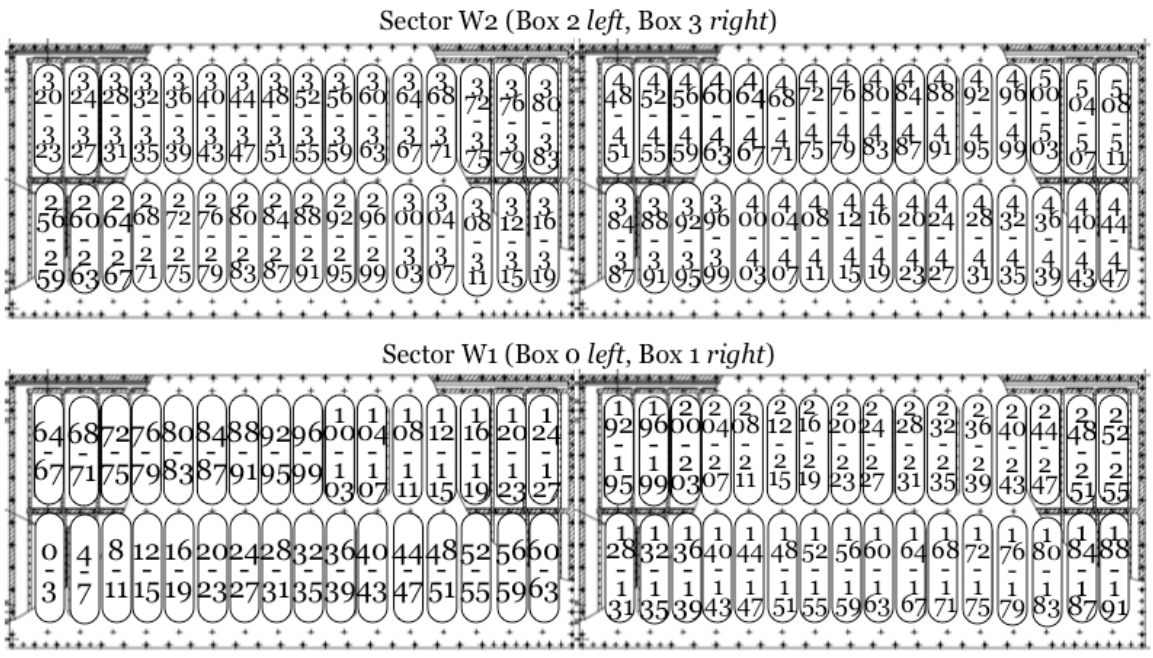

(B) Strip ID

FIGURE F.1. Geometric Enumeration of ID Numbers

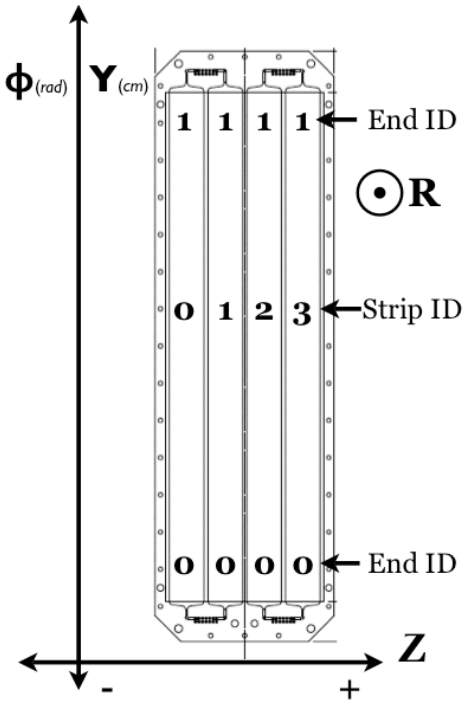

FIGURE F.2. Strip End ID

APPENDIX G

Data Structure of the TOFW Packet

TABLE G.1. Data Structure of TOFW Packet

Data members in each channel include "Q1","Q3", "T3", "T4"
TOFW data stored in PRDF packets 7101, 7102, 7103, and 7104

TOFW PacketID = 7101			
CRATE 0			
MrpcID	SlatID	EndID	iCh
0	0	0	0
		1	1
	1	0	2
		1	3
	2	0	4
		1	5
	3	0	6
		1	7
1	4	0	8
		1	9
	5	0	10
		1	11
	6	0	12
		1	13
	7	0	14
		1	15
2	8	0	16
		1	17
	9	0	18
		1	19
	10	0	20
		1	21
	11	0	22
		1	23
...			
31	124	0	248
		1	249
	125	0	250
		1	251
	126	0	252
		1	253
	127	0	254
		1	255

TOFW PacketID = 7102			
CRATE 1			
MrpcID	SlatID	EndID	iCh
32	128	0	0
		1	1
	129	0	2
		1	3
	130	0	4
		1	5
	131	0	6
		1	7
33	132	0	8
		1	9
	133	0	10
		1	11
	134	0	12
		1	13
	135	0	14
		1	15
...			
63	252	0	248
		1	249
	253	0	250
		1	251
	254	0	252
		1	253
	255	0	254
		1	255

TOFW PacketID = 7103			
CRATE 2			
MrpcID	SlatID	EndID	iCh
64	256	0	0
		1	1
	257	0	2
		1	3
	258	0	4
		1	5
	259	0	6
		1	7
65	260	0	8
		1	9
	261	0	10
		1	11
	262	0	12
		1	13
	263	0	14
		1	15
...			
95	380	0	248
		1	249
	381	0	250
		1	251
	382	0	252
		1	253
	383	0	254
		1	255

TOFW PacketID = 7104			
CRATE 3			
MrpcID	SlatID	EndID	iCh
96	384	0	0
		1	1
	385	0	2
		1	3
	386	0	4
		1	5
	387	0	6
		1	7
97	388	0	8
		1	9
	389	0	10
		1	11
	390	0	12
		1	13
	391	0	14
		1	15
...			
127	508	0	248
		1	249
	509	0	250
		1	251
	510	0	252
		1	253
	511	0	254
		1	255

APPENDIX H

Additional Drawings of the MRPC Detector

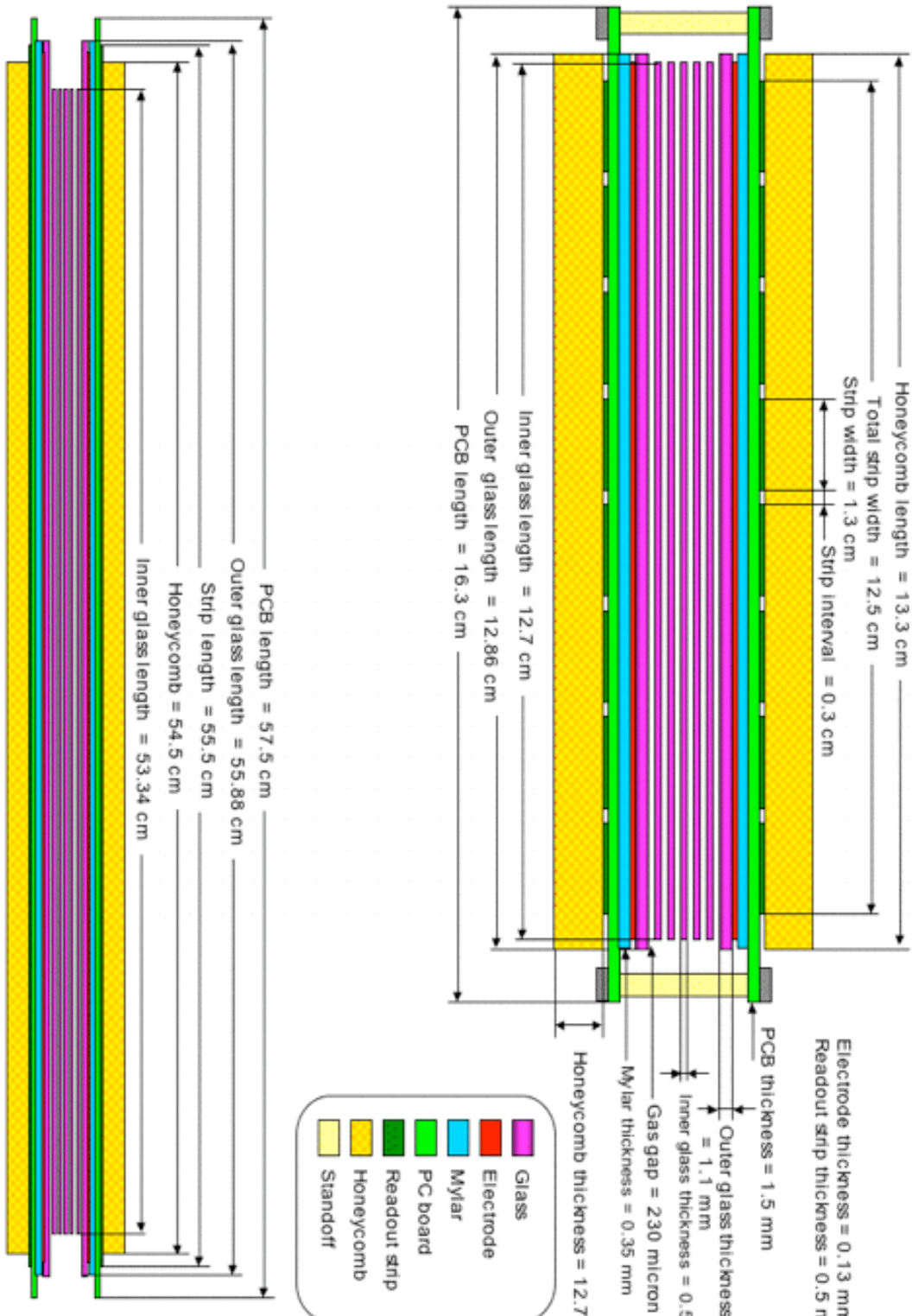

FIGURE H.1. Material Composition of the MRPC

NOTES:

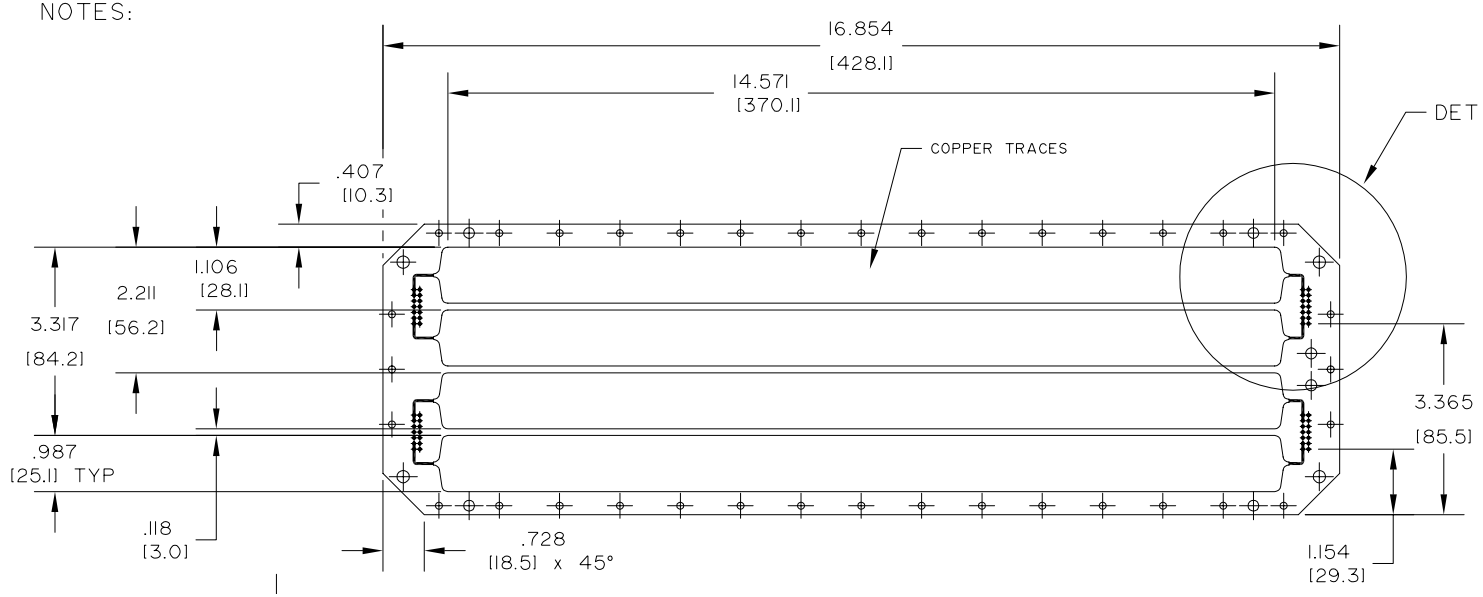
16.854
[428.1]
14.571
[370.1]
DET
COPPER TRACES
.407
[10.3]
1.106
[28.1]
2.211
[56.2]
3.317
[84.2]
.987
[25.1] TYP
.118
[3.0]
.728
[18.5] x 45°
3.365
[85.5]
1.154
[29.3]

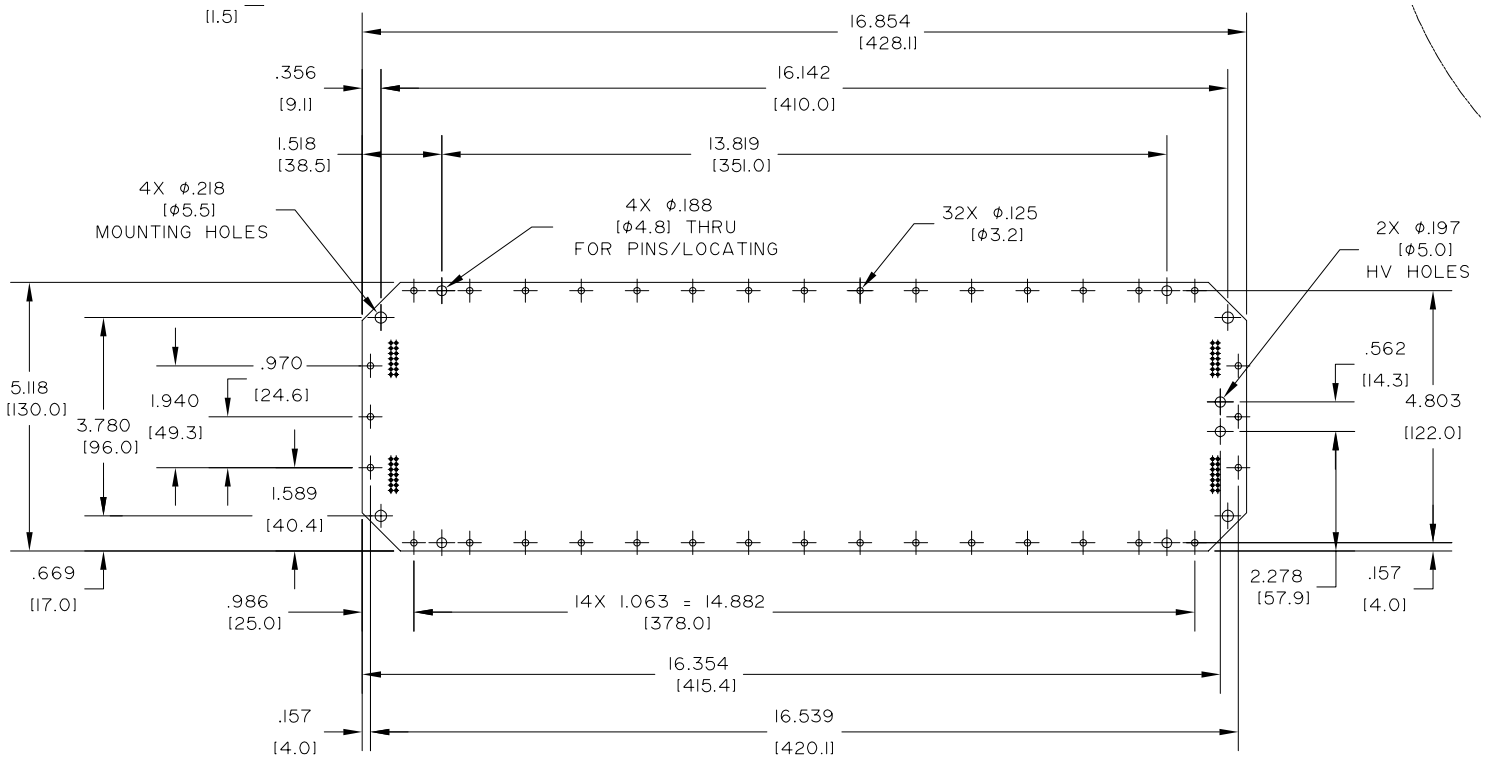
[1.5]
16.854
[428.1]
.356
[9.1]
16.142
[410.0]
1.518
[38.5]
13.819
[351.0]
4X Φ.218
[Φ5.5]
MOUNTING HOLES
4X Φ.188
[Φ4.8] THRU
FOR PINS/LOCATING
32X Φ.125
[Φ3.2]
2X Φ.197
[Φ5.0]
HV HOLES
.970
[24.6]
1.940
[49.3]
1.589
[40.4]
5.118
[130.0]
3.780
[96.0]
.562
[14.3]
4.803
[122.0]
.669
[17.0]
.986
[25.0]
14X 1.063 = 14.882
[378.0]
2.278
[57.9]
.157
[4.0]
16.354
[415.4]
.157
[4.0]
16.539
[420.1]

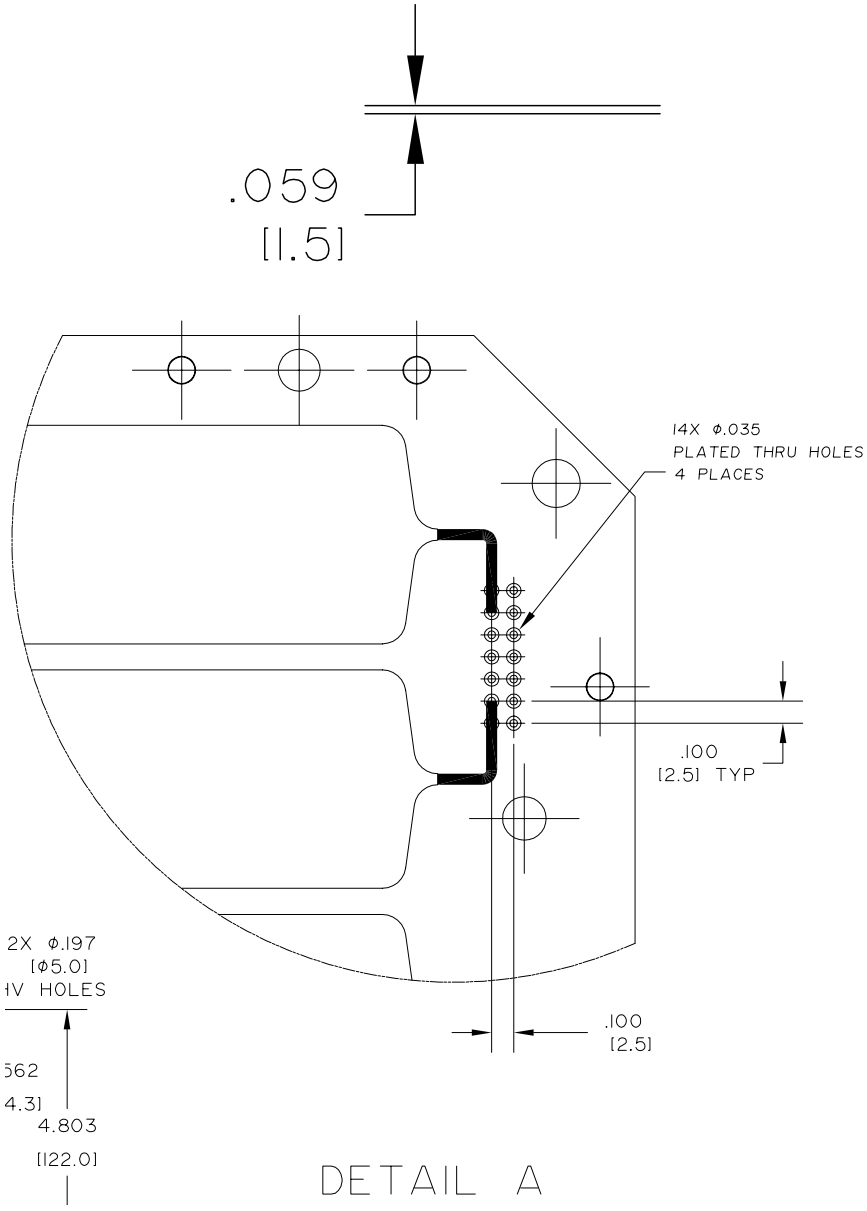
.059
[1.5]
14X ϕ.035
PLATED THRU HOLES
4 PLACES
.100
[2.5] TYP
.100
[2.5]
2X ϕ.197
[ϕ5.0]
4V HOLES
562
4.3]
4.803
[122.0]

DETAIL A

APPENDIX I

Schematic Drawings

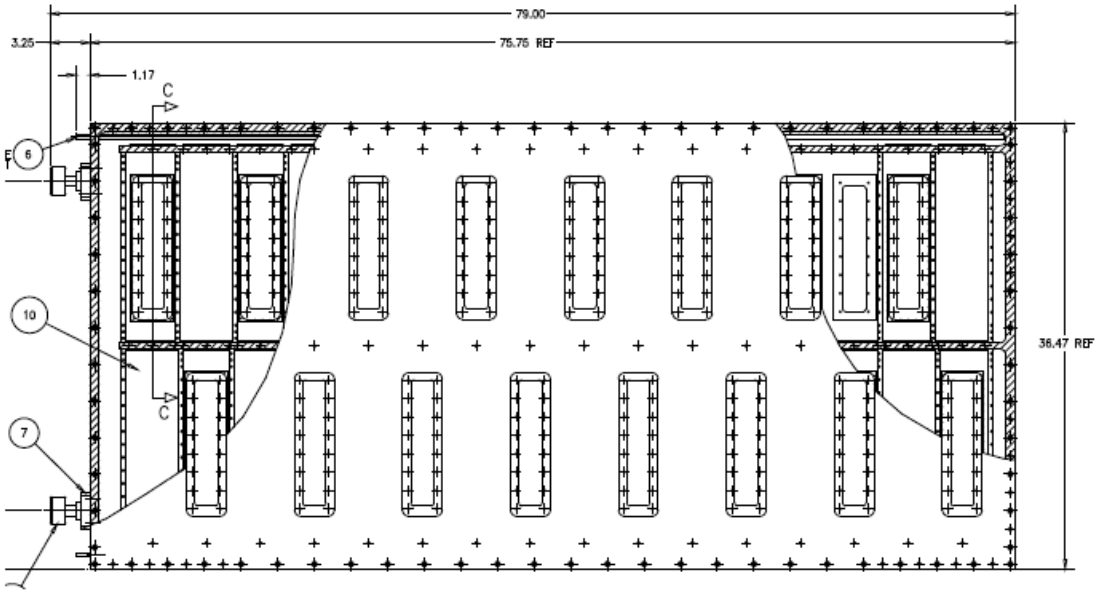

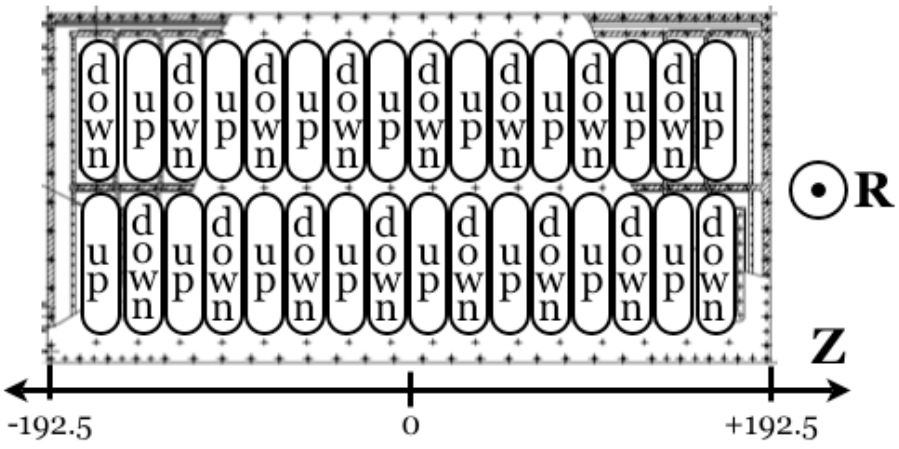

FIGURE I.1. Radial Juxtaposition of MRPC Detectors in each Gas Box
$\Delta R_{plane} = R_{up} - R_{down} = 3.5cm$

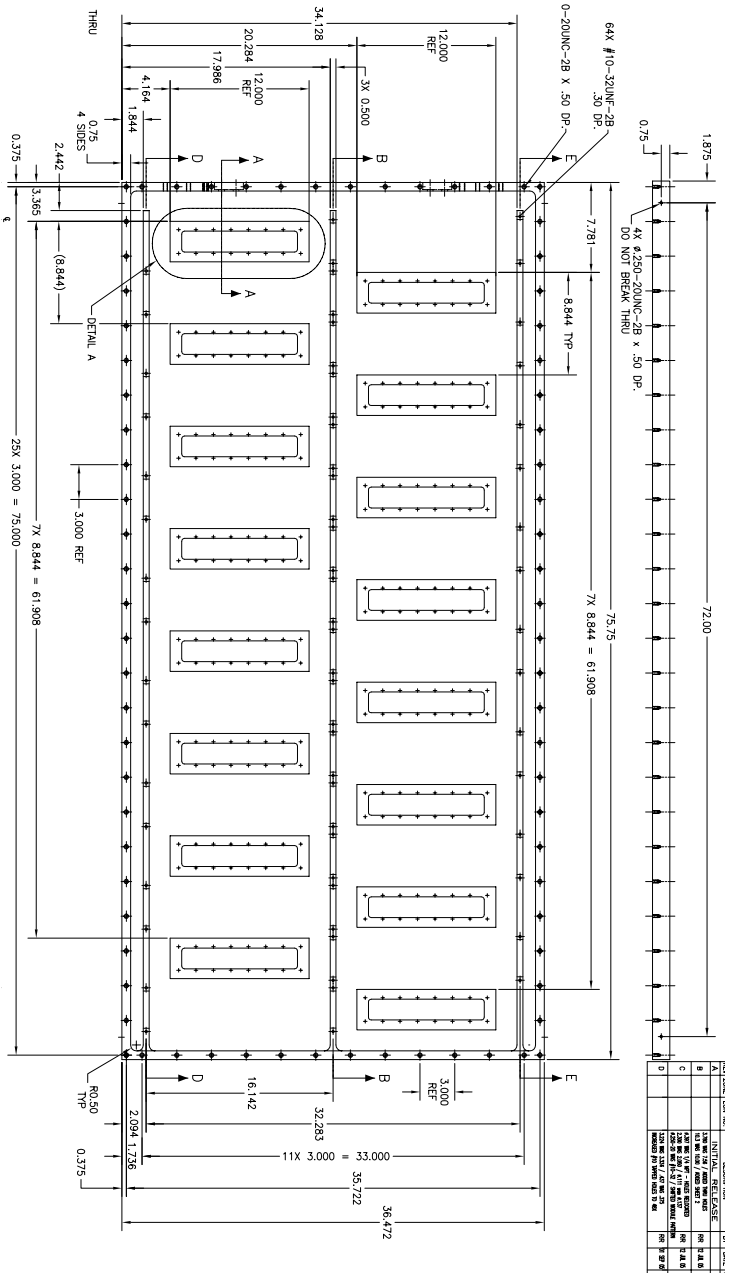

FIGURE I.2. Schematic of the Gas Chamber

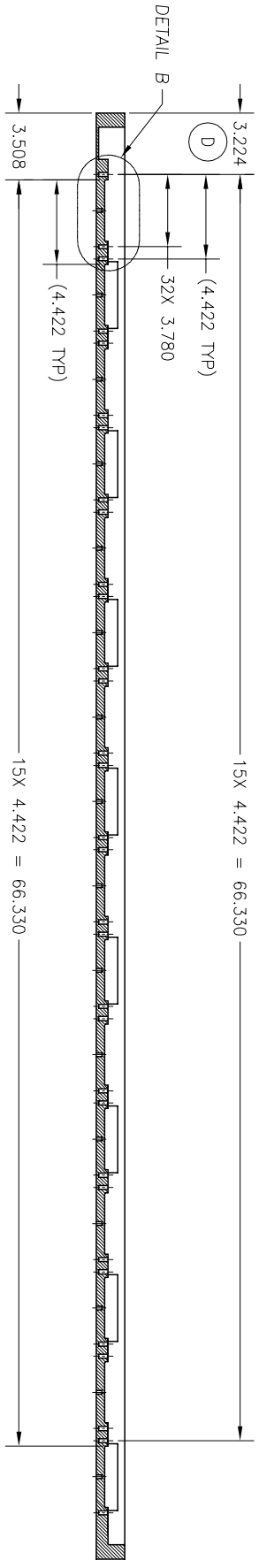
DETAIL B
D
3.508
3.224
(4.422 TYP)
32X 3.780
(4.422 TYP)
15X 4.422 = 66.330
15X 4.422 = 66.330

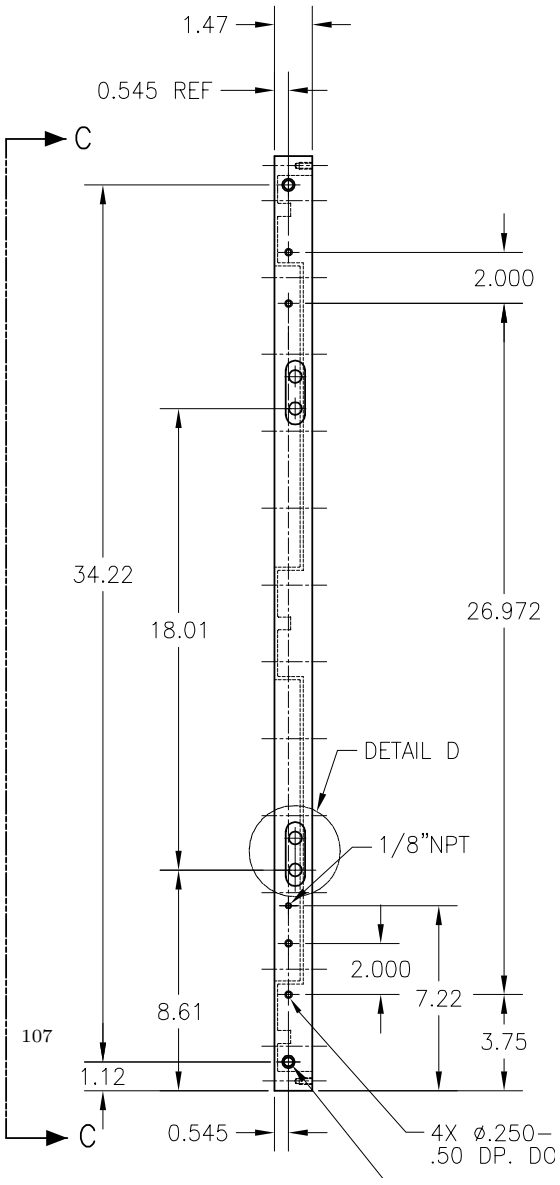
1.47
0.545 REF
C
2.000
34.22
18.01
26.972
DETAIL D
1/8"NPT
2.000
7.22
8.61
3.75
1.12
C
0.545
4X ø.250–
.50 DP. DC

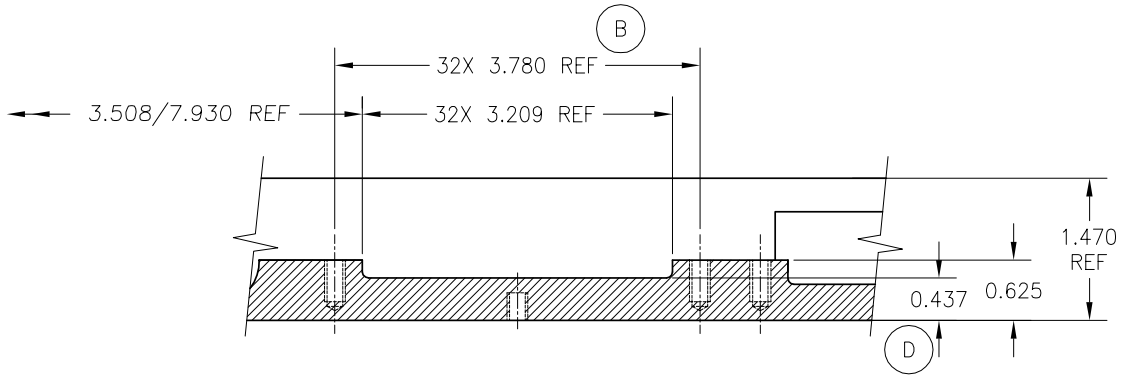

DETAIL B

SCALE 4.000

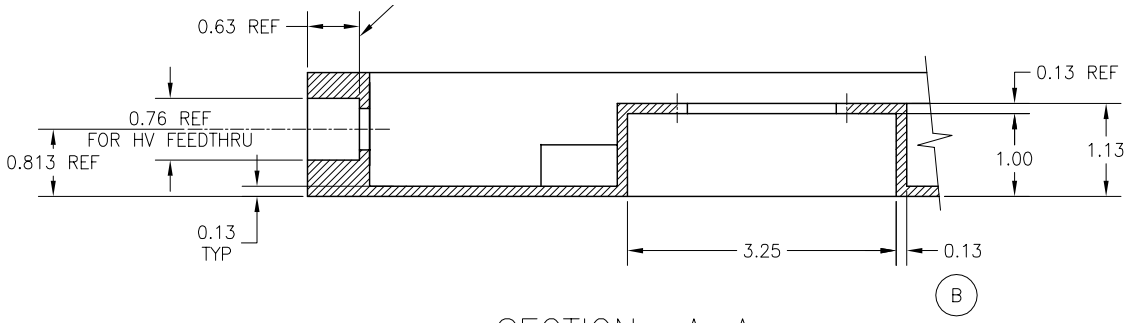

SECTION A–A

SCALE 4.000

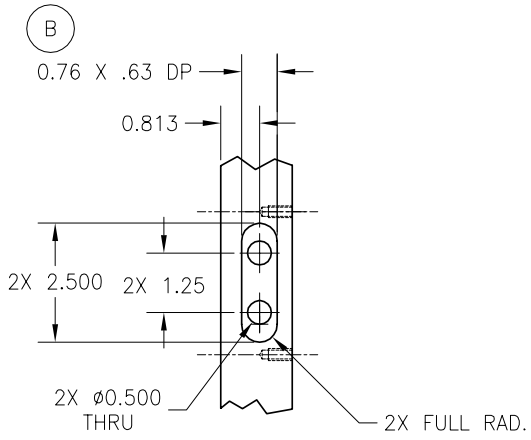

DETAIL D

SCALE 2.000

2 PLACES

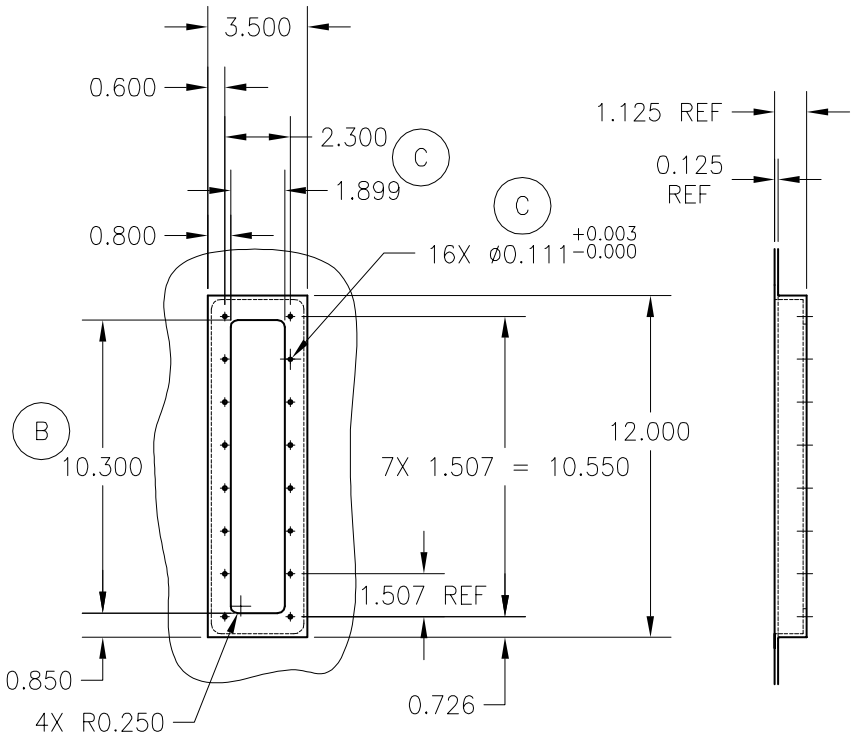

DETAIL A
SCALE 1.000
16 PLACES

These views not to scale:

F/T Board, Bottom Side

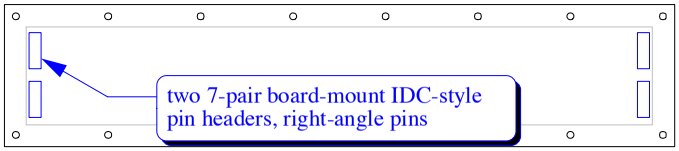

F/T Board, Top Side

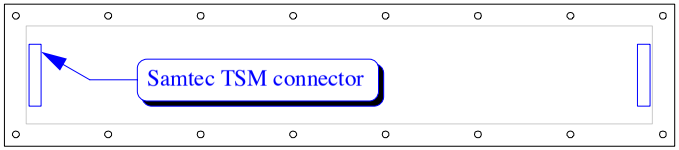

FEE Board, Top Side

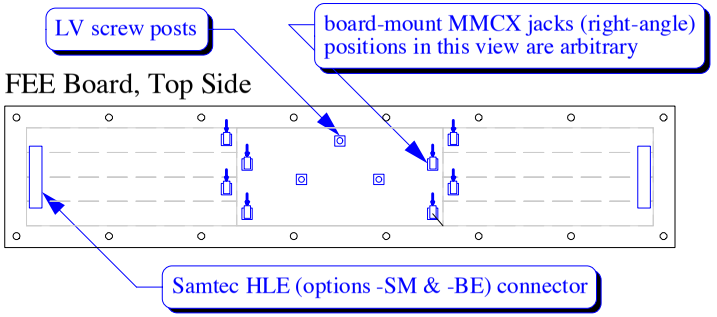

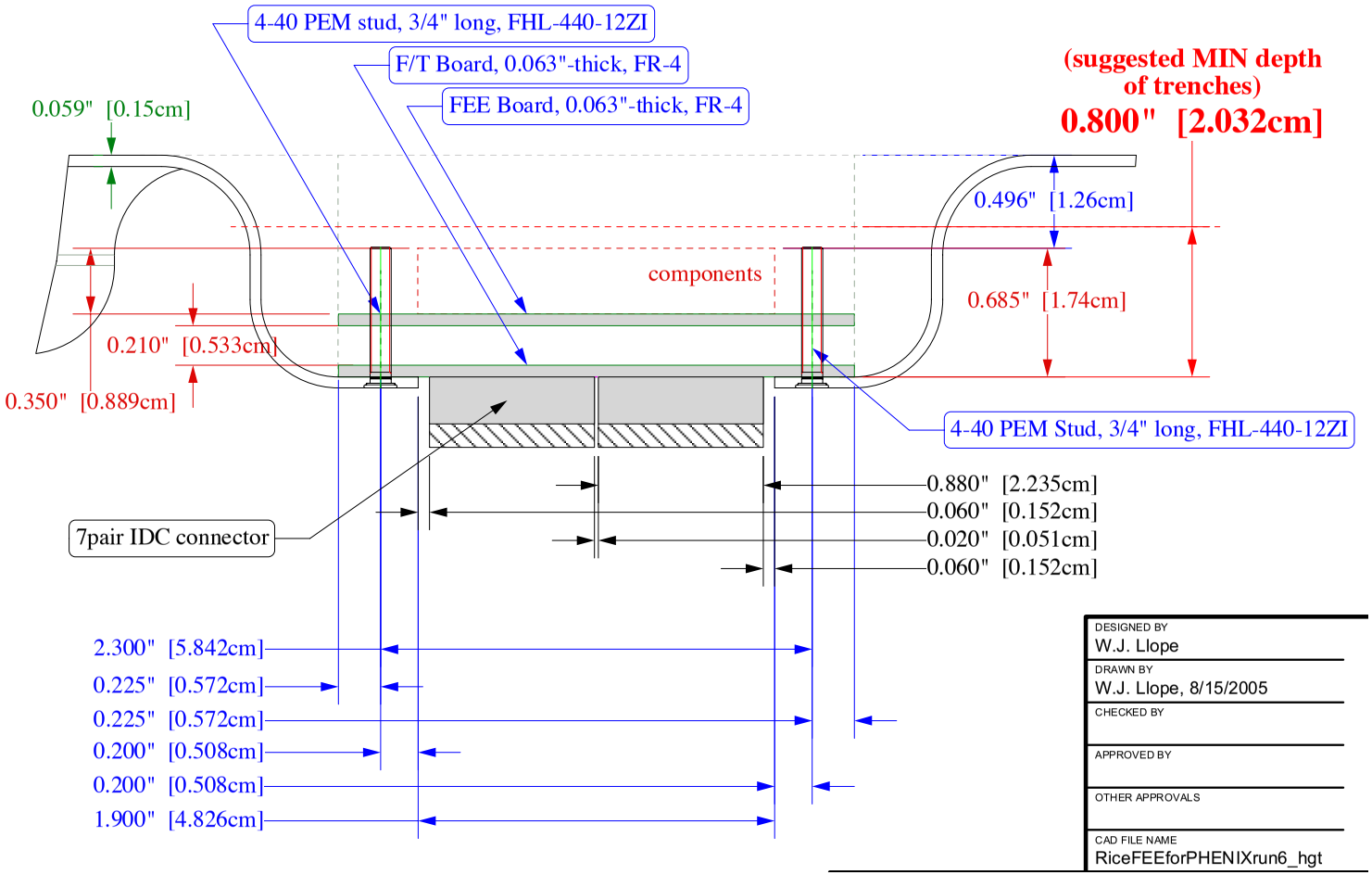
4-40 PEM stud, 3/4" long, FHL-440-12ZI
F/T Board, 0.063"-thick, FR-4
FEE Board, 0.063"-thick, FR-4
(suggested MIN depth of trenches)
0.800" [2.032cm]
0.059" [0.15cm]
0.496" [1.26cm]
components
0.685" [1.74cm]
0.210" [0.533cm]
0.350" [0.889cm]
4-40 PEM Stud, 3/4" long, FHL-440-12ZI
7pair IDC connector
0.880" [2.235cm]
0.060" [0.152cm]
0.020" [0.051cm]
0.060" [0.152cm]
2.300" [5.842cm]
0.225" [0.572cm]
0.225" [0.572cm]
0.200" [0.508cm]
0.200" [0.508cm]
1.900" [4.826cm]
DESIGNED BY
W.J. Llope
DRAWN BY
W.J. Llope, 8/15/2005
CHECKED BY
APPROVED BY
OTHER APPROVALS
CAD FILE NAME
RiceFEEforPHENIXrun6_hgt

TOF.W Preamp Low Voltage Supply Cabling
(1/8 shown)

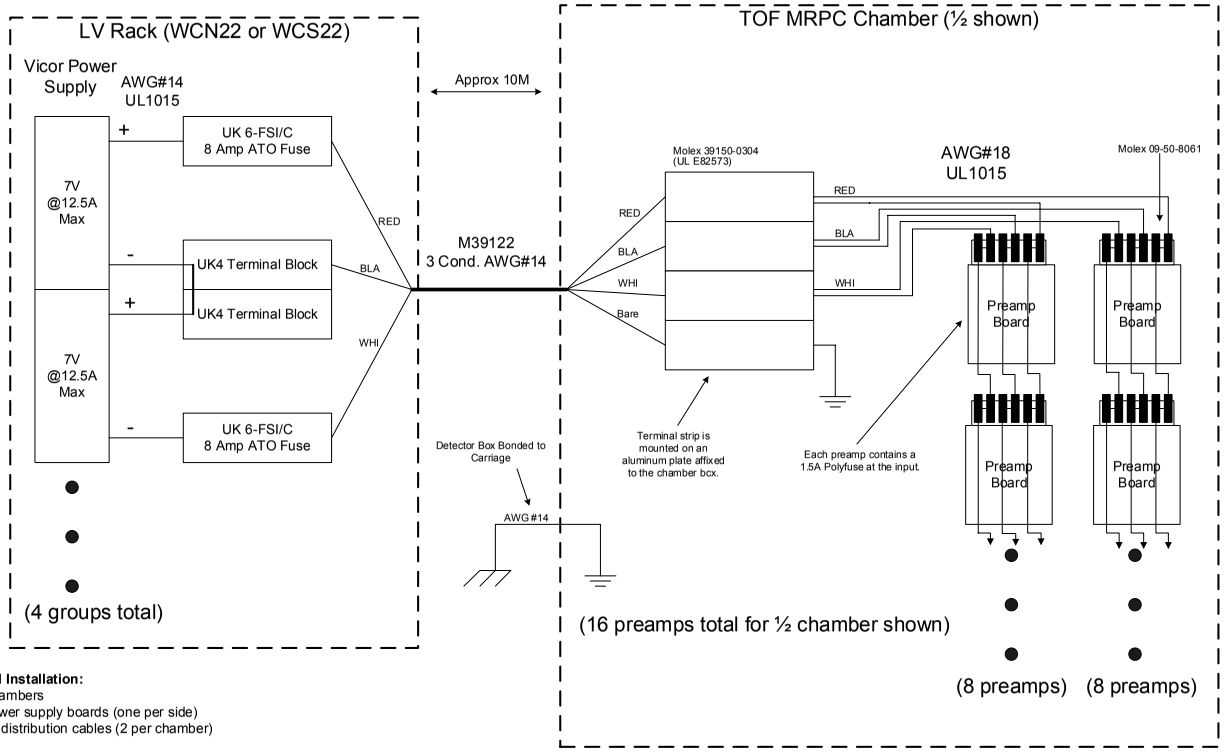

Total Installation:
4 Chambers
2 Power supply boards (one per side)
8 LV distribution cables (2 per chamber)

REFERENCES

[1] K. Adcox *et al*., Nucl. Phys. A **757**, 184 (2005).

[2] I. Arsene *et al*., Nucl. Phys. A **757**, 1 (2005).

[3] B. Back *et al*., Nucl. Phys. A **757**, 28 (2005).

[4] J. Adams *et al*., Nucl. Phys. A **757**, 102 (2005).

[5] W. J. Llope, Nucl. Instrum. Meth. B **241**, 306 (2005).

[6] A. Rose, J. Phys. G34, S **715** (2007).

[7] X. Dong, AIP Conf. Proc. **865**, 332 (2006).

[8] W. J. Llope *et al*., Nucl. Instrum. Meth. A **522**, 252 (2004).

[9] W. Llope *et al*., Nucl. Instrum. Meth. A **593**, 307 (2008).

[10] A. Akindinov *et al*., Eur. Phys. J. C **32S1**, 165 (2004).

[11] S. Belikov, J. Hill, J. Lajoie, H. Skank, and G. Sleege, Nucl. Instrum. Meth. A **494**, 541 (2002).

[12] L. Aphecetche *et al*., Nucl. Instrum. Meth. A **499**, 521 (2003).

[13] Y. Akiba *et al*., Nucl. Instrum. Meth. A **453**, 279 (2000).

[14] A. Bazilevsky, RIKEN Review **28**, 15 (2000).

[15] K. Reygers, Nuclear Physics A **715**, 683c (2003).

[16] M. Aizawa *et al*., Nucl. Instrum. Meth. A **499**, 508 (2003).

[17] A. Einstein, Annalen der Physik **17**, 891 (1905).

[18] A. Akindinov *et al*., Nucl. Instrum. Meth. A **456**, 16 (2000).

[19] P. Fonte, IEEE Transactions on Nuclear Science **49**, 881 (2002).

[20] A. Alici, Nuovo Cim. **027C**, 403 (2004).

[21] G. F. Knoll, *Radiation, Detection and Measurement*, 3rd ed. (John Wiley and Sons, New York, NY, 2000).

[22] E. C. Zeballos *et al*., Nucl. Instrum. Meth. A 373, 35 (1996).

[23] M. C. S. Williams, Nucl. Instrum. Meth. A **525**, 168 (2004).

[24] Y. Wang *et al*., Nucl. Instrum. Meth. A **538**, 425 (2005).

[25] A. N. Akindinov *et al*., Nucl. Instrum. Meth. A **533**, 93 (2004).

[26] L. E. Kline *et al*., Journal of Applied Physics **50**, 6789 (1979).

[27] K. Abe et al., Nucl. Instrum. Meth. A **455**, 397 (2000).

[28] M. Iori and F. Massa, NASA STI/Recon Technical Report N 91, 20460 (1990).

[29] E. C. Zeballos *et al*., Nucl. Instrum. Meth. A **367**, 388 (1995).

[30] W. J. Llope *et al*., Nucl. Instrum. Meth. (2008).